

**HIGH CONTRAST SPHERE-SUPPORTED
THIN-FILM ELECTROLUMINESCENT DEVICES**

**High Contrast Sphere-Supported Thin-Film
Electroluminescent Devices**

BY

YUNXI SHI, B. SC.

A Thesis

Submitted to the School of Graduate Studies
in Partial Fulfillment of the Requirements
for the Degree
Master of Applied Science

McMaster University

© Copyright by Yunxi Shi, 2006

Master of Applied Science (2006)
(Engineering Physics)

McMaster University
Hamilton, Ontario

**TITLE: HIGH CONTRAST SPHERE-SUPPORTED
THIN-FILM ELECTROLUMINESCENT
DEVICES**

**AUTHOR: Yunxi Shi,
B.Sc. (WuHan University)**

SUPERVISORS: Professor A. H. Kitai

NUMBER OF PAGES: xv, 125

ABSTRACT

This thesis is concerned with the improvement of the contrast ratio of flexible display devices, which are Sphere Supported Thin Film Electroluminescent (SSTFEL) devices. A two-layer coating system was selected as anti-reflection (AR) coatings to be deposited on the surface of SSTFEL devices to reduce the reflection of the ambient light from the surface of devices based on the interference concept. This AR coating was composed of an ITO layer and an ultra-thin gold layer. In order to maximize destructive interference in the visible wavelength range, the optical properties, including refractive index, transmittance and reflection of ITO films and ultra-thin gold films related to sputtering conditions have been studied. The electrical conductance of these two films has also been explored because these two layers work not only as AR coatings but also as a conductive and transparent electrode of SSTFEL devices. AFM images show that the surface morphology of ultra-thin gold films on Si substrates is similar to that on an ITO layer and on polypropylene sheets. The measurements of specular and diffuse reflectance of AR coatings on the propylene sheets and devices have been performed in detail. Results show that AR coatings have better performance on the devices when the thickness of ultra-thin gold layers and ITO layers are 3.43 to 4.01nm, and 42.5 to 45.0nm respectively. Specular and diffuse reflectance of SSTFEL devices with AR coatings are around 1.3% and 13.6% respectively, which is 6.3 times less than that of devices without AR coatings. The contrast ratio of devices with AR coatings is up to 47.9:1 at the ambient illumination level of 52.6Lux. At the ambient illumination level of 200 Lux, the contrast

ratio of SSTFEL devices is 5 times higher than that of SSTFEL devices without AR coatings.

During the research on the properties of ultra-thin gold films, it has been observed that the ultra-thin gold film has unreported optical and electric properties when its thickness is around 3nm. Its reflectance spectrum is similar to the reflectance spectrum of the substrate, whether the substrate is a glass slide or a wafer of silicon, and follows the reflectance spectrum of the substrates with an increase of several percent in visible wavelength range. The conductance of the ultra-thin gold film decreases by exponential decay as its thickness decreases for the conductance is based on tunneling effects. However, the conductance suddenly increases while the thickness of the ultra-thin gold layer is decreased at around 3 to 4 nm. This behavior has not been reported and explained.

ACKNOWLEDGEMENTS

There are a number of people who deserves gratitude for helping me in study, English learning and life in Canada.

First of all, I want to extend my deeply appreciation to my current supervisor, Dr. Adrian Kitai, for his kindness to give me the opportunity to work on this project in his group. I am also grateful for his guidance, advice in project, and especially prompt and careful review of the thesis. His unwavering help to each of his students is appreciated more than he knows.

I am full of gratitude to my previous supervisor, Dr, Thompson, for giving me the opportunity to study in McMaster, and his time, advice and guidance in previous project. I would like to thank my previous co-supervisor, Dr. Jamal Deen, for his help and support since the beginning of the previous project.

I am especially grateful to Dr. YingWei Xiang for training and assisting me in the fabrication of SSTFEL display devices. Without his help in the manufacture processes, this work would have been much more time consuming; Xiaonan Tan for his fruitful discussions in the theory of AR coatings, thin film theory and measurement of index and thickness of various films by Ellipsometry. Here I want to make my special thanks to Andy Duft especially for his excellent job and experience in AFM measurement, which contributed greatly to this thesis. Many thanks go to Karen Neumann in chemistry department for her help in the transmittance measurement of ITO films and ultra-thin gold films.

I would like to express my sincere thanks to Dr. Ziling Peng, Doris, Dr. D. Bruce and Peter Jonasson for training and assistance in clean-rooms of CEDT, and many useful

discussions in my research projects. I would also like to thank Dr. B.J.Robinson for growing my samples in the previous research project.

Many great thanks go to all of my friends who once helped me in Canada whether in study, life or English learning: They are Lao Zhang, Wenjung, Xiao Bao and his wife, Alice, Liu Wen, Xiang Qing and her husband in Ottawa; Ziling Peng, Yang Jang, Honggang Yu, Pan Lian, Weihong Jian, ShanShan Zhang, Bo Chen, Fangfang Zhang, Jiangcong Wang and Huiling Wang at McMaster; Mexican gang includes Ana, Jorge, Edgar and their best friend Julia. I would like to say: Thanks.

Last but not least, many thanks go to Dr. P.E Jessop, Marge Huntley and Shelley Lancaster for their kind help and what they did during this year.

Thanks a lot forever in my heart to people who deserve gratitude for helping me in Canada, the hometown of Dr. Norman Bethune.



Dr. Norman Bethune worked in Taihang Mountains of P.R.China 1939

CONTENTS

CHAPTER 1 INTRODUCTION	1
1.1 Introduction	1
1.2 Flexible Display Technologies	2
1.3 Enhanced Contrast Technologies of Display and This Work	4
CHAPTER 2 BASIC CONCEPTS OF THIN FILM EL DISPLAY AND ANTI-REFLECTION COATINGS	9
2.1 Electroluminescence of SSTFEL Devices.....	9
2.2 Fresnel Equations	11
2.3 Basic Theory of Anti-Reflection Coating	15
2.3.1 Single-Layer Anti-Reflection Coating	16
2.4 Contrast Ratio of Displays and Reflection	18
CHAPTER 3 FABRICATION PROCESSES OF SSTFEL DEVICES	23
3.1 The Structure of SSTFEL Devices in Detail	23
3.2 The Fabrication Processes of SSTFEL Devices.....	24
3.2.1 Sintering and Patterning BaTiO ₃ Spheres	24
3.2.2 Sputtering and Annealing of Green Phosphors	28
3.2.3 Embedding Process	28
3.2.4 Sputtering AR Coating and Electrodes	31

CHAPTER 6 SETUP OF MODEL FOR AR COATINGS ON POLYPROPYLENE SHEETS, SIMULATION RESULTS AND DISCUSSION	91
6.1 Model for the Reflectance Simulation of AR Coatings on Polypropylene Sheets.....	91
6.2 The Reflectance of the AR Coating on Polypropylene Sheets.....	94
6.3 Extracting Transmittance spectra of The Ultra-thin Gold Layer and The ITO Layer from Experimental Results	97
6.4 Extracting Reflectance Spectra of The Complex Surface and Interface from Experimental Results.....	99
6.5 Calculating reflectance of AR coatings on Polypropylene Sheets	101
 CHAPTER 7 CONCLUSION AND FUTURE WORKS	 111
7.1 Conclusion	111
7.2 Recommendations for Future Work.....	113
 APPENDIX:	
A EXPERIMENTAL SETUOP OF REFLECTIVITY MEASUREMENT SYSTEM	115
A1 Experimental Setup and Measurement for the Specular Reflection.....	115
A2 Experimental Setup and Measurement for the Diffuse Reflection.....	117
B ELLIPSOMETRY MEASUREMENT SYSTEM	119
 REFERENCE	 122

LIST OF FIGURES

Figure 1.1	A prototype of the Sphere-supported thin-film electroluminescent device.....	3
Figure 1.2	The schematic SSTFEL structure diagram shows that numerous spheres with a green phosphor on its top were embedded within a polypropylene sheet to form a flexible device.	4
Figure 1.3	The diagrams of samples show the applications of the black cathode (a) on the backside of the EL device patented by Xerox, and (b) the black layer on the backside of the OLED device patented by Luxell Inc.	6
Figure 1.4	The schematic diagram of SSTFEL device under the office illumination	6
Figure 1.5	Schematic diagrams of SSTEFL devices in detail from top-view and side-view.	7
Figure 1.6	Schematic diagrams of specular (a) and diffuse (b) reflections from the surface of the SSTFEL device including two part (A, B) areas.	8
Figure 2.1	Schematic diagrams of basic device structure and principle of the EL. ...	10
Figure 2.2	Schematic diagram of the equivalent circuit of TFEL devices.	10
Figure 2.3	Defining diagram of incident (\mathbf{k}_i), reflected (\mathbf{k}_r), and transmitted (\mathbf{k}_t) rays at a XZ-plane interface when the electric field is the transverse electric (<i>TE</i>) mode.	12
Figure 2.4	Schematic diagrams of a single-layer AR coating system, and light rays transmitted and reflected by this film when multiple reflections are neglected.	16
Figure 2.5	Reflectance from a single film layer versus normalized path difference. The dashed line represents the uncoated glass substrate of index $n_s=1.52$	17
Figure 2.6	Schematic structures of simplified displays. (A) expresses emissive displays including CRTs, PDPs, FEDs, and TFELs; (B) for the case of transmissive LCDs; and (C) for reflective LCDs.	19
Figure 2.7	Schematic diagrams of specular and diffuse reflections from the surface of the SSTFEL device with AR coatings including two part areas	21
Figure 3.1	A schematic structure diagram of the Sphere-Supported Thin-Film Electroluminescent Device.	23

Figure 3.2	A temperature curve of the BaTiO ₃ sphere sintering process.	25
Figure 3.3	Al ₂ O ₃ plate with special arrays of containing cells. Each cell has a matrix of dents with 5x5 pattern. BaTiO ₃ spheres were patterned inside dents.	27
Figure 3.4	Schematic diagrams of the embedding process (a) and resultant (b) in first step.	29
Figure 3.5	Schematic diagrams of embedding processes (a) and resultant (b) in the second step.	30
Figure 3.6	The image shows that the high RF power can crack and wrinkle the polypropylene sheet of devices by heating sample during the ITO deposited process.	32
Figure 3.7	An image shows the SSTFEL device with AR coating under office illumination.	33
Figure 4.1	Thickness of ITO films via the sputtering times under different RF Powers.	35
Figure 4.2	Deposition rates of ITO films via the RF Powers.	36
Figure 4.3	Deposition rates of ITO films via chamber pressures.	37
Figure 4.4	Resistivity of ITO films are relevant to RF power under sputtering conditions with chamber pressure of 0.5mTorr and Ar flow ratio of 7.0sccm.	38
Figure 4.5	Resistivity of ITO films is relevant to the chamber pressure under sputtering conditions with RF power of 30W and Ar flow ratio of 7.0sccm.	39
Figure 4.6	Index of ITO films fabricated under different RF powers with different thickness.	40
Figure 4.7	Index of ITO films is relevant to the RF power under sputtering conditions with the chamber pressure of 0.5mTorr and Ar flow ratio of 7.0sccm.	41
Figure 4.8	Index of ITO films are relevant to the chamber pressure under sputtering conditions with RF power of 30W and Ar flow ratio of 7.0sccm.	41
Figure 4.9	Transmittance spectra of ITO films with different thickness but deposited at the same RF power of 30W and the same chamber pressure of 0.5mTorr.	42

Figure 4.10	Transmittance spectra of ITO films deposited under different chamber pressures, but at the same RF power of 30 W and the same sputtering time of 6 minutes.	43
Figure 4.11	Transmittance spectra of ITO films deposited under different chamber pressures, but the same RF power of 30W and the same sputtering time of 6 minutes.	44
Figure 4.12	Images of AFM scanned over $1 \times 1 \mu\text{m}^2$ on ultra-thin gold films sputtered on Si substrates ranging from 5 seconds (or 5'')(a), 8 seconds (or 8'')(b) to 40 seconds (or 40'')(f). Each group has four images. Three of them are images viewed from different angles. One in the right-bottom is the measurement result of thickness of the relevant ultra-thin gold films.	49 to 53
Figure 4.13	Thickness of Ultra-thin gold film via the sputtering times.	47
Figure 4.14	Images of AFM scanned over $500 \times 500 \text{nm}^2$ of ultra-thin gold films sputtered on the surface of ITO layer on Si substrates ranging from 7 seconds (or 7'')(a), 10 seconds (10'')(b), 15 seconds (15'')(c) to 35 seconds (35'')(e). (f) is the image of ultra-thin gold films sputtered on the surface of ITO layer on a polypropylene sheet. Each group has two images viewed from top and side views.	54 to 56
Figure 4.15	Sheet resistance of ultra-thin films with sputtering time ranging from 3 second to 60 second. Below tick labels of bottom axis are the sputtering time of ultra-thin gold films, and upper tick labels of bottom axis are the thickness of ultra-thin gold films related to the sputtering time. The scale is shown in the top axis.	60
Figure 4.16	Reflection spectra of ultra-thin gold films on Si substrates with sputtered time ranging from 5 second (5'') to 5 minutes (5'). In-site is reflection spectrum of bulk gold with polished surfaces.	63
Figure 4.17	Reflection spectra of ultra-thin gold films on glass slide substrates with sputtered time ranging from 5 seconds to 5 minutes.	63
Figure 4.18	Transmittance spectra of ultra-thin gold films on glass slide substrates with sputtering time ranging from 5 seconds to 5 minutes.	65
Figure 5.1	Specular reflectance spectra of samples with an ITO film of 100nm on Au ₂ /pp and without a ITO film on Au ₂ /pp. The in-site is the reflectance of bulk gold with a polished surface.	67
Figure 5.2	Specular reflectance spectra of samples with different thickness of AR coating layers on Au ₂ /pp, organized based on the sputtering time of ITO layers.	70 to 73

Figure 5.3	Specular reflectance spectra of samples with different thickness of AR coating layers on Au2'/pp, organized based on the sputtering time of ultra-thin gold layers.	74 to 75
Figure 5.4	Lower reflectance spectra of samples in figure 5.3 with different thickness of AR coating layers on Au2'/pp.	76
Figure 5.5	Diffuse reflectance spectra of samples with different thickness of AR coating layers on Au2'/pp, organized based on the sputtering time of ITO layers.	79 to 82
Figure 5.6	Diffuse reflectance spectra of samples with different thickness of AR coating layers on Au2'/pp, organized based on the sputtering time of ultra-thin gold layers.	82 to 84
Figure 5.7	Lower reflectance spectra of samples in figure 5.6 with different thickness of AR coating layers on Au2'/pp.	84
Figure 5.8	Specular reflectance spectra of SSTFEL devices with or without AR coatings.	87
Figure 5.9	Diffuse reflectance spectra of SSTFEL devices with or without AR coatings.	88
Figure 6.1	A schematic diagram of the model for AR coatings on polypropylene sheets.	91
Figure 6.2	Schematic diagram of AR coating on thick gold layer with the thickness of 360nm.	95
Figure 6.3	Schematic diagrams of the transmittance measurement of ITO films deposited on glass slides by Cary 50 Probe UV Visible Spectrophotometer.	98
Figure 6.4	Schematic diagrams of the transmittance measurement of ultra-thin gold films on glass slides by Cary 50 Probe UV Visible Spectrophotometer. ...	99
Figure 6.5	Schematic diagrams of interface reflections between the air and a thick gold layer (a); and between the ITO layer and the thick gold layer (b). ...	101
Figure 6.6	Simulation results of specular reflectance of AR coatings composed of ultra-thin gold layer with sputtering time of 5 seconds and different ITO layers are shown from (a) to (g) as the parameter of Δ is changed from 0 to π . (h) is the measurement results of AR coatings composed of ultra-thin gold layer with sputtering time of 4 seconds and different ITO layers.	103 to 106

Figure 6.7	Simulation results of specular reflectance of AR coatings composed of ultra-thin gold layer with sputtering time of 12 seconds and different ITO layers are shown from (a) to (g) as the parameter of Δ is changed from 0 to π . (h) is the measurement results of AR coatings composed of ultra-thin gold layer with sputtering time of 11 seconds and different ITO layers.	107 to 110
Figure A.1	A schematic diagram of the measurement set up of the specular reflection.	116
Figure A.2	A schematic diagram of the measurement set up of the diffuse reflection	117
Figure A.3	This graph shows the percent reflectance of the KODAK Grad Card in relation to light wavelength in nanometers. A white side curve is the reflectance spectrum of the reference sample.	118
Figure.B.1	Schematic diagram of a null ellipsometry measurement system.....	119

LIST OF TABLES

Table 3.1	Shrinkage of BaTiO ₃ sphere diameter after sintering at high temperature.	25
Table 3.2	Sputtering conditions of ITO films.	30
Table 4.1	Sample voltages measured with 4-point probe and relevant calculated resistance (ohms per square) for group 1.	56
Table 4.2	Sample voltages measured by 4-point probe and relevant calculated resistance (ohms per square) for group 2.	57
Table 5.1	Integration areas of specular reflection spectra ranging from 410 to 700nm for lower spectra of samples in figure 5.4.	67
Table 5.2	Integration areas of diffuse reflection spectra ranging from 425 to 700nm for lower spectra of samples in figure 5.7.	81
Table 5.3	Integration areas of specular reflection spectra ranging from 410 to 700nm in figure 5.8 for SSTFEL devices with different AR coating layers.	82
Table 5.4	Integration areas of diffuse reflection spectra ranging from 425 to 700nm in figure 5.9 for SSTFEL devices with different AR coating layers.	83
Table 5.5	Contrast of SSTFEL devices with or without AR coating system under different illumination conditions	87

Chapter 1 Introduction

1.1 Introduction

In a growing information society, individuals are linked to information through a variety of hardware interfaces. More than 90 percent of information we acquire is visual. The display as an output device bridges information between electronic devices and human beings. In other words, it has an essential property, totally unlike other information processing devices, to perform as a man-machine interface, interpreting analog and digital information signals for us. Because of this unique feature, a display needs to have some human-compatible characteristics to fully function as a man-machine interface. In addition, technological and economical processes have been significant. For example, the display was developed having a full color image, small thickness, light weight, and the large viewing area

More than 100 years have passed since Braun invented the CRT as a display device in 1897 [1.1]. Although drastic changes in the electronics world and display technologies have been introduced based on various operating principles for these past 100 years, no other technology in this display field has existed for such a long time as the CRT. CRTs established their status in the past as a high-performance and cost-effective device, and were used for TVs and PC monitors. However, CRTs are confronting their limit of performance due to the restriction of screen size. Although effort is still being devoted to enlarging its viewing area and reducing depth, a move from bulky CRT displays toward thinner, lighter, flat panel Liquid Crystal Displays (LCDs) and Plasma displays (PDPs) has been underway in recent years. In the consumer market now, people

are increasingly choosing the flat LCD and plasma TVs, not only for the space-saving potential and the enhanced appearance but also for their high contrast and quality images.

However, while these display technologies are developing, research is starting on larger displays as well as wall-sized or flexible displays for applications such as for facilitating group work, interaction and teaching in the classroom and in other fields

1.2 Flexible Display Technologies

The move from CRTs to FPDs has resulted in significant space savings, and enhanced mobility, as in the case of the laptop computer. A flexible display is expected to have the next significant impact in the field of displays in which rigid glass sheets are no longer required. Several flexible displays have been prototyped, such as reflective liquid crystal displays [1.2,1.3], OLED displays [1.4,1.5] and sphere-supported thin-film electroluminescence (SSTFEL) devices [1.6].

The reflective mode of liquid crystals can be utilized to make LCDs as flexible displays. In the reflective mode, liquid crystals modulate reflectance of ambient light to display images. Recently, color TFT-LCD and amorphous-silicon active-matrix panels have been demonstrated on a plastic substrate [1.3]. However this kind of flexible display does not always have enough brightness since they do not emit light.

Based on the self-luminous and plastic properties, OLED displays can be made on flexible substrates with enough brightness to show good quality images. However, they are very sensitive to moisture and oxygen and degrade if exposed to either. The challenge now is to find new organic materials with less sensitivity to moisture and oxygen, or to

develop a gas and vapor protected flexible substrate or flexible seal technologies for displays.

Sphere-supported thin-film electroluminescence (SSTFEL) technology is a new platform technology developed at McMaster University to fabricate a flexible display. It has been demonstrated by a prototype display device in figure 1.1 [1.7]. The basic structure of this device is shown in figure 1.2 [1.7]. On the top areas of BaTiO_3 spheres

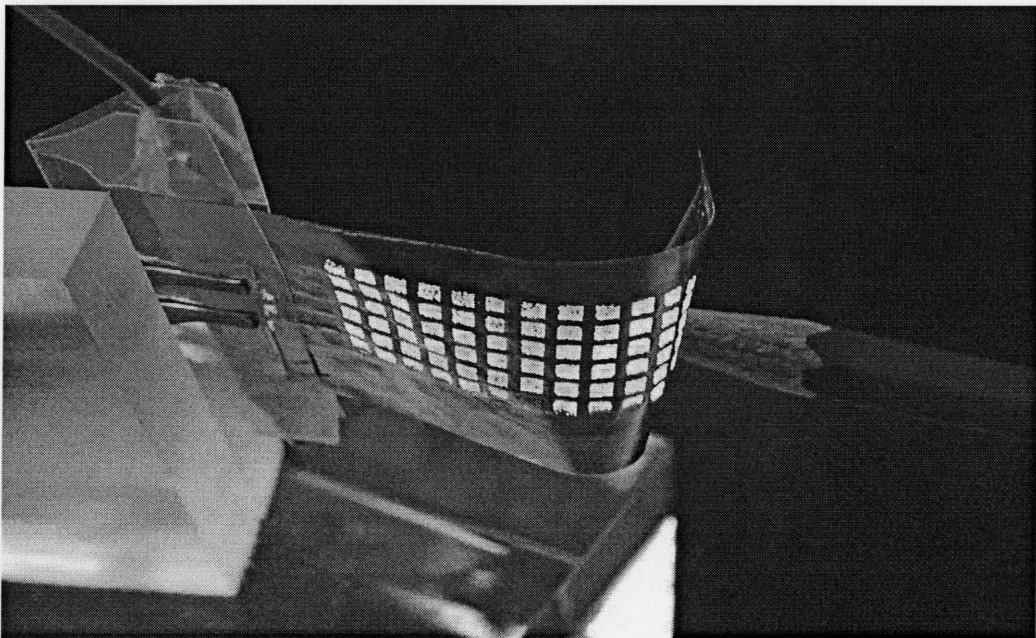


Figure 1.1 a prototype of the Sphere-supported thin-film electroluminescence device

are a sandwich structure composed of two Al_2O_3 layers and a thin-film oxide EL phosphor ($\text{Zn}_2\text{Si}_{0.5}\text{Ge}_{0.5}\text{O}_4:\text{Mn}$) layer. Two electrodes are made by depositing a gold layer on the backside and a transparent ITO (Indium-Tin Oxide) layer on the front-side of the device to form a thin-film electroluminescence (TFEL) structure, which will be discussed in detail in Chapter 2. Therefore, BaTiO_3 spheres embedded within a flexible

polypropylene sheet become light-emitters and emit light under the application of an AC voltage in the range of 120 to 200 volts (peak).

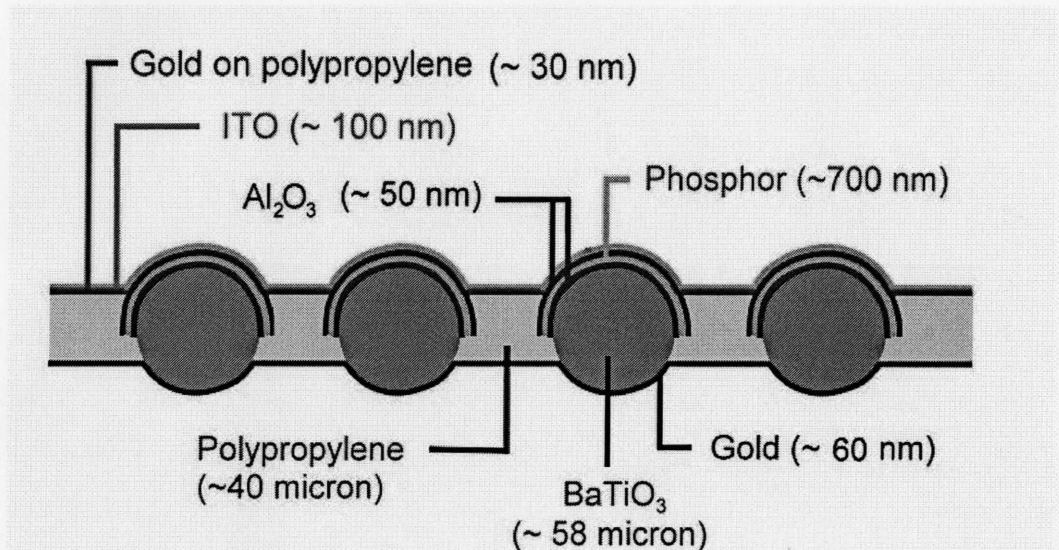


Figure 1.2 The schematic SSTFEL structure diagram shows that numerous spheres with a green phosphor on its top were embedded within a polypropylene sheet to form a flexible device.

Unlike other flexible display technologies, the SSTFEL device based on TFEL technology is a self-luminous display technology and has the advantage of not being sensitive to humidity and air.

1.3 Enhanced Contrast Technologies of Display and This Work

All display screens have specular and diffuse reflections that can degrade image contrast and affect image quality. They generally require a contrast enhancing technology to improve visual performance.

Anti-reflectance (AR) coatings are most widely used for enhancing the contrast of displays. They can effectively reduce the specular and diffuse reflection of ambient light on the surface or interfaces in a display system [1.8]. An important surface of a display screen is the front surface in the optical system, the surface closest to the viewer. In CRT displays and flat panel displays such as PDPs and FEDs, AR coatings are deposited on the surface of the glass screen to reduce reflection of ambient light and to enhance the contrast of images.

However, two other kinds of contrast enhancement technologies have been demonstrated in order to reduce the reflection of ambient light from EL displays, including OLED. In EL displays, light emitting material such as sulfide or oxide-based materials in the inorganic EL display, and organic self-luminous materials in the OLED are transparent. At the front of display devices, an ITO film is often deposited to work as a conductive and transparent electrode, which allows transmission of the emitting light. Therefore, ambient light not only reflects from the surface of the EL display but also can pass through the ITO layer and light emitting materials. Then it reflects strongly from the back metal electrode of devices. Both reflections degrade the contrast of displays. Therefore, a black layer working as the back electrode of devices is very important to enhance the contrast of EL displays. One kind of black cathode has been developed by Xerox Corp. It is an absorbing and conducting cathode to be put on the backside of organic layers. Another black cathode is a new generation of black metal conducting layers developed by Luxell Inc. and applied on the backside of OLEDs to reduce the

reflection of ambient light [1.9]. Both of these black cathodes are shown in figure 1.3 [1.10].

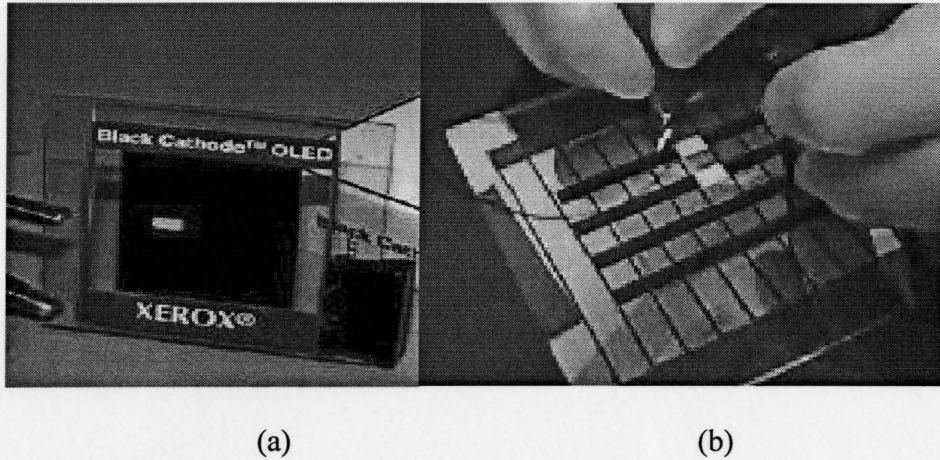


Figure 1.3 The diagrams of samples show the applications of the black cathode (a) on the backside of the EL device patented by Xerox, and (b) the black layer on the backside of the OLED device patented by Luxell.

Figure 1.4 shows the image of an SSTFEL device under normal illumination in an office. Because an electrode layer on the device surface is composed of a 30nm gold layer and an ITO layer with very high reflectance in visible wavelengths of about 40% and 11% respectively, it obviously can be seen that this SSTFEL device has very high

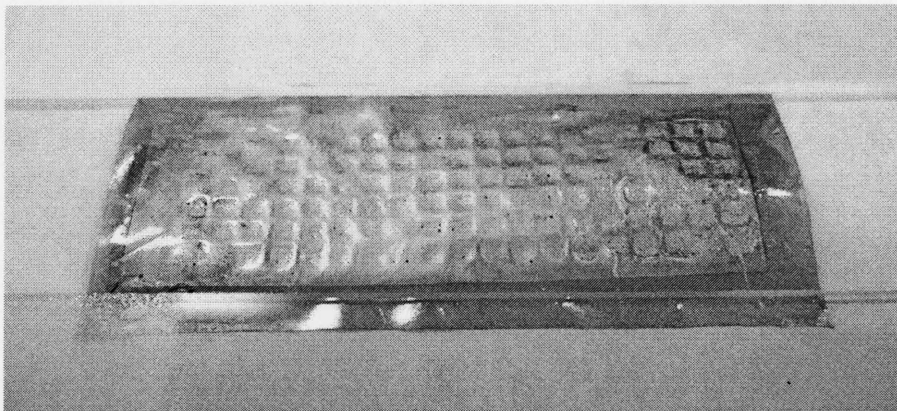


Figure 1.4 The schematic diagram of SSTFEL device under the office illumination

reflectance due to the direct reflection of this gold layer. Thus SSTFEL devices suffer from low contrast under ambient illumination and need AR coatings to enhance contrast.

There are also two types of reflections while light is incident on the surface of SSTFEL display devices: specular reflection and diffuse reflection. For SSTFEL devices, surface reflection is complicated due to the special structure of the SSTFEL device shown in figure 1.5. The surface of the SSTFEL device is composed of

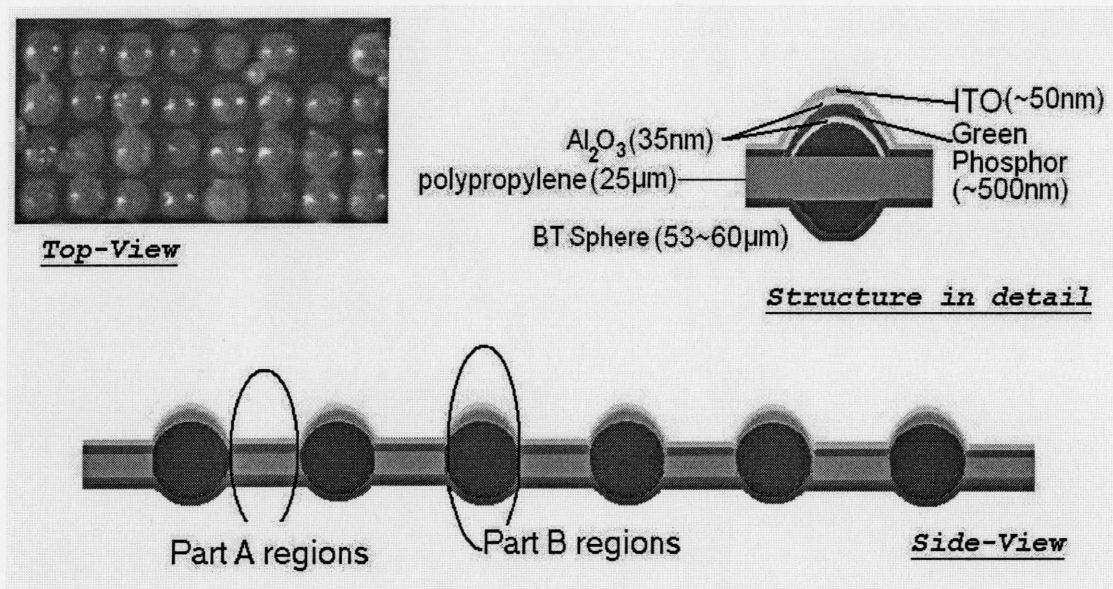


Figure 1.5 Schematic diagrams of SSTFEL devices in detail from top-view and side-view.

two areas: the area of part A on the surface of the device is composed of a 30 nm gold layer and an ITO layer deposited on the smooth surface of the polypropylene sheet with a minor roughness and exhibiting predominately specular reflection as shown in figure 1.6(a); the other is area of part B, the spherical surface of BaTiO₃ spheres embedded within the polypropylene sheet shown in figure 1.6(b). It is known that an ITO layer,

Al_2O_3 layers and phosphor layer deposited on the top area of BaTiO_3 spheres are all transparent, and the surface of BaTiO_3 spheres is white with high reflectance. Therefore, the diffuse reflection from region B is very high under ambient illumination. The challenge of this work is to develop AR coatings for reducing the ambient light reflection including specular and diffuse reflections from the surface of SSTFEL devices in order to enhance the contrast ratio of SSTFEL devices.

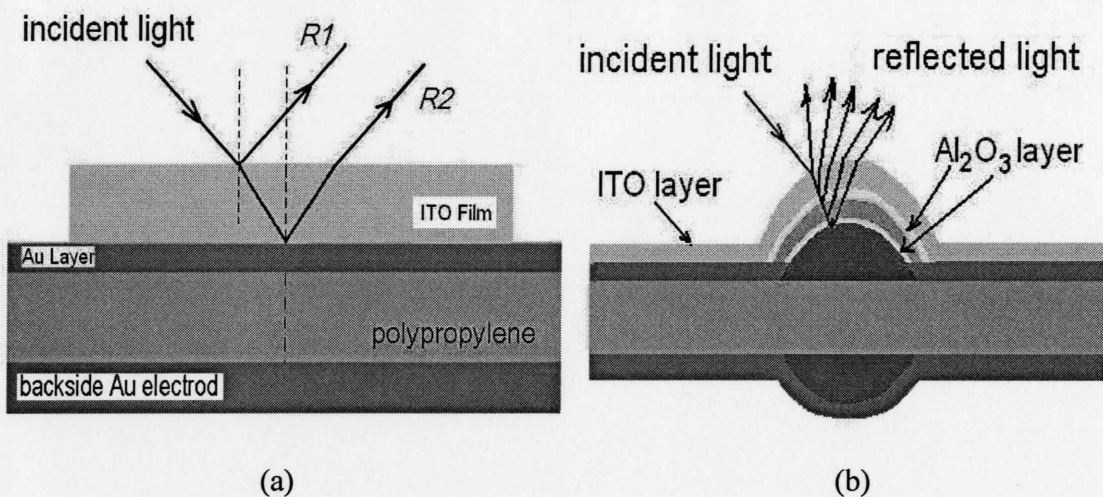


Figure 1.6 Schematic diagrams of specular (a) and diffuse (b) reflections from the surface of the SSTFEL device including two part (A, B) areas

A two layer AR coating system, which is composed of an ITO film and an ultra-thin gold film, were selected to make the AR coatings because such coatings can effectively reduce both specular and diffuse reflections and are expected to work well on both areas of the device surface.

Chapter 2 Basic Concepts of Thin Film EL Display and Anti-Reflection Coatings

Basic concepts relevant to the sphere-supported thin-film electroluminescent (SSTFEL) devices and anti-reflection coatings are presented in this chapter, including the basic theory of thin film EL, Fresnel equations, two-beam interference and contrast ratio of SSTFEL devices.

2.1 Electroluminescence of SSTFEL Devices

Electroluminescence is the phenomenon by which electrical energy is converted to luminous energy and was first observed in 1929 [2.1]. Today EL is classified into inorganic EL and organic EL (discovered in 1987) [2.2]. Both kinds of EL have application to a full-color flat panel display.

In a thin-film EL (TFEL) display, the light-emitting layer is only about $0.5\mu\text{m}$ to $1.0\mu\text{m}$ thickness and total device thickness is about $1\text{-}2\mu\text{m}$. Driving voltages are AC voltage. The basic structure of TFELs consists of 5 layers shown in figure 2.1 (a) [2.3]. The middle layer is the phosphor layer, which is made mainly from sulfide-based materials; however, oxide-based materials may also be used. Light is emitted from a TFEL device when a voltage is applied on the device and the electric field across the thin film stack reaches threshold strength of about 10^6 (V/cm). Under the application of the voltage, electrons tunnel from interface states at the dielectric/phosphor interface, shown in figure 2.1(b) [2.4], and then are accelerated by the high electric field of about 10^6

(V/cm) in the phosphor layer. Once the electrons gain enough energy from the electric field they can impact excite luminescent centers to emit light and ionize electrons

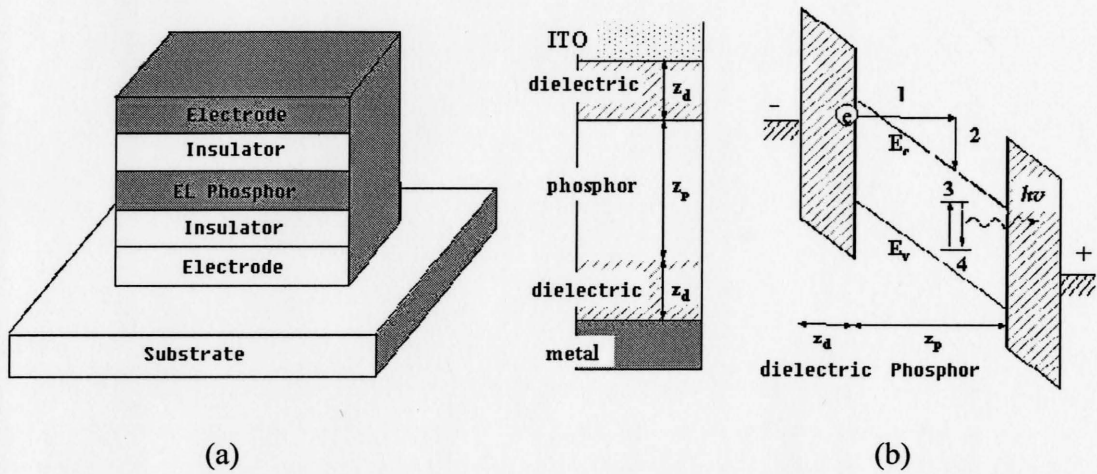


Figure 2.1 Schematic diagrams of basic device structure and principle of the EL

from atoms to create avalanche current. When electrons reach the opposite side of the phosphor layer, they are trapped at interface states. They will be released again when the applied voltage is reversed; then the same process is repeated in reverse.

The devices can be modeled [2.5] as a pair of back-to back Zener diodes connected to two series capacitors as shown in figure 2.2: C_i is an equivalent capacitor of

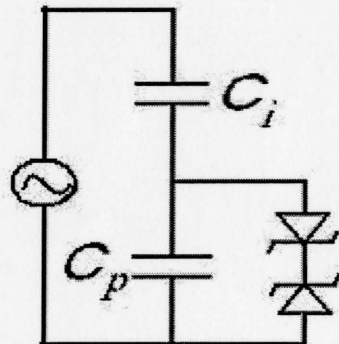


Figure 2.2 Schematic diagram of the equivalent circuit of TFEL devices

the dielectric layer; and C_p is an equivalent capacitor of the phosphor layer. Under an applied voltage V_a to the device, the voltage applied to the phosphor layer, V_p is expressed as [2.6]

$$V_p = \frac{1}{1 + \frac{\epsilon_p d_i}{\epsilon_i d_p}} V_a \quad (2.1)$$

and luminance (L) of devices[2.4]

$$L_{EL-on} = \frac{4}{\pi} \eta f \epsilon_0 \epsilon_i \left(\frac{d_p}{d_i} \right) E_{p,th} (V_a - V_{th}) \quad (2.2)$$

ϵ_i , ϵ_p are the related dielectric constant of dielectric layer and phosphor layer respectively, and d_i , d_p are the thickness of dielectric layer and phosphor layer respectively. f is the frequency of an AC applied voltage, and η is the luminous efficiency of the phosphor layer.

From the above two equations, there are two methods by which the luminance of the device may be improved under a constant modulation voltage ($V_a - V_{th}$). One way is to maximize the thickness of the phosphor layer relative to the dielectric layer and use the dielectric layer with a high dielectric constant, such as BaTiO₃ with $\epsilon_i \sim 2000-4000$. The other important method is to increase the luminous efficiency of the phosphor layer, η .

2.2 Fresnel Equations [2.7, 2.9]

Fresnel equations express the ratio of both reflected and transmitted E -field amplitudes to the incident E -field amplitude when light is incident on the surface or the interface of dielectric materials. Let us assume a ray of light incident at point P on an

interface on the xz -plane. Figure 2.3 [2.7] shows the resulting reflected and refracted rays. The plane of incidence is xy -plane.

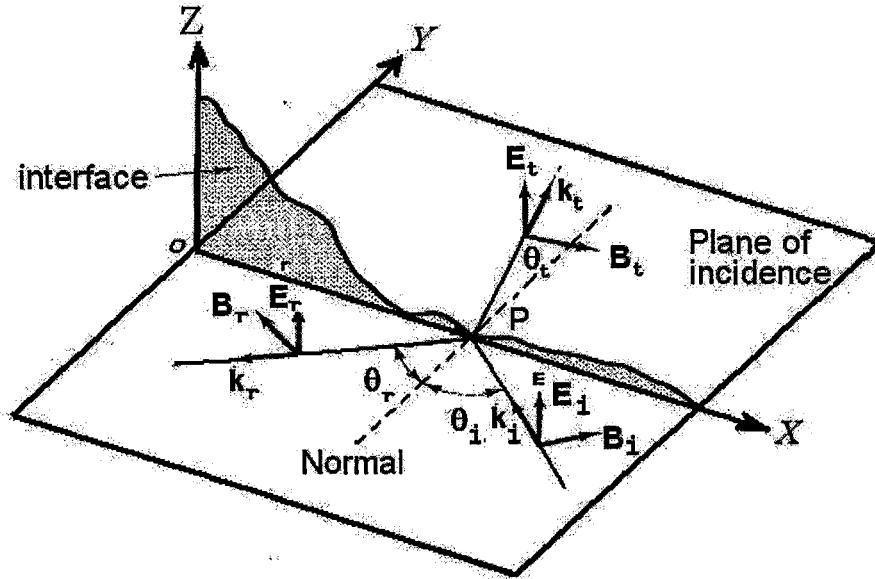


Figure 2.3 Defining diagram of incident (\mathbf{k}_i), reflected (\mathbf{k}_r), and transmitted (\mathbf{k}_t) rays at a XZ -plane interface when the electric field is the transverse electric (TE) mode

The incident light is assumed a plane harmonic wave expressed as

$$\vec{E}_i = \vec{E}_0 e^{i(\vec{k} \cdot \vec{r} - \omega t)} \quad (2.3)$$

The reflected and transmitted waves in figure 2.3 can be expressed, respectively, as

$$\vec{E}_r = \vec{E}_{0r} e^{i(\vec{k}_r \cdot \vec{r} - \omega_r t)} \quad (2.4)$$

$$\vec{E}_t = \vec{E}_{0t} e^{i(\vec{k}_t \cdot \vec{r} - \omega_t t)} \quad (2.5)$$

In the interface plane xz , where all three waves exist simultaneously, their relationship cannot depend on the arbitrary choice of a boundary point r or a time t , and

should be fixed. The phases of the three waves, which depend on r and t , must themselves be equal:

$$(\vec{k}_i \cdot \vec{r} - \omega t) = (\vec{k}_r \cdot \vec{r} - \omega_r t) = (\vec{k}_t \cdot \vec{r} - \omega_t t) \quad (2.6)$$

This equation yields

$$\omega_i = \omega_r = \omega_t \quad (2.7)$$

and

$$\vec{k}_i \cdot \vec{r} = \vec{k}_r \cdot \vec{r} = \vec{k}_t \cdot \vec{r} \quad (2.8)$$

where $k_r = n_r \omega / c$, and $k_t = n_t \omega / c$. The first two terms and last two terms of Eq.(2.8) become

$$\text{law of reflection:} \quad \theta_i = \theta_r \quad (2.9)$$

$$\text{and Snell's law of refraction:} \quad n_1 \sin \theta_i = n_2 \sin \theta_t \quad (2.10)$$

With the help of boundary conditions arising out of Maxwell's equations, the requirement of these boundary conditions for the electric fields of transverse electric (*TE*) mode:

$$E_i + E_r = E_t \quad (2.11)$$

In the case of the corresponding magnetic fields,

$$B_i \cos \theta_i - B_r \cos \theta_r = B_t \cos \theta_t \quad (2.12)$$

When we parallel their development for the transverse magnetic (*TM*) mode, we have

$$B_i + B_r = B_t \quad (2.13)$$

$$-E_i \cos \theta_i + E_r \cos \theta_r = -E_t \cos \theta_t \quad (2.14)$$

For non-magnetic material, the magnetic field in the above equations can be expressed in

terms of electric field through the relation

$$B = \frac{n}{c} E, \quad (n=n_2/n_1) \quad (2.15)$$

The reflection coefficient $r=E_r/E$ and transmission coefficient $t=E_t/E$ are obtained from simplifying Eq.(2.9) through (2.15)

$$TE: \quad r = \frac{E_r}{E_i} = \frac{n_1 \cos \theta_i - n_2 \cos \theta_t}{n_1 \cos \theta_i + n_2 \cos \theta_t} \quad (2.16)$$

$$TM \quad r = \frac{E_r}{E_i} = \frac{n_2 \cos \theta_i - n_1 \cos \theta_t}{n_2 \cos \theta_i + n_1 \cos \theta_t} \quad (2.17)$$

$$TE: \quad t = \frac{E_t}{E_i} = \frac{2n_1 \cos \theta_i}{n_1 \cos \theta_i + n_2 \cos \theta_t} \quad (2.18)$$

$$TM: \quad t = \frac{E_t}{E_i} = \frac{2n_1 \cos \theta_i}{n_2 \cos \theta_i + n_1 \cos \theta_t} \quad (2.19)$$

Equations (2.17) through (2.19) are the Fresnel equations, which express the ratio of both reflected and transmitted E -field amplitudes to the incident E -field amplitude by reflection and transmission coefficients. The reflectance and transmittance, respectively, for TE and TM modes of light incident on the surface of the dielectric material are

$$R_{TE} = r_{TE}^2; \quad T_{TE} = 1 - R_{TE} \quad (2.20)$$

$$R_{TE} = r_{TE}^2; \quad T_{TE} = 1 - R_{TE} \quad (2.21)$$

When the reflecting surface is metallic, the Fresnel equations continue to be valid, but the index of homogeneous dielectric materials with conductivity zero will be replaced by the complex index of the metal. The complex index of the metal is a composite of two

parts: one is a real part, the other is an imaginary part, and is associated with its conductivity and energy absorbance.

The complex index, in general, is expressed as

$$\tilde{n} = n_R + in_I \quad (2.22)$$

Therefore, Fresnel equations become

$$TE: \quad r = \frac{E_r}{E_i} = \frac{\tilde{n}_1 \cos \tilde{\theta}_i - \tilde{n}_2 \cos \tilde{\theta}_t}{\tilde{n}_1 \cos \tilde{\theta}_i + \tilde{n}_2 \cos \tilde{\theta}_t} \quad (2.23)$$

$$TM: \quad r = \frac{E_r}{E_i} = \frac{\tilde{n}_2 \cos \tilde{\theta}_i - \tilde{n}_1 \cos \tilde{\theta}_t}{\tilde{n}_2 \cos \tilde{\theta}_i + \tilde{n}_1 \cos \tilde{\theta}_t} \quad (2.24)$$

$$TE: \quad t = \frac{E_t}{E_i} = \frac{2\tilde{n}_1 \cos \tilde{\theta}_i}{\tilde{n}_1 \cos \tilde{\theta}_i + \tilde{n}_2 \cos \tilde{\theta}_t} \quad (2.25)$$

$$TM: \quad t = \frac{E_t}{E_i} = \frac{2\tilde{n}_1 \cos \tilde{\theta}_i}{\tilde{n}_2 \cos \tilde{\theta}_i + \tilde{n}_1 \cos \tilde{\theta}_t} \quad (2.26)$$

2.3 Basic Theory of Anti-Reflection Coating [2.8]

Anti-reflection coatings are used to reduce the surface reflectance of optical components and the reflectance of an interface between two media with different refractive indices. The ideal AR coating is a set of very thin homogeneous layers with refractive indices increasing in small steps from the low index medium to the high-index medium. This coating is of no practical value because there are limits to choices of materials, which can be deposited as hard and environmentally stable coatings. Single-layers and multi-layers have been utilized as a substitute method to make AR coatings.

2.3.1 Single-Layer Anti-Reflection Coating.

A single-layer AR coating optical system is shown in figure 2.4 [2.8]. The reflectance of this system the normal incidence is expressed as [2.8]

$$R = \frac{n_1^2 (n_0 - n_s)^2 \cos^2 \delta + (n_0 n_s - n_1^2) \sin^2 \delta}{n_1^2 (n_0 + n_s)^2 \cos^2 \delta + (n_0 n_s + n_1^2) \sin^2 \delta} \quad (2.27)$$

where n_0 , n_1 , and n_2 express the index of air, a dielectric layer and a substrate respectively. δ is the optical path difference of the film given by

$$\delta = \frac{2\pi}{\lambda_0} (n_1 d_1) \quad (2.28)$$

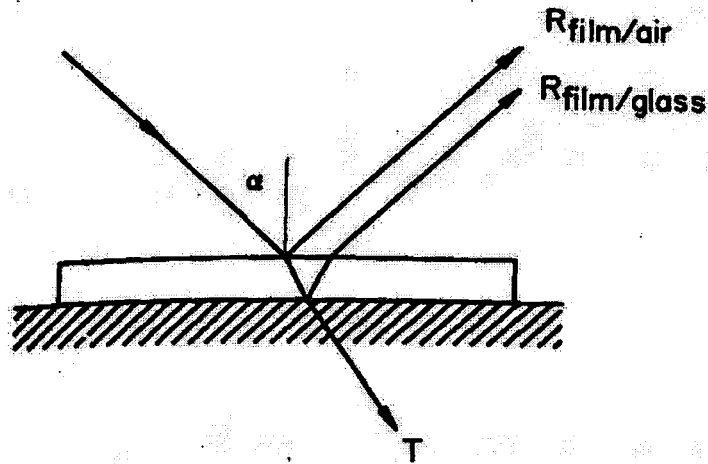


Figure 2.4 Schematic diagrams of a single-layer AR coating system, and light rays transmitted and reflected by this film when multiple reflections are neglected.

When the thickness of the film is a quarter wavelength, $d_1 = \lambda/4$, where λ is the light wavelength in the film, then $\delta = \pi/2$, and

$$R = \left(\frac{n_0 n_s - n_1^2}{n_0 n_s + n_1^2} \right)^2 \quad (2.29)$$

It is obvious that a perfectly non-reflecting film can be made with a coating of $\lambda/4$ and refractive index $n_1 = \sqrt{n_0 n_s}$. When $n_1 < \sqrt{n_0 n_s}$ or $n_1 > \sqrt{n_0 n_s}$, the reflectance cannot be zero even if the thickness of the film is equal to quarter-wavelength. When the substrate is glass with $n_s=1.52$, the ideal index for a nonreflecting coating is $n_1=1.23$, which is shown in figure 2.5. Therefore, there are two ways to tune the reflectance. One

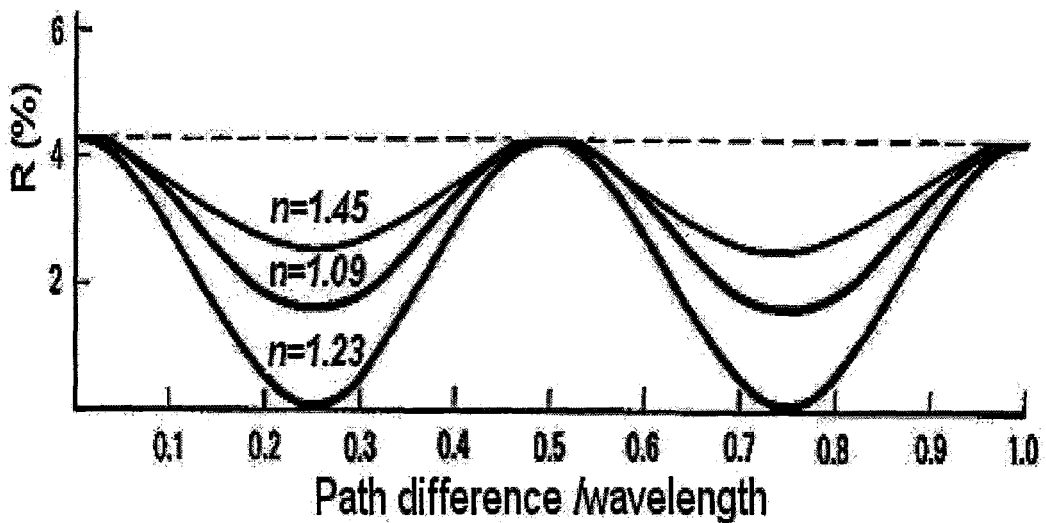


Figure 2.5 Reflectance from a single film layer versus normalized path difference. The dashed line represents the uncoated glass substrate of index $n_s=1.52$

way is to modify the film thickness. When the thickness of the film is equal to a quarter-wavelength in optical path difference, the phase difference between two reflected light beams shown in figure 2.4 is 180 degrees and the maximum destructive interference between two beams could occur. Reflectance R will be a minimum. Another way to tune the reflectance is to change the index of the film to modify the amplitudes of the electric field of two reflected light beams. When the electric field amplitudes of two reflected

light beams is equal but reverse, both of them cancel out resulting in a reflectance of R of zero.

If the index of the film does not match the value of $\sqrt{n_0 n_s}$, a thin metallic film can be utilized to compensate by depositing it on the top of the film or in the film/substrate interface [2.10]. This method has been used in this work and will be described in the following section in detail.

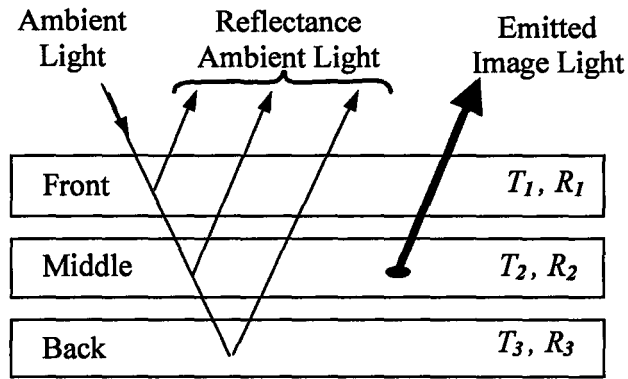
2.4 Contrast Ratio of Displays

Display screens can often be modeled to consist of three parts: the front, middle and back parts shown in figure 2.6 [1.8]. Each part comprises the components that are located in front, within and behind the display. (T_1, R_1, A_1) , (T_2, R_2, A_2) , and (T_3, R_3, A_3) represent a transmittance (T), reflectance (R) and absorption (A) related to each part respectively. Here, T , R , and A take into account possible factors, such as the size of pixel apertures, specular or diffuse reflection, and scattering.

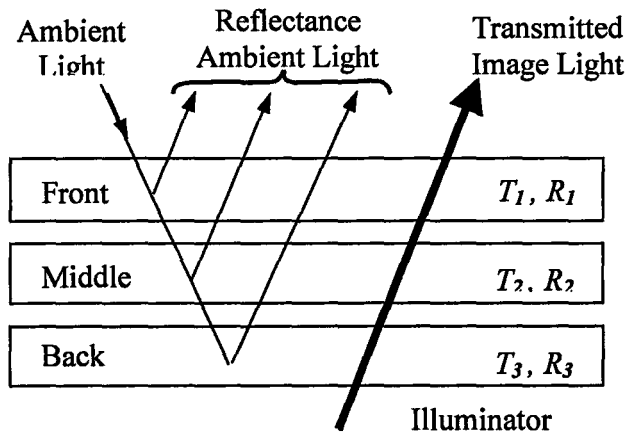
The luminance contrast ratio of a display is defined to be the ratio of the total luminance of the light from the “on” pixel to the total luminance of the light from the “off” pixels [1.8].

$$C = \frac{L_{\text{pixel-on}}}{L_{\text{pixel-off}}} = \frac{L_{EL\text{-on}} + L_{\text{reflect}}}{L_{EL\text{-off}} + L_{\text{reflect}}} \quad (2.30)$$

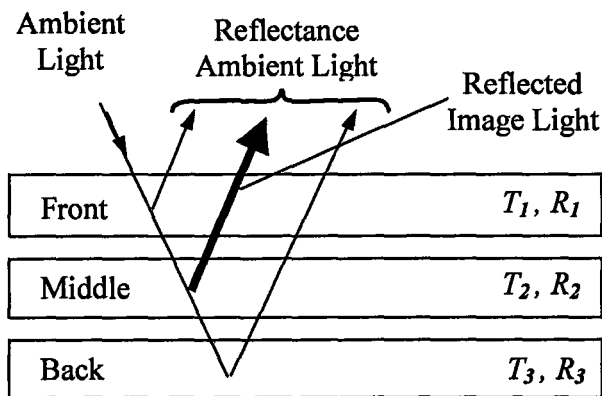
In the above expression, $L_{\text{pixel-on}}$ expresses the luminance of light output from the device with the pixel “on”. For the SSTFEL device, it is the sum of $L_{EL\text{-on}}$ and L_{reflect} . $L_{EL\text{-on}}$ is luminance of light from pixels of the device under the application of an AC



A. Emissive mode



B. Transmissive mode



C. Reflective mode

Figure 2.6 Schematic structures of simplified displays. (A) expresses emissive displays including CRTs, PDPs, FEDs, and TFELs; (B) for the case of transmissive LCDs; and (C) for reflective LCDs

voltage and expressed in repression (2.2), and $L_{reflect}$ is the reflection luminance of ambient light from the surface of SSTFEL devices, which is a product of the reflectance of devices and the illuminance of ambient light, $R * L_{ambient}$; $L_{pixel-off}$ expresses luminance of light output from the device at the pixel “off” while the AC voltage on it is off. It is the sum of L_{EL-off} and $L_{reflect}$. L_{EL-off} is equal to zero due to no light emitted from pixels of the device without the application of the AC voltage. To replace $L_{reflect}$ with $R * L_{ambient}$ and L_{EL-on} with the expression (2.2) in expression (2.30), it becomes

$$C = \frac{\eta}{R} \left(\frac{1}{L_{ambient}} \right) \left\{ \frac{4}{\pi} f \epsilon_0 \epsilon_i \left(\frac{d_p}{d_i} \right) E_{p,th} (V_a - V_{th}) \right\} + 1 \quad (2.31)$$

It is clear that to remove the reflection from the surface and interface is a very effective way to enhance the contrast of displays because this reflection determines the influence of the ambient light on the contrast. R is inversely proportional to contrast ratio of EL devices such as SSTFEL devices. Table 2.1 lists some of the optical coatings used

Table 2.1. Optical coatings for contrast enhancement [1.8].

Display types	Emissive	Non-emissive Transmissive	Non-emissive Reflective
Reduce R_1	AR coating	AR coating	AR coating
Reduce R_2	AR coating Black coating	AR coating	AR coating
Reduce R_3	AR or Black coating	AR coating	AR or Black coating

AR: anti-reflectance

for this purpose. The other way is to increase η of the device. Another important method is to increase the contrast ratio of the device.

It can be seen that contrast ratio is also a parameter relevant to the ambient illuminance level of measurement conditions for EL display devices.

In this work, a two layer AR coating system was selected for improving the contrast ratio of SSTFEL device. It is composed of an ITO layer and ultra-thin gold layer, and deposited on the surface of SSTFEL devices which is shown in figure 2.7(a) and (b) to represent two areas (A, B) of the surface of devices as well as shown in figure 1.5

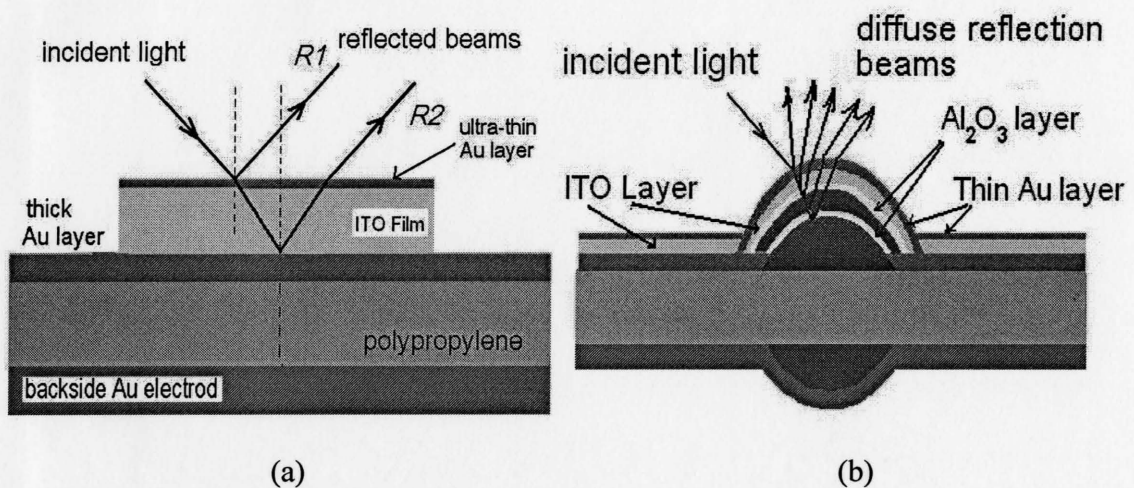


Figure 2.7 Schematic diagrams of specular and diffuse reflections from the surface of the SSTFEL device with AR coatings including two part areas

For this AR coating on the area of part A, which is shown in figure 1.5 as well as in figure 2.7(a), the ITO layer works as a phase tuner to make a phase difference between two reflective light beams ($R1$, $R2$) shown in figure 2.7(a) nearly equal to 180 degrees. The ultra-thin gold layer is utilized to adjust the intensity of reflectance light $R1$ to match closely the intensity of $R2$ in order to reduce reflectance. On the area of part B, which is

shown in figure 1.5 as well as figure 2.7(b) here, the ultra-thin gold layer, the ITO layer, two Al_2O_3 layers and the phosphor layers form an optical system. The thickness of the ultra-thin gold layer, the ITO layer and Al_2O_3 layers could be optimized to reduce the diffuse reflectance light from top areas of BaTiO_3 spheres. It has been reported in [2.11] that the ultra-thin gold layer and the ITO layer can work as AR coatings to reduce specular reflection effectively and enhance the contrast ratio of the electroluminescent device made on planar BaTiO_3 chips.

Chapter 3. The Fabrication Processes of SSTFEL Devices

The fabrication processes of SSTFEL devices and AR coatings are discussed here. During the process, it was found that the efficiency of the green phosphor material on the top area of BaTiO₃ spheres was affected by the sintering temperature of BaTiO₃ spheres and reached up to 1.48 lm/W when BaTiO₃ spheres were sintered at 970°C.

3.1 The Structure of SSTFEL Devices in Detail

The structure of SSTFEL devices with AR coatings is schematically shown in figure 3 1 Thousands of tiny BaTiO₃ spheres (diameter about 50 μm) of high-permittivity dielectrics ($\epsilon_r=1000-6000$) [3 1] are embedded within a polypropylene sheet to form a flexible display device as shown in figure 3 1 On the top area of BaTiO₃ spheres, green-emitting oxide phosphor (Zn₂Si_{0.5}Ge_{0.5}O₄.Mn) with thickness of 500~700nm was deposited by RF magnetron sputtering, which has shown high luminance and luminous efficiency [3.2, 3.3] Two 35nm Al₂O₃ layers are sputtered to

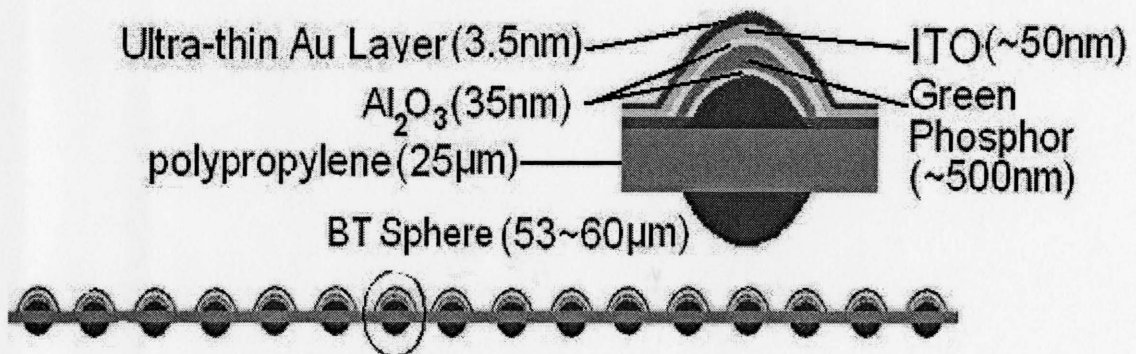


Figure 3 1 A schematic structure diagram of the Sphere-Supported Thin-Film Electroluminescent Device

sandwich this phosphor layer in order to provide charge-injection interfaces [1.7, 2.3, 3.4]. A 45-50nm ITO layer is deposited on the top area of the device to form a conductive and transparent electrode for light to leave from the green oxide phosphor under the application of an AC voltage. Under the ITO layer is a 30nm gold layer for improving the stability of the conductivity of the ITO layer. Because the ITO layer on the polypropylene sheet is easily cracked to result in a big jump in resistance [3.5, 3.6] due to the strain from the bent polypropylene sheet when the polypropylene sheet bends. The AR coatings are composed of an ITO layer and an ultra-thin gold layer that is sputtered directly on the surface of the ITO layer to enhance the contrast ratio of SSTFEL devices. The backside electrode of devices is another gold layer with thickness of 30-60nm, which is not visible to the viewer of display.

3.2 The Fabrication Processes of SSTFEL Devices

3.2.1 Sintering and Patterning BaTiO₃ Spheres

BaTiO₃ spheres used in this work as supporters of deposited phosphors are commercially available from TPL Inc. They are made from BaTiO₃ fine particles with the size of 50nm by spraying drying technology at lower temperature. These BaTiO₃ fine particles could be produced via an aqueous, low temperature process, which results in BaTiO₃ spheres having cubic structure with lower-permittivity dielectrics and hydroxyl defects observed by infrared spectroscopy for BaTiO₃ [3.7]. However, a thermal treatment above 600°C can remove the hydroxyl group. The defects were also liberated with heat treatment in air by sintering at over 800°C [3.8]. The cubic phase of BaTiO₃

spheres changes to the tetragonal phase with high permittivity dielectrics [3.9] after sintering at over 920°C [3.10].

The BaTiO₃ spheres were first selected with the diameter from 63 to 75 μm by meshes, and then were sintered in a furnace within the air atmosphere. A curve in figure 3.2 shows this sintering process. BaTiO₃ spheres were treated at 500°C for 30 minutes in order to remove some residual organic chemical materials adhered on the surface of BaTiO₃ fine particles in the BaTiO₃ spheres; they were then continually sintered at 970°C for 2 hours in order to remove the the hydroxyl group and the defects.

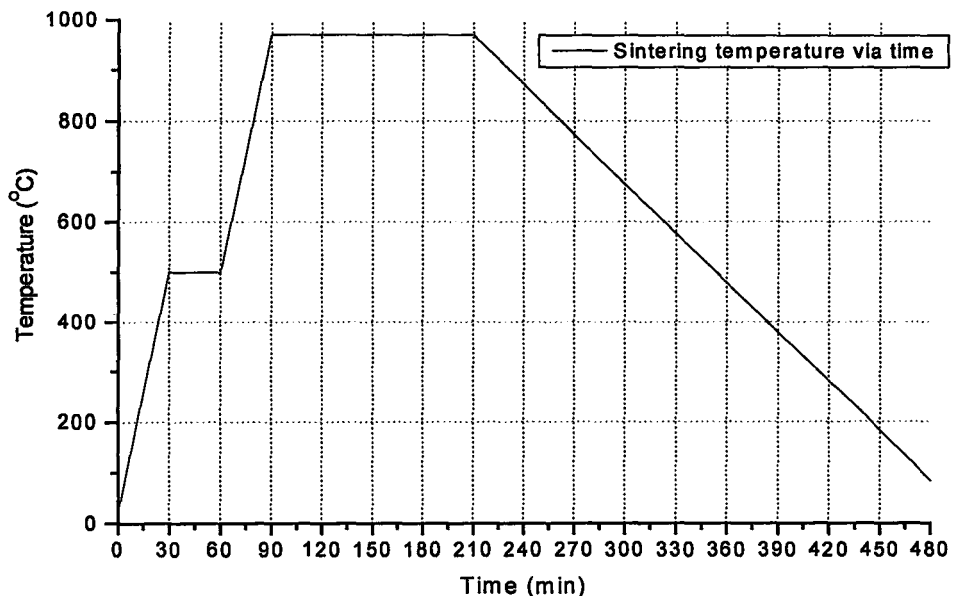


Figure 3.2 a temperature curve of the BaTiO₃ sphere sintering process.

After sintering, the BaTiO₃ spheres become strong enough to be used as supporters and their crystal structure changes to tetragonal phase with a high permittivity dielectric constant of about 4000 [3.10]. The diameter of BaTiO₃ spheres also shrinks in the sintering process. Table 3.1 shows shrinkage information of BaTiO₃ spheres at

different sintering temperatures. It is obvious seen that the shrinkage of BaTiO₃ sphere diameter is larger at high temperature than that at low temperature. More than 30% of BaTiO₃ spheres still have diameter of 63-75μm after sintering in the temperature range from 720°C to 920°C. However this ratio is less than 20% after sintering at temperatures from 1020°C up to 1170°C. Two groups of shrinkage data at the same sintering conditions of 970°C for 2 hours show that the shrinkage ratio of BaTiO₃ sphere diameters is not well predicted even if the sintering conditions are the same. This result indicates that BaTiO₃ spheres are not uniform in green density of BaTiO₃ fine particles, although the sizes of BaTiO₃ fine particles are very tiny, about 50nm. The sintering process can make BaTiO₃ spheres strong. It was also found that sintering temperature also strongly affects the luminous efficiency of green phosphor sputtered on the top area of BaTiO₃ spheres.

Table 3.1: Shrinkage of BaTiO₃ sphere diameter after sintering at high temperature

Diameter	<45μm	45-53μm	53-63μm	63-75μm
720@2hrs	21%	13%	25%	41%
820@2hrs	26%	14%	26%	34%
920@2hrs	3%	5%	49%	43%
(1) 970@2hrs	15%	9%	45%	31%
(2) 970@2hrs	29%	19%	36%	16%
1020@2hrs	23%	15%	48%	15%
1070@2hrs	25%	29%	41%	5%
1170@2hrs	23%	35%	36%	6%

Luminous efficiency of the green phosphors reaches up to 1.48 lm/W when BaTiO₃ spheres were sintered at the temperature of 970°C, and the increment of the luminous efficiency of the green phosphors improves the contrast ratio of the SSTFEL as shown in expression (2.31)

After the sintering process, the more spherically symmetric spheres with the diameter range of 53~63μm were selected, then patterned on a high-purity Al₂O₃ plate with a special array containing cells which consist of a matrix of dents to hold the BaTiO₃ spheres. Figure 3.3 shows this 5x5 matrix of dents with patterned BaTiO₃ spheres. Dents

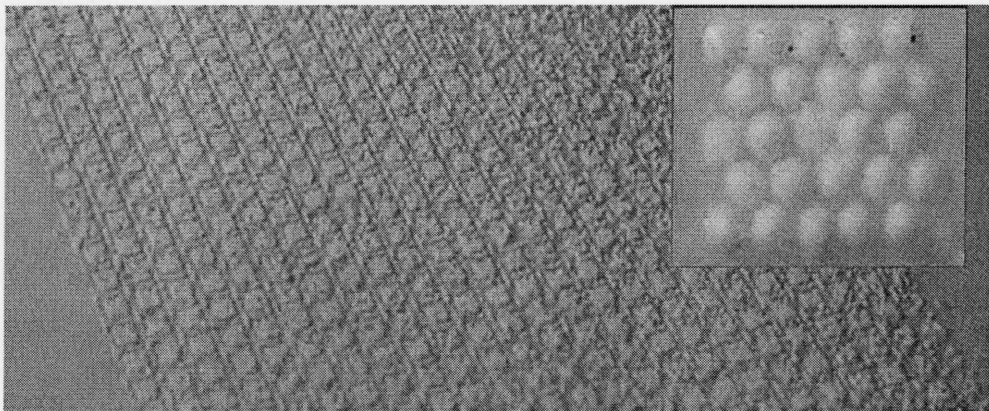


Figure 3.3 Al₂O₃ plate with special arrays of containing cells. Each cell has a matrix of dents with 5x5 pattern. BaTiO₃ spheres were patterned inside dents

on the Al₂O₃ plate have the depth of 20μm with the diameter of 56μm, and interval distance of 15μm between them. They were pre-coated with tiny powders of Polyethylene Glycol 400, and then BaTiO₃ spheres were put into the dents. They were weakly adhered into the dents after the Al₂O₃ plate was heated up to 110°C and then cooled quickly down to room temperature. The sticking force was strong enough to keep spheres stationary during the subsequent sputtering and annealing processes.

3.2.2 Sputtering and Annealing Green Phosphors

After BaTiO₃ spheres were patterned on the Al₂O₃ plate, a sandwich Al₂O₃/Green phosphor/Al₂O₃ was deposited on the top area of the BaTiO₃ spheres by RF magnetron sputtering. Before depositing materials on the top area of BaTiO₃ spheres, an Al₂O₃ target and an oxide green EL phosphor target comprising Zn₂Si_{0.5}Ge_{0.5}O₄:Mn were pre-bombarded at 6mTorr of Ar and O₂ mixed ambience with the flow ratio of 24.5 sccm and 14.5 sccm respectively for 5 minutes in order to clean impurities absorbed on the surface of targets. While sputtering the Al₂O₃ layer and the green phosphor layer, Ar and O₂ flowed into the chamber at the flow ratio of 24.5 sccm and 14.5 sccm respectively to maintain the ratio of 1.7:1 [3.10]. The pressure of the chamber was maintained at 6 mTorr. BaTiO₃ spheres and the Al₂O₃ plate were kept at 250°C for sputtered materials to adhere to the surface of spheres well. Under the RF power of 600W, the Al₂O₃ layer and the green phosphor layer were deposited for 5 minutes and 40 minutes respectively to make the Al₂O₃ layer of 35nm and the green phosphor layer of 600nm.

After phosphor was sputtered on the top area of BaTiO₃ spheres, the annealing process is needed for crystallizing the phosphor layer. BaTiO₃ spheres, still sitting on the Al₂O₃ plate, were annealed at 800°C for 12 hours with an oxygen pressure of 4x10⁻⁴Torr [3.10]. As a result of the series of process described above, BaTiO₃ spheres become green light emitters.

3.2.3 Embedding Process

In order to make devices flexible, BaTiO₃ spheres, as light emitters, were

embedded within a thin and flexible polypropylene sheet with the thickness of only 25 μm . The embedding process is separated into two steps.

First, a 30nm gold layer was deposited on a polypropylene sheet that was used to pick up the BaTiO₃ spheres. The polypropylene sheet was adhered on a silicone elastomer layer of a sheet that is composed of hard polyester backing sheet and a soft silicone elastomer layer, which is called Gel-Pak film, made by Gel-Pak, Inc. This Gel-Pak and polypropylene stack was pressed on BaTiO₃ spheres covered Al₂O₃ plate and heated in N₂ up to 200°C [3 10]. BaTiO₃ spheres penetrate the polypropylene sheet by vertically pressing the sandwich under the pressure of 0.12N/cm² [3 10], and then quickly cooling it because the polypropylene sheet was melted at 200°C. The processing and result are schematically shown in Figure 3.4 (a) and (b), respectively. While cooling to room temperature, the BaTiO₃ spheres were embedded tightly within this thin

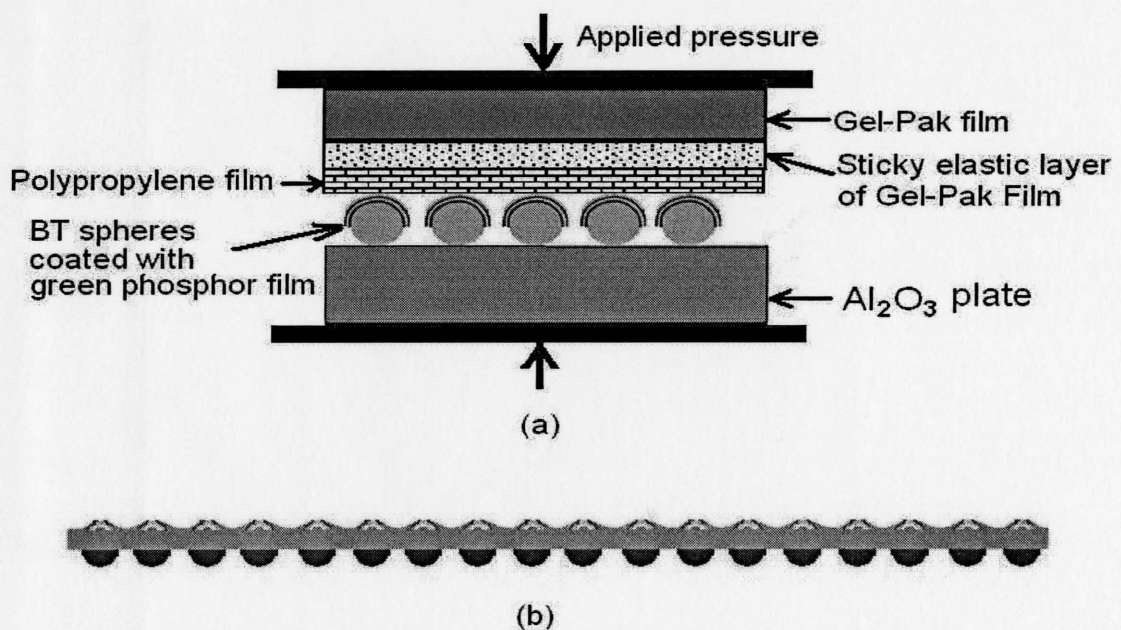


Figure 3.4 Schematic diagrams of the embedding process (a) and resultant (b) in first step.

polypropylene sheet. However, BaTiO_3 spheres were not symmetrically located in the polypropylene sheet as shown in figure 3.4(b).

The second step is to push the thin polypropylene sheet into the middle of BaTiO_3 spheres. The device was sandwiched between two Gel-Pak films shown in figure 3.5(a), heated up to 173°C , and then quickly cooled down to room temperature under a pressure of $2.21\text{N}/\text{cm}^2$ [3 10] on this sandwich structure. A basic structure of flexible display devices is shown in figure 3.5(b). Because the adhesive layer of Gel-Pak film is elastic and deforms under pressure, it can effectively protect the top and bottom area of spheres from being covered with a polymer sheet. Moreover, the polypropylene sheet with embedded spheres could be easily peeled off from this adhesive layer without any damage.

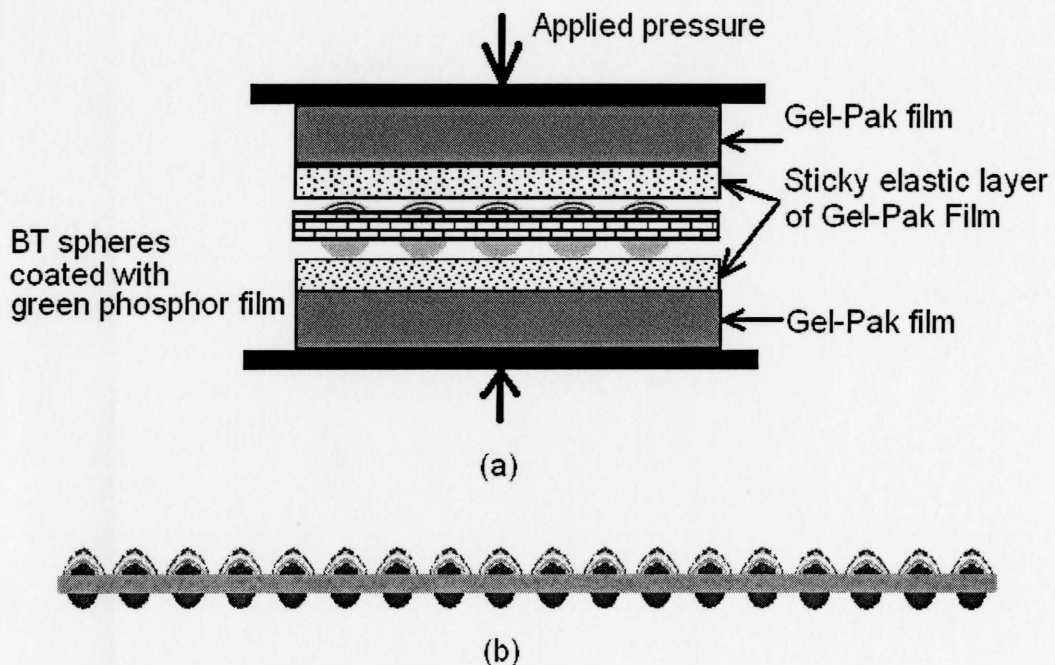


Figure 3.5 Schematic diagrams of embedding processes (a) and resultant (b) in the second step.

3.2.4 Sputtering AR Coating and Electrodes

A transparent ITO electrode layer with thickness about 450nm was deposited on the top area of the device. The ITO target was an $\text{In}_2\text{O}_3:\text{SnO}_2$ (90:10wt%) ceramic target. It was also pre-sputtered 5 minutes before the ITO layer was deposited on the surface of devices. Typical sputtering conditions are shown in Table 3.2. The RF power must be

Table 3.2 Sputtering conditions of ITO film

Sputtering Parameters	Value
Chamber pressure (mTorr)	0.5
RF Power (W)	30
Ar Flow (sccm)	7.0
Substrate Temperature	Room temperature

lower than 30W. If RF power was set at 45W, the atoms of the target had more kinetic energy to impact on the surface of devices, which resulting in the increase of the temperature of the devices during the 4-minute sputtering process. As a result, the polypropylene sheet of devices cracked and wrinkled as show in figure 3.6. The transparent ITO electrode layer deposited on the surface of SSTFEL devices also works as a dielectric layer of AR coatings on the SSTFEL device. This AR coating is a composite of this ITO layer and an ultra-thin gold layer with thicknesses of 45nm and 3.5nm respectively. The ultra-thin gold layer was sputtered on the surface of the ITO layer by Edwards Sputter Coater S150B. The sputtering was performed at a ratio of about

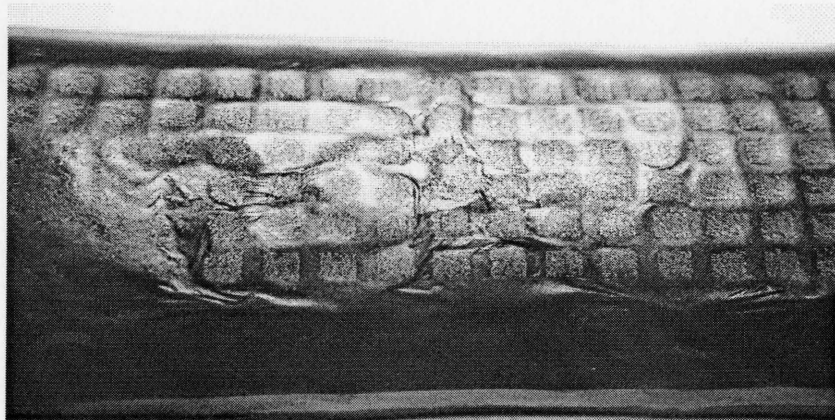


Figure 3.6 The image shows that the high RF power can crack and wrinkle the polypropylene sheet of devices by heating sample during the ITO deposited process

18nm/min in 0.18 Torr argon ambient with RF power of 30W on a 99.99% gold target (17).

Another gold layer with the thickness of 60nm was sputtered on the backside of the device as the backside electrode of the device as shown in figure 1.2. However, the stickiness between this gold layer and the polypropylene sheet is not good. A sandwich structure of the electrode composed of ITO layers and sandwiched gold ultra-thin layers was developed to improve the stickiness between the electrode and the polypropylene sheet. The ITO film was deposited on the backside of the polypropylene sheet, for enhancing the stickiness between the backside electrode and the polypropylene sheet.

Based on the optimization of sintering temperature of BaTiO₃ spheres and AR coating technology, a SSTFEL display device with high efficiency about 1.48Lm/W was fabricated and is shown in figure 3.7. Two vertical bright strips on the device surface do not have AR coatings for the 3.5nm gold layer is not present on the bright strips, and their reflectance is very high. Dark areas have been deposited the 3.5nm ultra-thin gold layer

to form AR coatings on this areas. It can be seen that AR coatings obviously reduce the reflection of ambient light from the surface of the SSTFEL device.

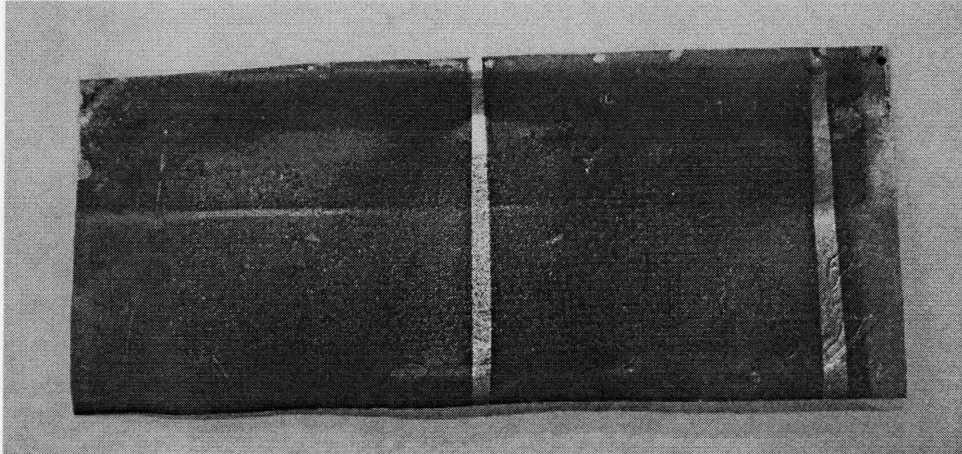


Figure 3.7 An image shows the SSTFEL device with AR coating under office illumination.

Chapter 4 Experimental (I) and Discussion

(Depositions and characterizations of the ITO film and the ultra-thin gold film)

An ITO layer and an ultra-thin gold layer deposited on the surface of the SSTFEL device not only work as a transparent and conductive electrode but also as layers of AR coatings in this work. The thickness of the ultra-thin gold layer and the ITO layer should be optimized to reduce the reflectance of the ambient light from the surface of SSTFEL devices. As reported in [4.1, 4.2, 4.3, 4.4], optical and electric properties of ITO films are particularly sensitive to the deposition conditions. Refractive index, transmittance and sheet resistance of the ITO films with thickness ranging from 30 to 60 nm have been measured and reported in this chapter. The optical and electric properties of the ultra-thin gold films also have been studied. AFM technology was used to explore the surface morphology of ultra-thin gold layer on Si substrates and on polypropylene sheets. Experimental results show that the ultra-thin gold film has unexpected electric property when its thickness is around 3nm.

4.1 ITO Optical and Electrical Characteristics

Because the chamber pressure and RF power directly affect the index, and the transprence and the sheet resistance of the ITO layer, it is necessary to optimize the sputtering conditions for lower sheet resistance and higher transprence of the ITO layer. On the other hand, controlling the thickness of the ITO layer is also very important to make it as a layer in AR coatings. Therefore, ITO layers were deposited on Si substrates

for their index and thickness to be measured with PZ2000 ellipsometry. Before ITO films were deposited on the surface of Si substrates, Si substrates were etched for 40 seconds in the HF and H₂O mixed solution of 1:40 (wt%) to remove a naturalized SiO₂ film on the surface of Si substrates. Then ITO films were sputtered on the fresh surface of Si substrates.

4.1.1 The Thickness of ITO Films Relevant to Deposition Conditions

Several groups of ITO layers sputtered on Si substrates were measured and Figure 4.1 shows measurement results of their thickness related to sputtering times under deposition conditions with the same chamber pressure of 0.5mTorr, the same Ar flow ratio of 7.0sccm, but different RF powers of 30W (a), 45W (b) and 60W (c). Whether the RF power is 30W, 45W or 60W, the thickness of the ITO layer always linearly increases with the increment of the sputtering time. The higher the RF power, the faster the

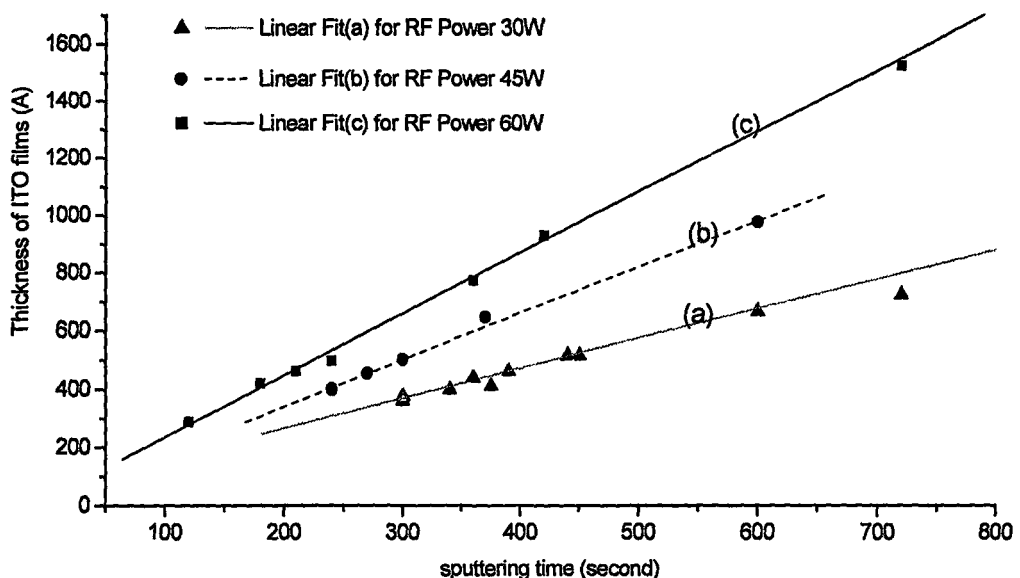


Figure 4.1 Thickness of ITO films via the sputtering times under different RF Powers

deposition rate of the ITO film. The deposition ratios are (1.03 ± 0.05) Å/sec for 30W, (1.60 ± 0.04) Å/sec for 45W and (2.12 ± 0.08) Å/sec for 60W, respectively.

The deposition rate of ITO films relevant to RF power is shown in figure 4.2. It increases linearly from (0.85 ± 0.05) Å/sec to (2.20 ± 0.08) Å/sec as RF power increases from 20W to 60W while other deposition conditions are kept unchanged.

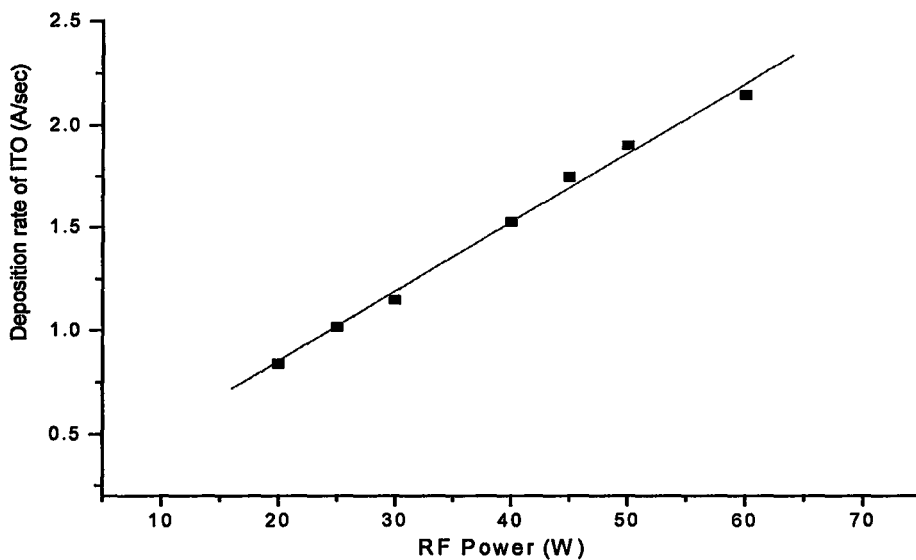


Figure 4.2 Deposition rates of ITO films via the RF Powers

Figure 4.3 shows the deposition rate of ITO films relevant to the chamber pressure. It can be seen that the deposition rate of ITO films increases up to about 1.32 Å/sec as the chamber pressure increases from 0.3mTorr to 0.6mTorr, then decreases as the chamber pressure increases moreover from 0.8mTorr.

In the lower chamber pressure, the density of ionized Ar^+ located near the surface of the ITO target is less than that in higher chamber pressure, which results in the atoms bombed out of the ITO target less and target's atoms arriving on the surface of the

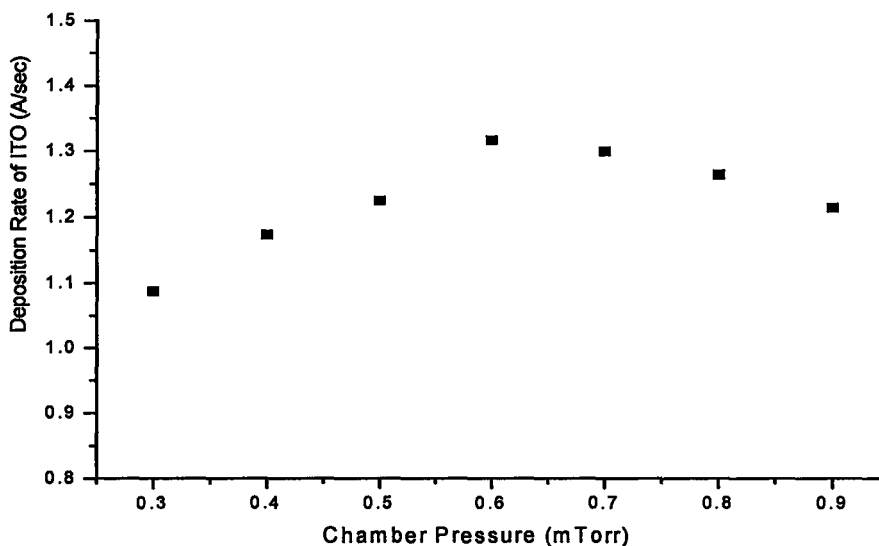


Figure 4.3 Deposition rates of ITO films via the chamber pressures

substrate less. Thus the deposition rate of ITO films on the substrate is lower at the lower chamber pressure. Under the high chamber pressure, the density of ionized Ar^+ is much higher and results in the atoms bombed out of the ITO target much more. Thus, there are more target's atoms towards to the surface of substrate to increases the deposition rate.

However, as high chamber pressure increases moreover, some of these atoms are diffused away by the ionized Ar^+ with higher density near the surface of the target and cannot reach the surface of the substrate, which causes the deposition rate of ITO films to decrease as the chamber pressure increases from 0.8 to 0.9 mTorr as shown in figure.4.3.

4.1.2 Electric Properties of ITO Films Relevant to Deposition Conditions.

The sheet resistance of ITO films decreases as the thickness of ITO films increases while the sputtering conditions remain unchanged. The measurement results of ITO sheet resistance via different RF powers and chamber pressures are shown in

figure 4.4 and 4.5. Because the R_{\square} is a parameter related to the ITO thickness, a parameter $R_{\square} * d_{ITO}$ is introduced as a unit of the vertical axis for comparing the conductive property of ITO films. R_{\square} and d_{ITO} are the sheet resistance and the thickness of ITO films respectively. $R_{\square} * d_{ITO}$ can be seen as resistivity of ITO films. It can be seen that the resistivity of ITO films have a lower value in the region of RF power 25-45W, while the resistivity of ITO films are higher when the RF power is lower than 25W and higher than 50W to 60W.

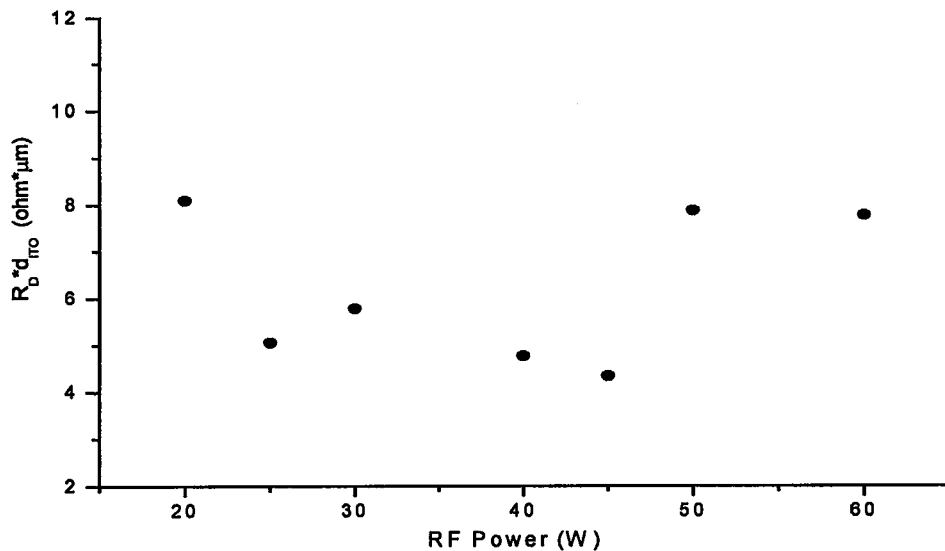


Figure 4.4 Resistivity of ITO films are relevant to RF power under sputtering conditions with chamber pressure of 0.5mTorr and Ar flow ratio of 7.0sccm

The resistivity of ITO films shown in figure 4.5 almost keeps a constant value for the chamber pressure from 0.3mTorr to 0.6 mTorr. Then, its value increases as the chamber pressure increases and rises quickly as the chamber pressure is larger than 0.7mTorr.

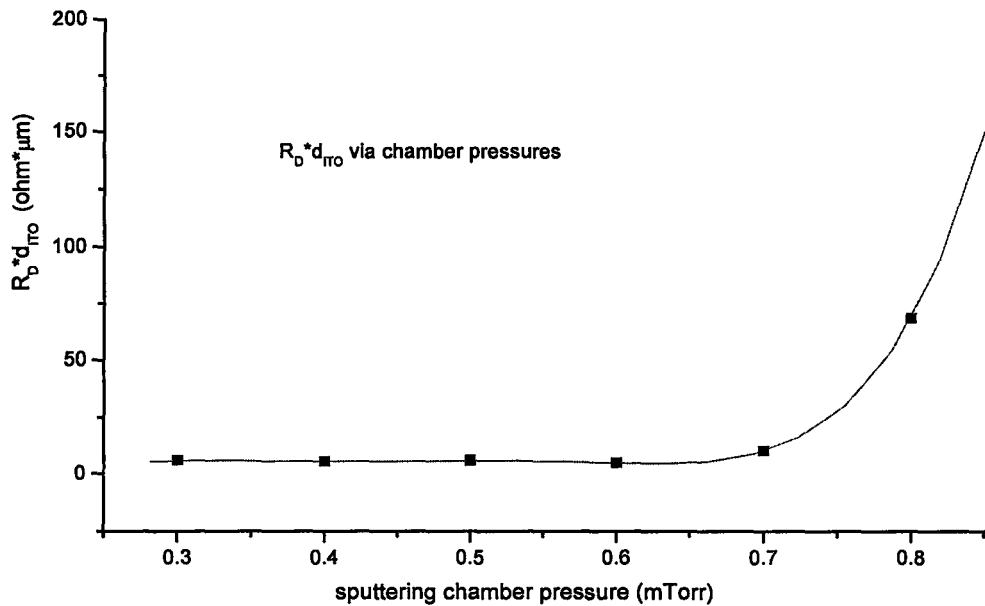


Figure 4.5 Resistivity of ITO films are relevant to the chamber pressure under sputtering conditions with RF power of 30W and Ar flow ratio of 7.0sccm

4.1.3 Refractive Index of ITO Films Relevant to Deposition Conditions

The refractive index and transmittance of ITO film are important parameters for the design of AR coatings, and conductive and transparent electrode layer. Figure 4.6, figure 4.7 and figure 4.8 show the refractive index of ITO films via deposition conditions of the sputtering time, RF power and the chamber pressure. It can be seen in figure 4.6 that the index of ITO films does not keep a constant for the thickness of ITO films from 300 Å to 1000 Å whether the RF power is 30W, 45W or 60W. For the RF power of 45W and 60W, the change of ITO index is large in the thickness range of ITO films less than 500 Å. The index of the ITO film increases as thickness increases, then goes towards a constant value when the thickness of ITO films is over 500 or 600. But for the RF power of 30W, the index difference of ITO films is not larger than 0.03 as the thickness of ITO

films varies in the region from 300Å to 700 Å. Therefore, it can be reasonably decided that the index of ITO films may be approximated by an average value of 1.97 under the deposition conditions with the chamber pressure of 0.5mTorr and RF power of 30W

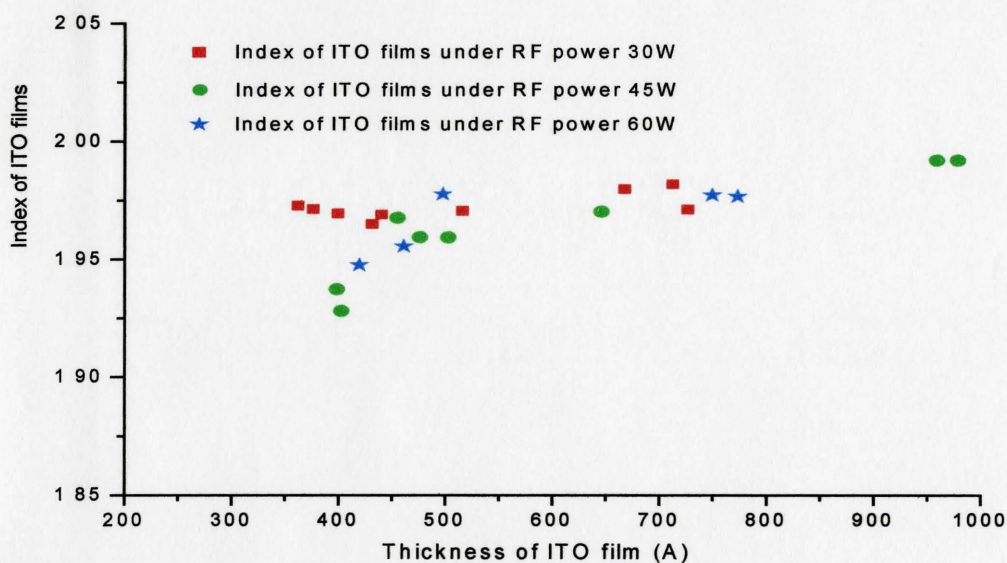


Figure 4.6 Index of ITO films fabricated via thickness under different RF powers but the same chamber pressure of 0.5mTorr

Data in the figure 4.7 show the relationships between the index of ITO films and RF power under deposition conditions with the chamber pressure of 0.5mTorr and sputtering time of 360 seconds. The index of ITO films decreases quickly at first as the RF power increases from 20W to 30W, then increases slowly as the RF power increases from 30W to 60W

To maintain RF power of 30W and change the chamber pressure, it can be seen in figure 4.8 that the index of ITO films almost remains a constant in the region of the chamber pressure from 0.3mTorr to 0.5mTorr, and increases as the chamber pressure increases from 0.6 mTorr

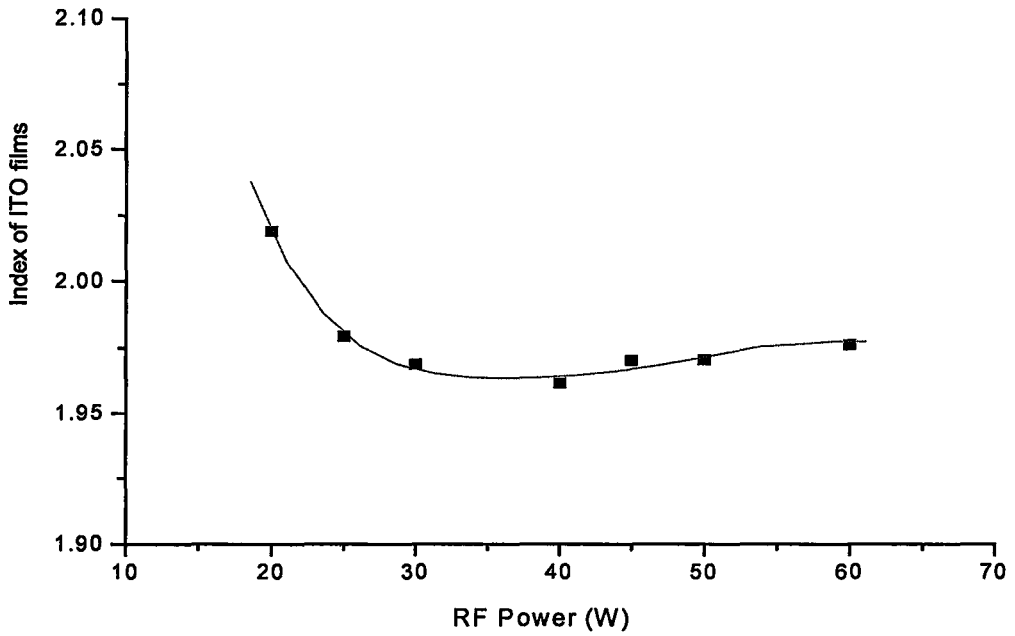


Figure 4.7 Index of ITO films is relevant to the RF power under sputtering conditions with the chamber pressure of 0.5mTorr and Ar flow ratio of 7.0sccm

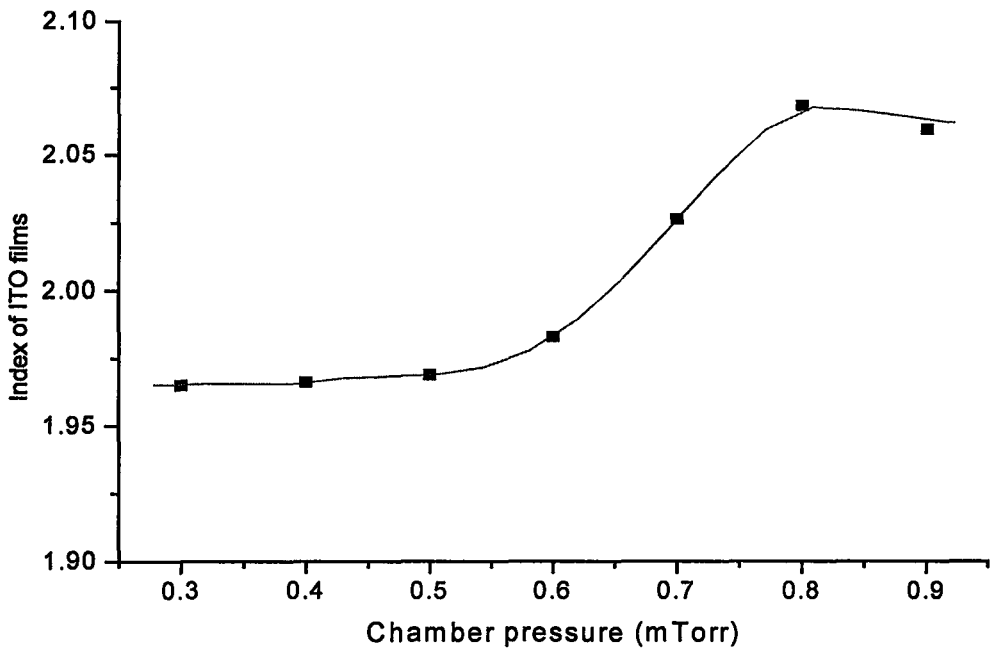


Figure 4.8 Index of ITO films is relevant to the chamber pressure under sputtering conditions with RF power of 30W and Ar flow ratio of 7.0sccm

4.1.4 Transmittance of ITO Films Relevant to Deposition Conditions

The transmittance spectra of ITO films were measured by Cary 50 Probe UV-Visible Spectrophotometer. ITO films were deposited on glass slide substrates with different sputtering conditions. As shown in figure 4.9, the transmittances of ITO film

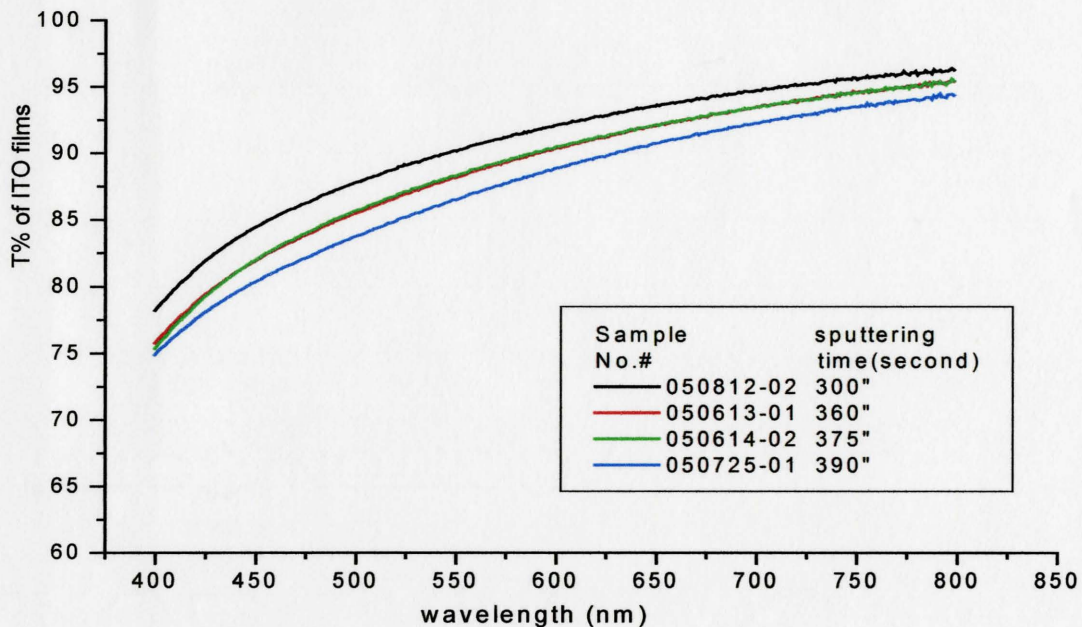


Figure 4.9 Transmittance spectra of ITO films with different RF power, but the same chamber pressure of 0.5mTorr

decrease as the deposition time increases, and also as the thickness of ITO films increases. The decrease of transmittances of ITO film is shown by the whole spectral curve moving down in visible wavelength range, but the shape of curves almost does not change. The transmittance is larger than 75% in the region from 400nm to 700nm and larger than 80% at the wavelength up to 450nm if the sputtering time is less than 6 minutes.

In figure 4.10, it can be seen that the transmittance of the ITO film decreases as the chamber pressure increases. However, the thickness of the ITO film also increases

when the chamber pressure increases from 0.3mTorr to 0.6mTorr. As we knew, the thicker the ITO film, the lower the ITO transmittance. The small change of ITO

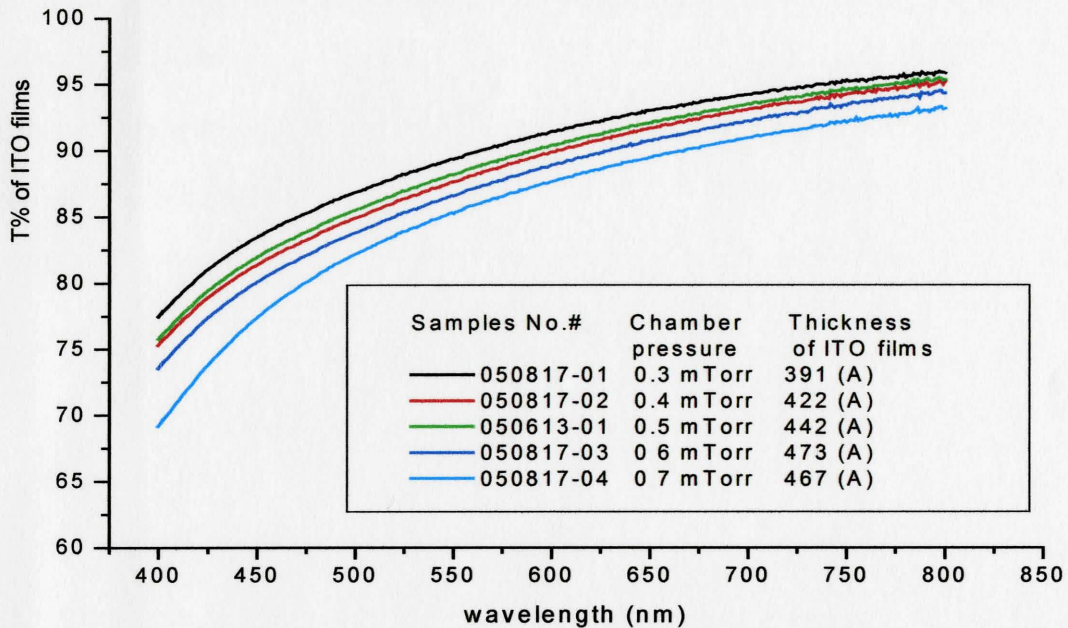


Figure 4.10 Transmittance spectra of ITO films deposited under different chamber pressures, but at the same RF power of 30 W and the same sputtering time of 6 minutes.

transmittance indicates that the chamber pressure has little effect on the transmittance of ITO films while it increases from 0.3mTorr to 0.6mTorr. However, the chamber pressure significantly affects the transmittance of the ITO film when it is as high as 0.7mTorr. The transmittance of the ITO film deposited at the chamber pressure of 0.7mTorr is smaller than that of the ITO film deposited at the chamber pressure at 0.6mTorr, but the thickness of the ITO film deposited at the chamber pressure of 0.7mTorr is less than the thickness of the ITO film deposited at the chamber pressure of 0.6mTorr as shown in figure 4.10.

Similarly, the RF power affects the transmittance of ITO films when ITO films were deposited under the higher RF power. As RF power is 90W, the transmittance

spectrum of the ITO film shown in figure 4.11 is totally different from other transmittance spectra obtained at lower RF powers. Not only does the shape of this spectrum curve change, but also it is much lower than that deposited at lower RF powers in the wavelength ranging from 500nm to 700nm, although, it is higher at the short wavelength region below 450nm.

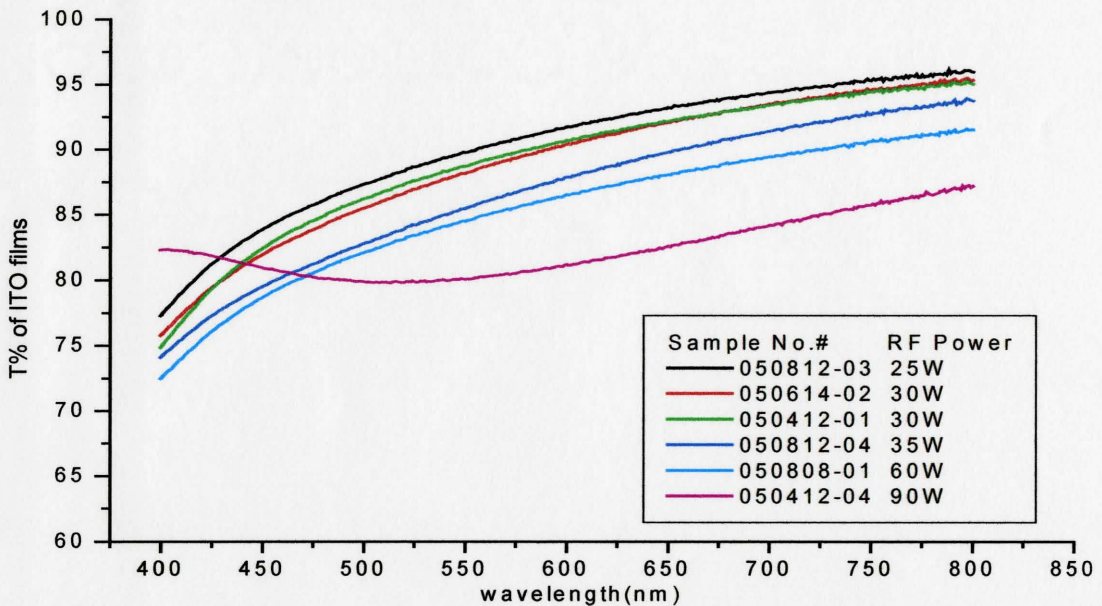


Figure 4.11 Transmittance spectra of ITO films deposited under different chamber pressures, but the same RF power of 30 W and the same sputtering time of 6 minutes

Other transmittance spectra of ITO films are similar in the shape of spectrum curve while RF power is lower than 60W. Two curves obtained at the same RF power of 30W are very close, which indicates that the repeatability of the sputtering process is very good for ITO transmittance. On the other hand, transmittance of an ITO film deposited under RF power of 30W is higher than that of an ITO film deposited at RF power of 35W, although the differences of deposition rate between them are small, as shown in figure 4.2.

Finally, considering electric and optical properties and relevant deposition conditions, the deposition conditions with RF power of 30W, the chamber pressure of 0.5mTorr and Ar flow ratio of 0.7sccm are best to sputter ITO films as a conductive and transparent film for SSTFEL devices. ITO film deposited for 6 minutes under such conditions has transmittance larger than 75% at short wavelength 400nm and over 80% at the wavelength ranging from 450nm to 800nm, high conductive and lower sheet resistance of 131.2 ± 6.1 (ohms per square) at the and the index about 1.97 while its thickness is $(425 \pm 29) \text{Å}$.

4.2 Characteristics of Ultra-Thin Gold Film

Various growth techniques and morphology of an ultra-thin metal layer including gold, silver, copper and aluminum have been reported [4.5, 4.6, 4.7, 4.8]. They were utilized in the fabrication of filters, AR coatings [2.11] and gas sensors [4.7]. In this work, ultra-thin gold layers were sputtered on the substrates at room temperature by using an S150B Sputter Coater. All sputtering conditions except sputtering time were kept unchanged for all samples. The chamber pressure was kept at 0.18Torr with Argon atmosphere, sputtering current of 20mA and voltage of 1.2kV. AFM was used to measure the thickness of ultra-thin gold films and explore their morphology.

4.2.1 Surface Morphology of ultra-thin gold films

The results of AFM measurements over a scanning area of 500nm x 500nm and $1 \mu\text{m} \times 1 \mu\text{m}$ on ultra-thin gold films deposited on the Si substrate are shown in this

section. Before sputtering, Si substrates were cleaned at first, and then treated in HF:H₂O mixed solution with 1:40 (wt%) for 40 seconds to remove a naturalized SiO₂ film on the surface of Si substrates.

There are five group of images in figure 4.12 from page 49 to 53, which represent a series of ultra-thin gold films deposited ranging from 5 second (5") to 40 second (40"). In each group, there are three AFM images viewed from different angles. The fourth image is the thickness measurement of this ultra-thin gold film. The step in the fourth image was scratched for the thickness measurement by moving a pointed end of a tweezers on the surface of the ultra-thin gold film.

In figure 4.12(a), with sputtering time of 5 seconds, the thickness of ultra-thin gold film is $2.98 \pm 0.15 \text{ nm}$. It can be seen that the ultra-thin gold film is composed of tiny islands distributing densely and separately on the surface of the Si substrate, which agrees with the literature [4.9]. As the sputtering time increases to 8 seconds, the thickness of ultra-thin film is $3.84 \pm 0.19 \text{ nm}$, and tiny gold islands become bigger and contact with each other as shown in figure 4.12 (b). These islands are still clearly distinguishable while the sputtering time increases up to 18 seconds, resulting in a thickness of ultra-thin gold film of about $6.55 \pm 0.33 \text{ nm}$, several tiny islands connect with each other to form an island chain as shown in figure 4.12(c). The morphology of the ultra-thin gold film obviously shows that the film is composed of island chains forming separate regions, not islands. The separate regions disappear in figure 4.12 (d) when the sputtering time increases up to 25 seconds and the island chains grow bigger. However, the boundary among island chains can still be identified. Therefore, the gold film is not a continuous

film. In figure 4.12(e), it is obviously seen that there are many bright points on the surface of gold island chains from the top-view of AFM image. They are new tiny isolated islands forming on the top of island chains, which can be also seen in previous reports [4.9, and 4.10]. It is similar to existing growth models such as the Volmer-Weber model [4.11, 4.12]. It could be assumed that a new layer begins to form over the islands chains before these islands chains form a continuous film, and this type of layer, which is composed of numerous island chains, stacks one by one to form a continuous film in the macroscopic structure.

The thickness of ultra-thin gold films versus the sputtering times is shown in figure 4.13. It is linear as expected, and the sputtering rate is 0.29 ± 0.01 (nm/sec).

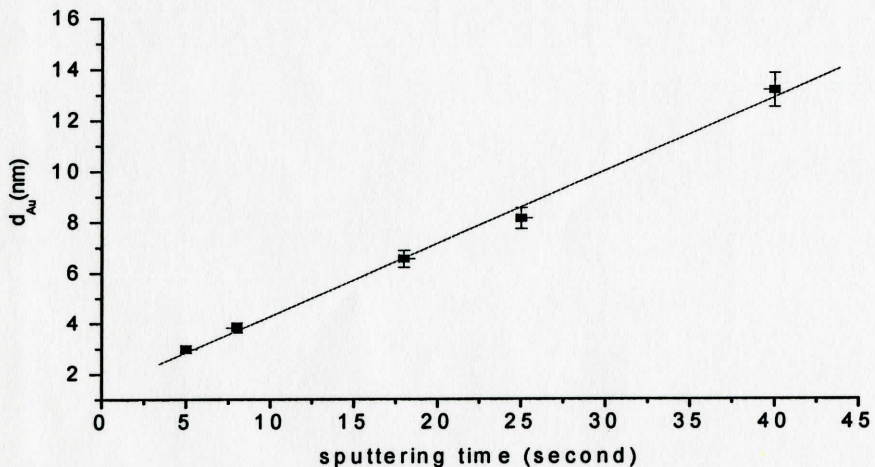
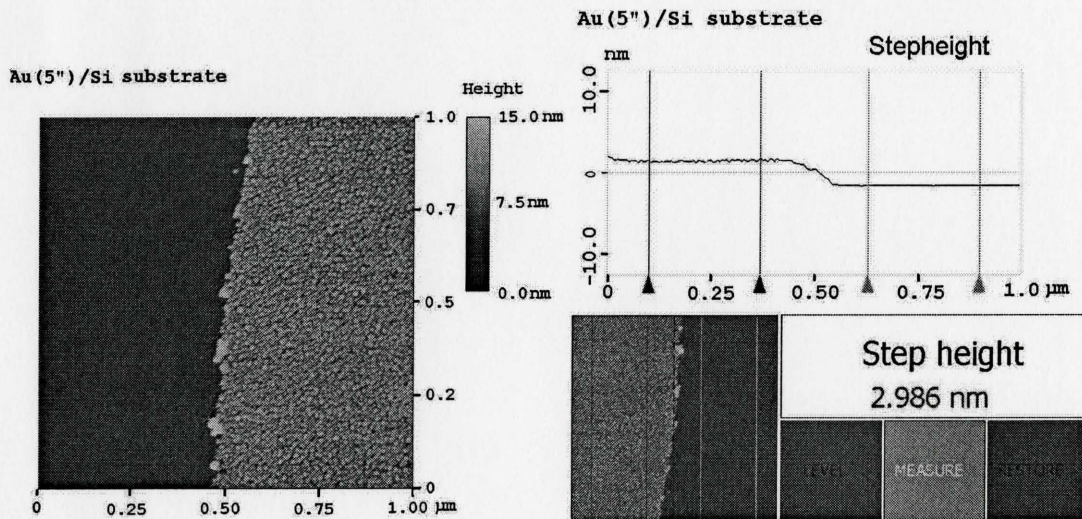
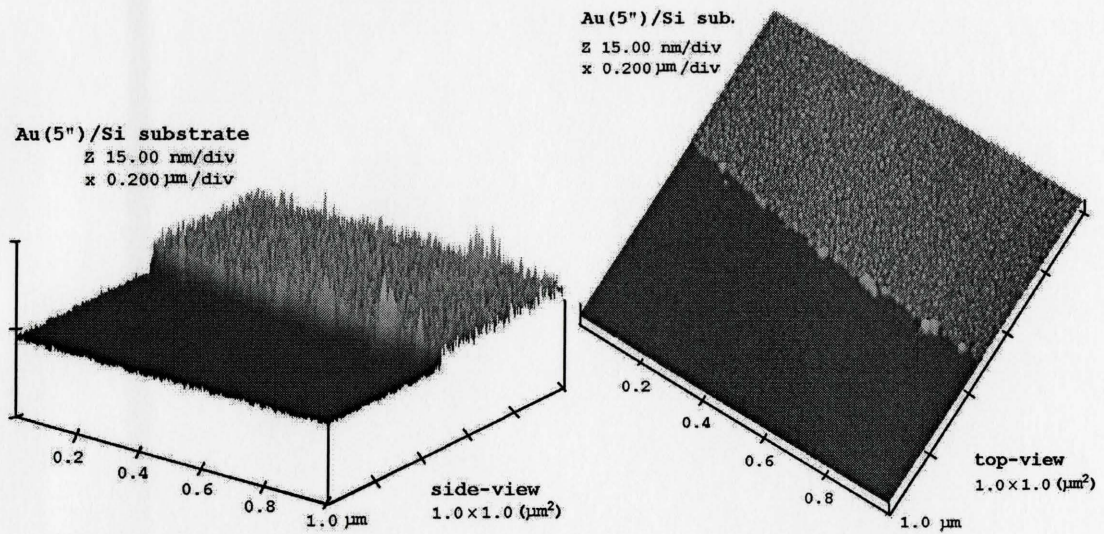


Figure 4.13 Thickness of Ultra-thin gold film via the sputtering times

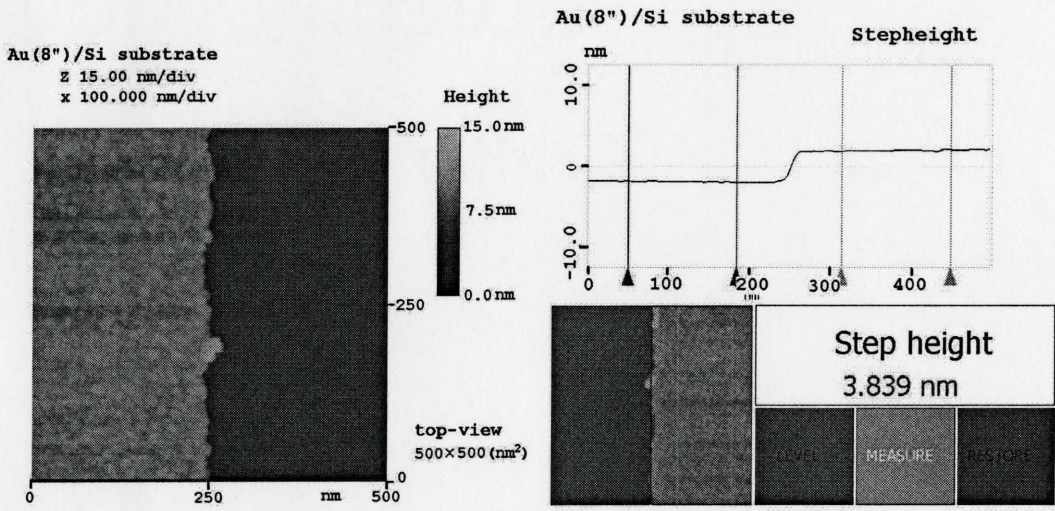
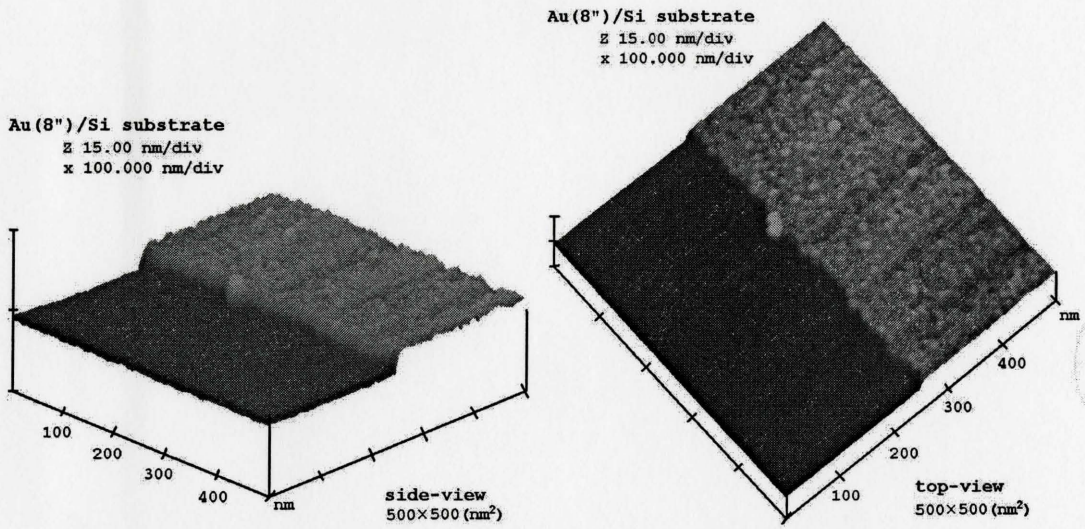
The morphology of ultra-thin gold films deposited on the surface of ITO/Si substrates and ITO/Au/polypropylene sheets was scanned by AFM over an area of 500nm x 500nm, which are shown in figure 4.14 from page 54 to 56. Although the surface of the ITO layer shown in figure 4.14(a) is not as smooth as the surface of Si substrates, shown

in the dark color area in side-view images of figure 4.12, the morphology of the ultra-thin gold film on the surface of ITO layers is still similar to that of the ultra-thin gold film sputtered on the Si substrates. As the sputtering time increases from 7 seconds to 35 seconds, the ultra-thin gold film at first is composed of tiny isolated gold islands distributed densely on the surface of ITO layers shown in figure 4.14(a), and these islands become bigger in figure 4.14(b) as the sputtering time reaches 10 seconds; then the islands connect together to form island chains when sputtering time increases to 15 seconds shown in figure 4.14(c). Because dimensions of X, Y and Z axes in figure 4.14 are 500nm x 500nm in X and Y axis, and 5nm in Z axis different from that in figure 4.12, which are 1 μ m x 1 μ m and 15nm respectively, thus the morphology of ultra-thin gold films in figure 4.14 looks different from that in figure 4.12. However, bright points on the surface of gold islands are also seen in figure 4.12(e). It can be assumed that the formation of a continuous thick gold film involves stacking by layers, which are composed of island chains.

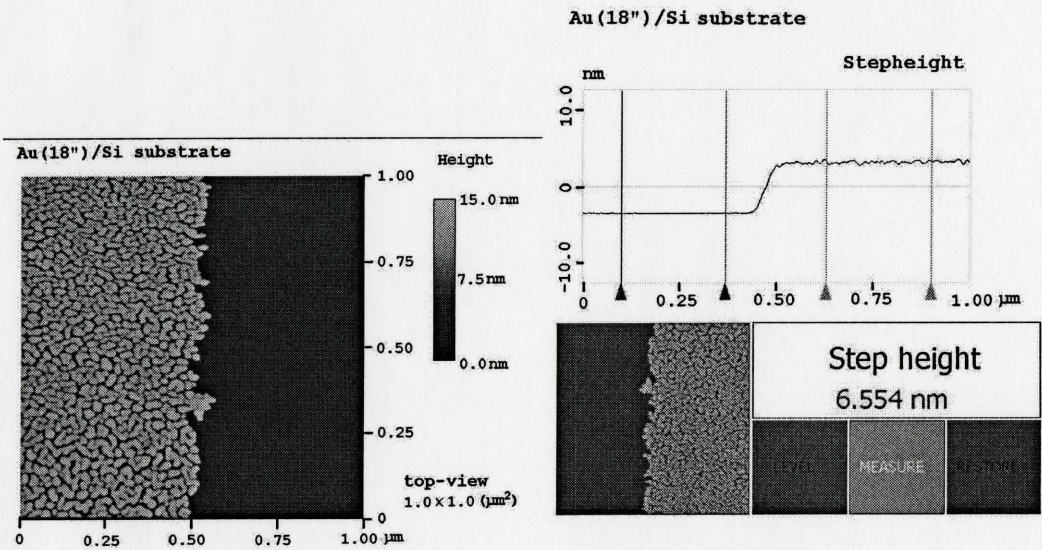
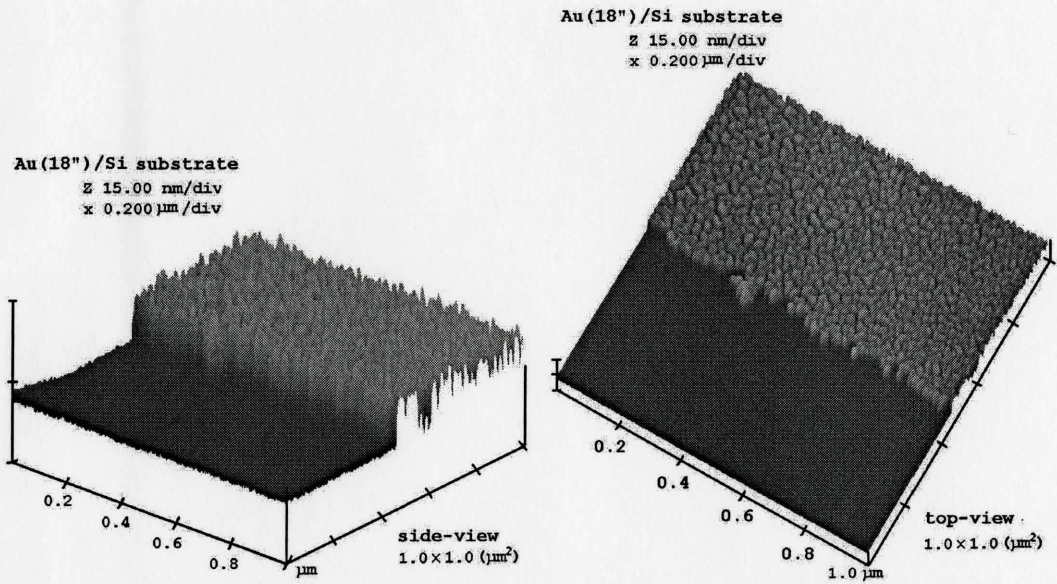
While an ultra-thin gold film was sputtered on the surface of ITO films on the polypropylene sheet, its morphology is similar to that on Si substrates or on ITO/Si substrates. After annealing at 200°C, the smooth surface of the polypropylene sheet becomes wavelike. The wavelike morphology does not change when an ITO film was sputtered on its surface at room temperature. After an ultra-thin gold layer was sputtered on the top of the ITO layer with 7 seconds, tiny gold islands distributed on this wavelike surface as on the surface of Si substrates, which is shown in figure 4.14 (f). The morphology of the ultra-thin gold layer does not change.



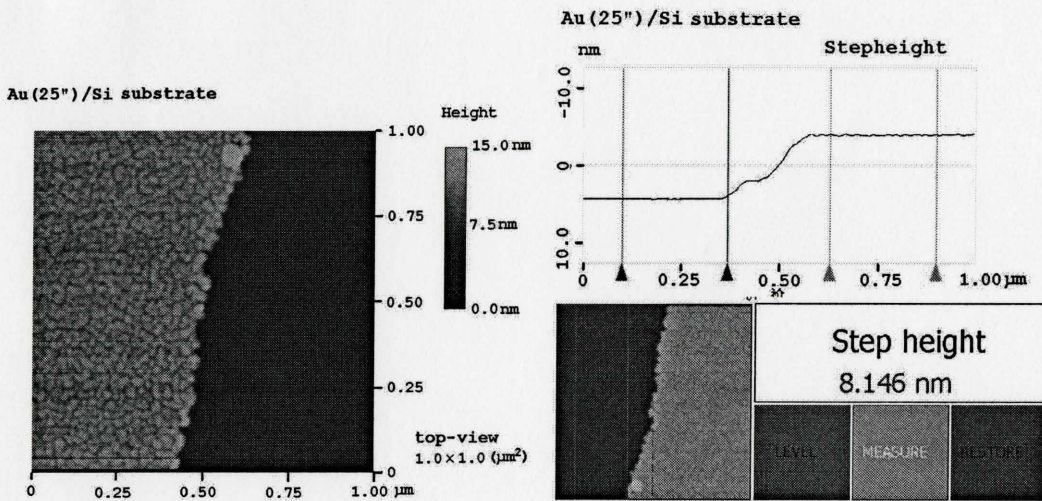
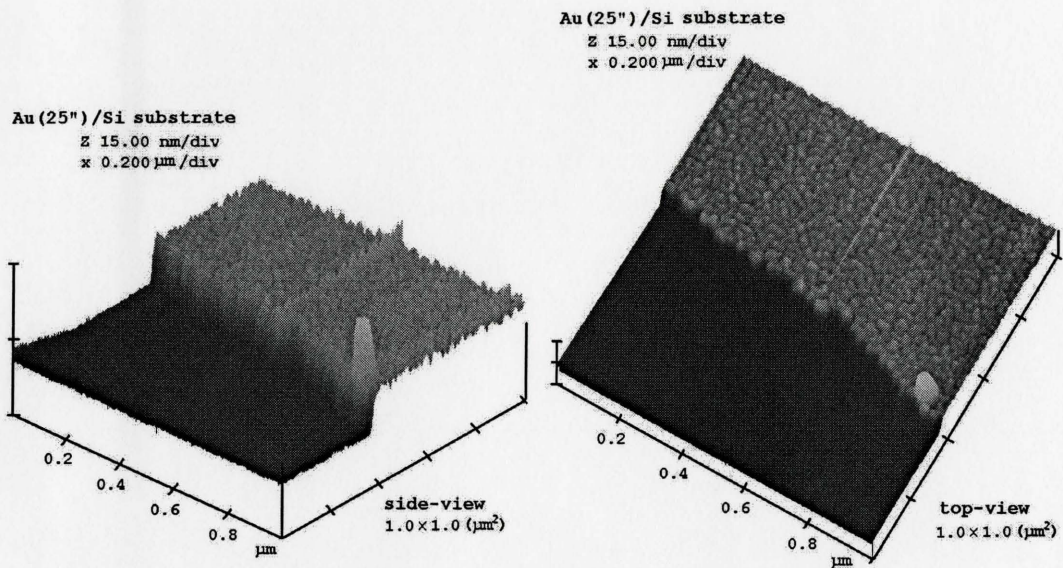
(a)



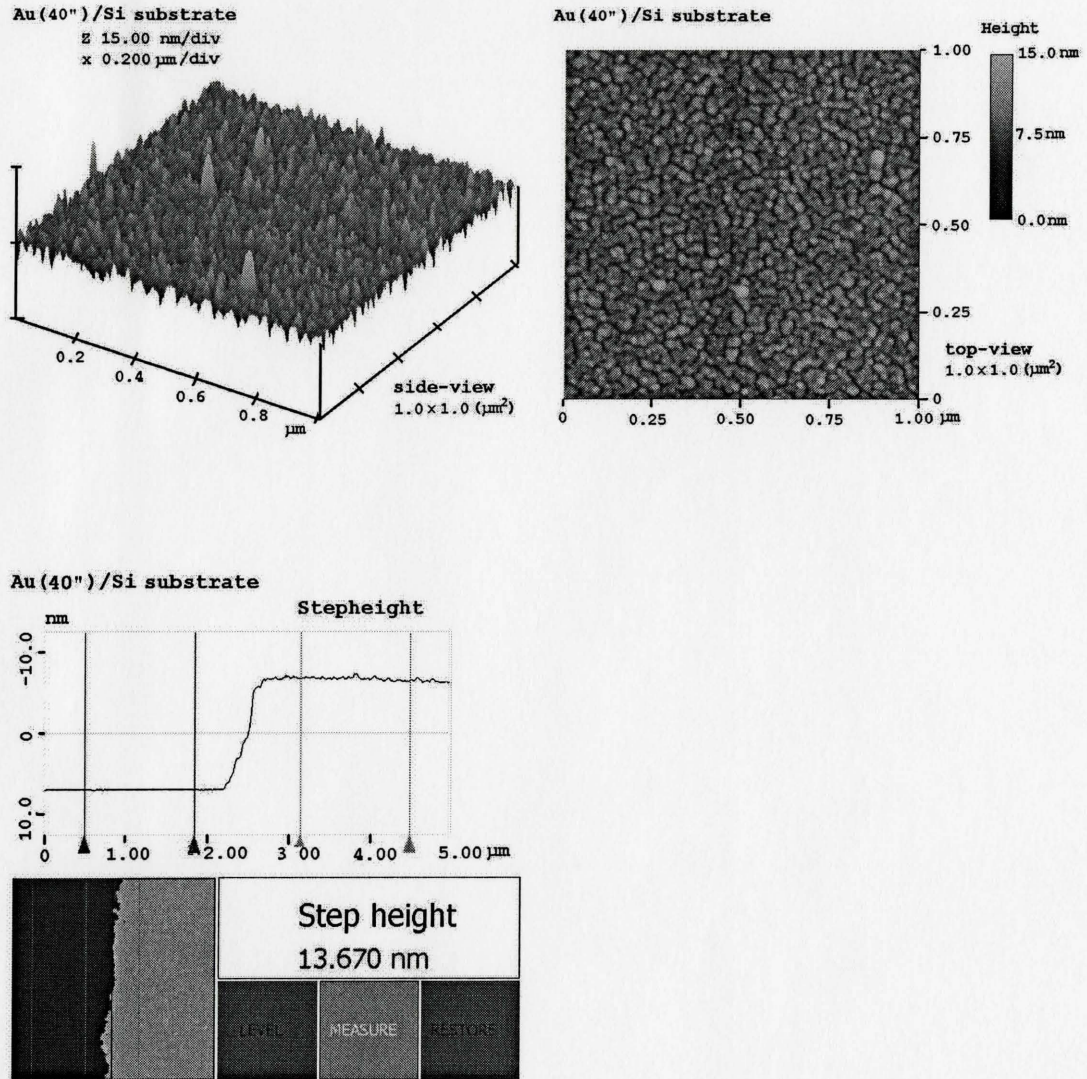
(b)



(c)

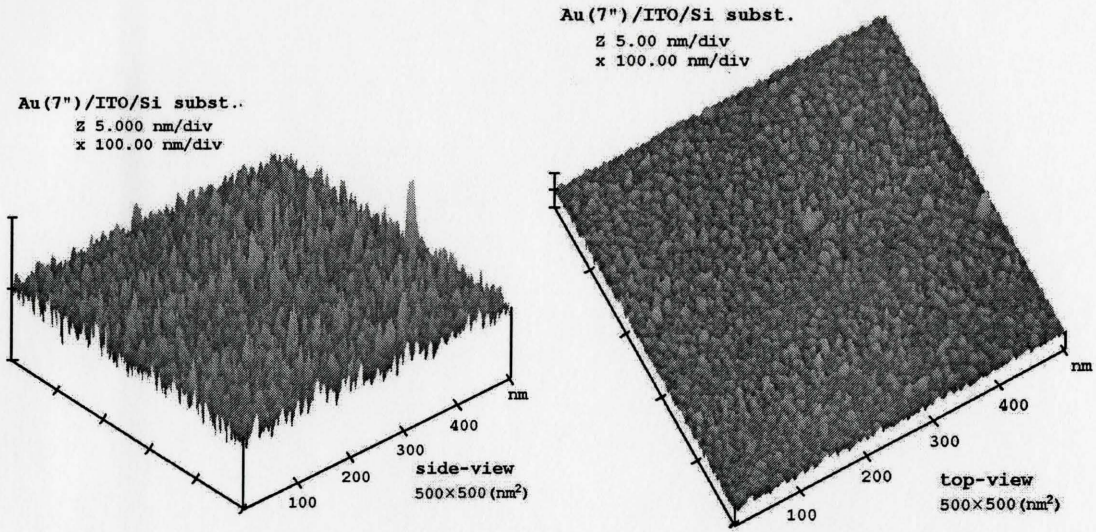


(d)

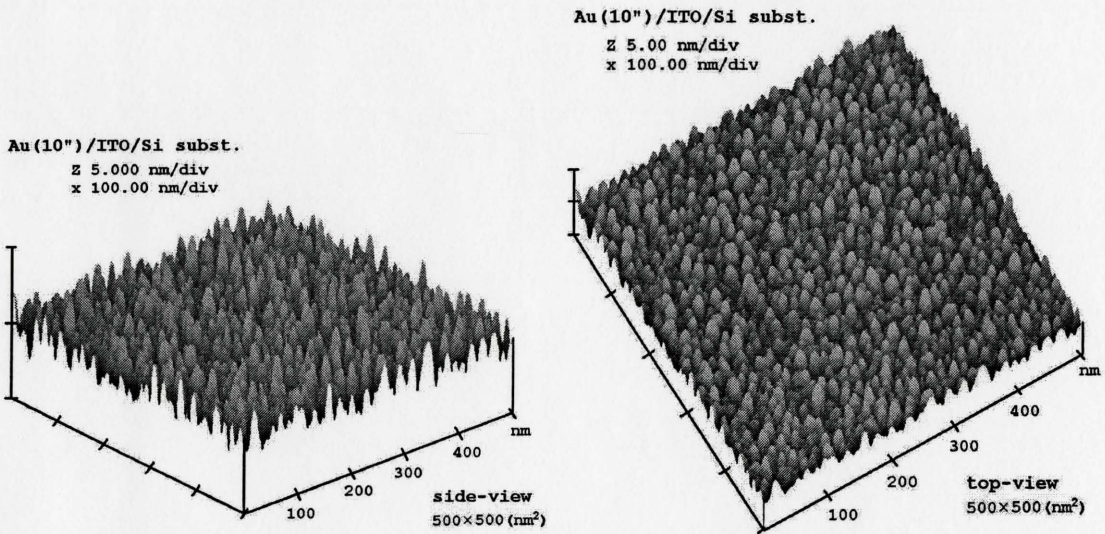


(e)

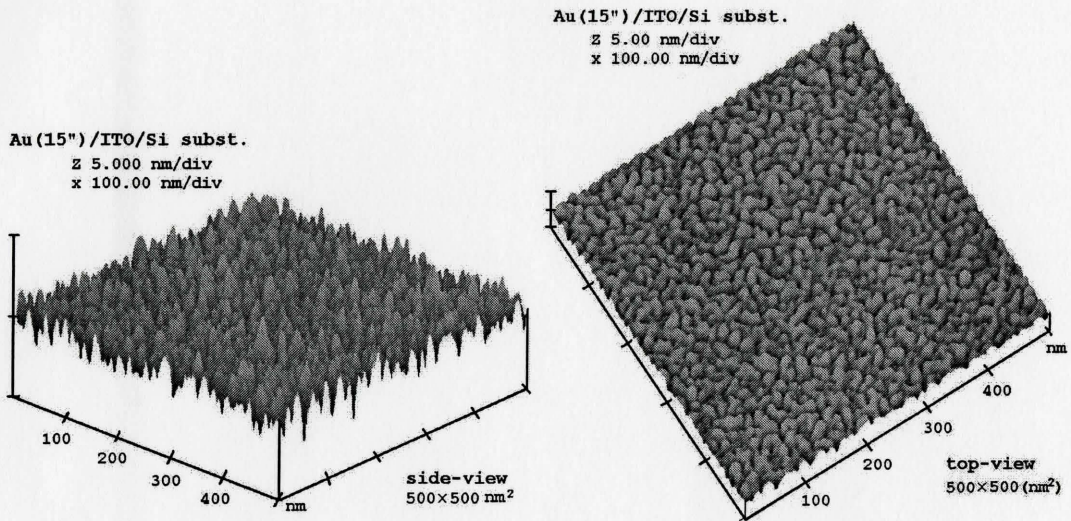
Figure 4.12 The images of AFM scanned over $1 \times 1 \mu\text{m}^2$ on ultra-thin gold films sputtered on Si substrates ranging from 5 seconds (or 5'')(a), 8 seconds (or 8'')(b) to 40 seconds (or 40'')(f). Each group has four images. Three of them are images viewed from different angles. One in the right-bottom is the measurement result of thickness of the relevant ultra-thin gold films.



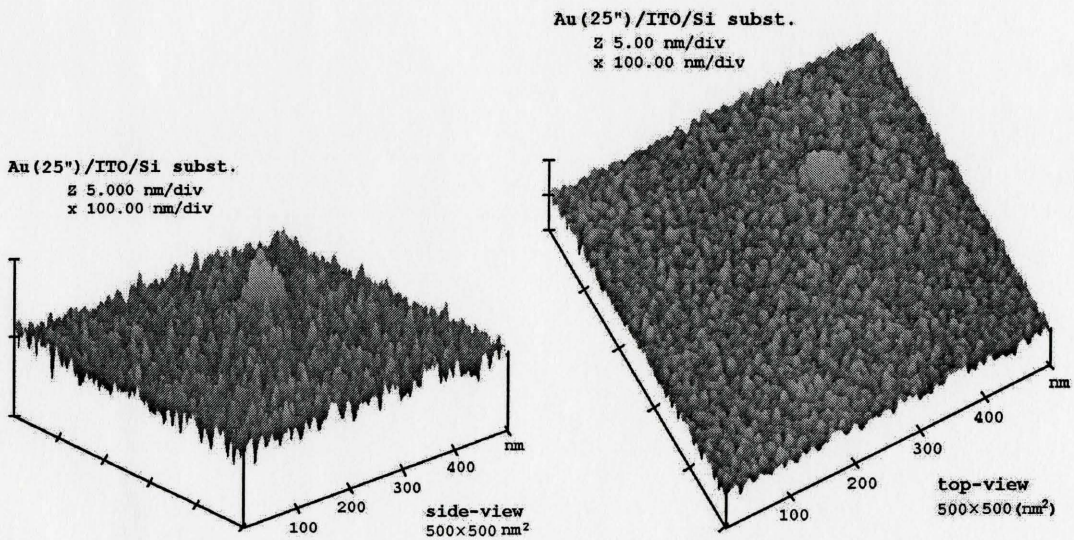
(a)



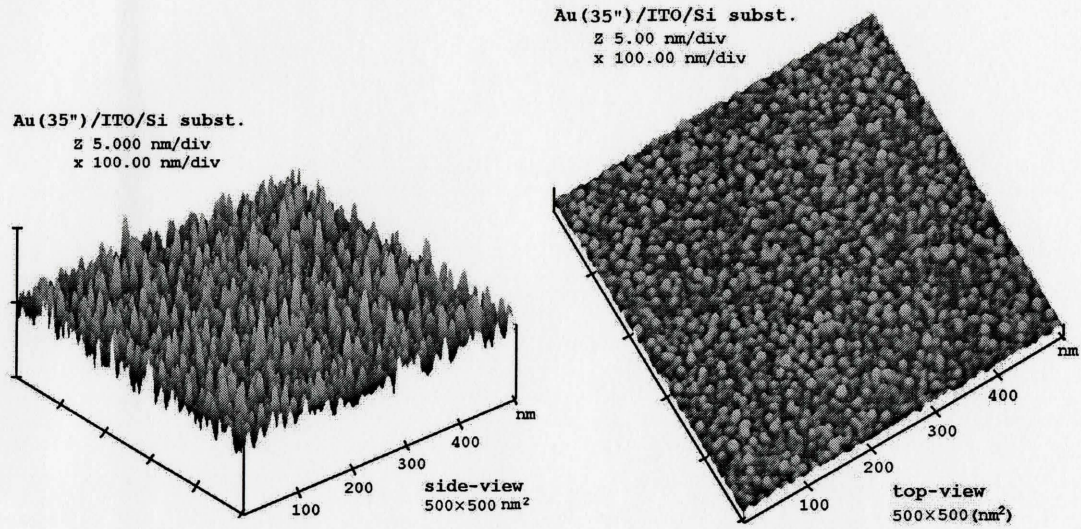
(b)



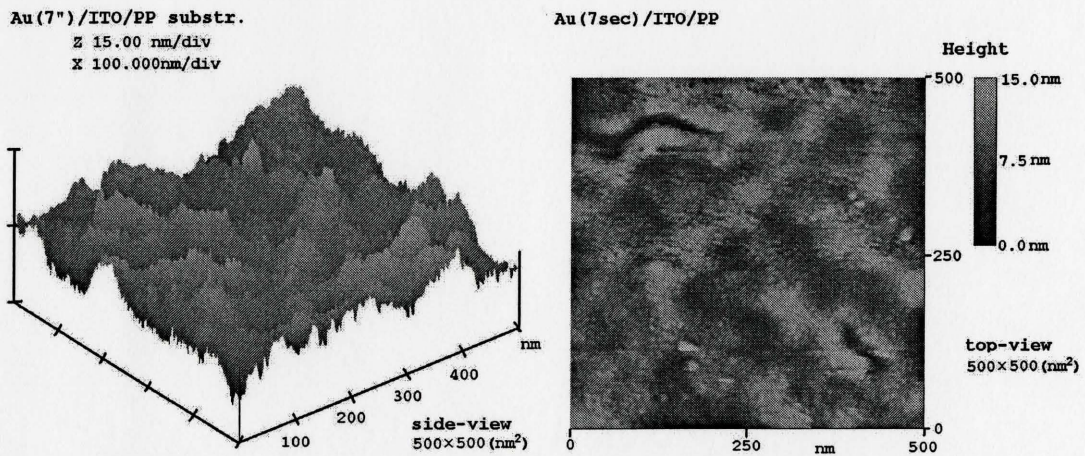
(c)



(d)



(e)



(f)

Figure 4.14 the images of AFM scanned over 500x500nm² of ultra-thin gold films sputtered on the surface of ITO layer on Si substrates ranging from 7 seconds (or 7'') (a), 10 seconds (10'') (b), 15 seconds (15'') (c) to 35 seconds (35'') (e). (f) is the image of ultra-thin gold films sputtered on the surface of ITO layer on a polypropylene sheet. Each group has two images viewed from top and side views.

4.2.2 Electric Properties of Ultra-Thin Gold Films

In the structure of SSTFEL devices, the top electrode is composed of three layers on the surface of polypropylene sheets as shown in figure 3.1. Three layers are a thick gold layer (30nm), an ITO layer and an ultra-thin gold layer. In the part A region of device surface shown in figure 2.7(a), as well as in figure 1.5, the conductivity is mainly determined by the thickness of the gold film. Its sheet resistance is much lower than the sheet resistance of the ITO layer and the ultra-thin gold layer. However, on the top of BaTiO₃ spheres as shown in figure 2.7(b), as well as part B region in figure 1.5, the electrode is only composed of two layers, which are the ITO layer and the ultra-thin gold layer. Measured results show that these two layers contribute the conductivity of this electrode.

Tables 4.1 and Table 4.2 are the results of the sheet resistance measured with a 4-point probe on two group samples. In these samples, ITO films were first deposited on glass substrates under sputtering conditions of RF power of 30W, chamber pressure of 0.5mTorr and sputtering time of 6 minutes; then ultra-thin gold films were sputtered from 3 seconds to 60 seconds on the top of ITO films. Before sputtering ultra-thin gold films, the sheet resistances of ITO films on each glass substrate were measured. The total sheet resistances of two layers were measured quickly after ultra-thin gold films were sputtered for the ultra-thin gold film is very active in atmosphere. As shown in figure 4.15 and Table 4.1, data of the first group indicates that the conductance of the ultra-thin gold layer dominates the conductance of the composite AR coatings when the sputtering time of the ultra-thin gold layer is more than 20 seconds. However, the ultra-thin gold layer

Table 4.1* Sample voltages measured with 4-point probe and relevant calculated resistance (ohms/per square) for group 1.

Sample Number #	Sputtering time	V1 (mV)	V2 (mV)	V3 (mV)	V(average) (mV)	$R_{\square}(\Omega/\square)$	$R_{Au\square}(\Omega/\square)$
050825-1	ITO 6' 30"	233.6	233.7	232.5	233.3 ± 5.7	105.7 ± 3.0	
	Au 4"	216.7	219.5	220.0	218.7 ± 5.1	99.1 ± 2.7	1590.4 ± 698.8
050825-2	ITO 6' 30"	257.9	255.3	255.1	256.1 ± 6.7	116.0 ± 3.4	
	Au 7"	237.2	234.0	235.7	235.6 ± 6.2	106.7 ± 3.2	1335.7 ± 458.7
050825-3	ITO 6' 30"	254.0	253.6	255.5	254.4 ± 6.2	115.2 ± 3.2	
	Au 10"	236.8	233.2	233.8	234.6 ± 6.5	106.3 ± 3.3	1367.6 ± 482.3
050825-4	ITO 6' 30"	245.9	247.3	247.4	246.9 ± 5.9	111.8 ± 3.1	
	Au 15"	133.7	131.8	132.0	132.5 ± 4.0	60.0 ± 2.0	129.6 ± 6.6
050825-5	ITO 6' 30"	260.5	257.4	257.9	258.6 ± 6.8	117.1 ± 3.5	
	Au 20"	58.4	58.5	58.4	58.4 ± 1.5	26.3 ± 0.8	34.2 ± 0.9
050825-6	ITO 6' 30"	244.1	245.1	244.4	244.5 ± 5.6	110.8 ± 3.0	
	Au 30"	28.0	28.0	27.8	27.9 ± 1.1	12.7 ± 0.5	14.3 ± 0.4
050825-7	ITO 6' 30"	255.2	256.6	257.9	256.6 ± 6.4	116.2 ± 3.3	
	Au 45"	18.2	18.0	17.9	18.0 ± 0.9	8.2 ± 0.4	8.8 ± 0.3
050825-8	ITO 6' 30"	257.3	261.7	261.1	260.0 ± 7.2	117.8 ± 3.7	
	Au 60"	15.1	15.1	15.0	15.1 ± 0.8	6.8 ± 0.4	7.3 ± 0.2

*: Voltages of samples are measured by a 4-point probe measurement system at the current of 10.00mA. Every sample was measured twice when ITO on a glass slide and au ultra-thin gold layer on ITO/Glass and displayed in two rows respectively. $R_{Au\square}$ is equivalent sheet resistance of the ultra-thin gold layer.

Table 4.2* Sample voltages measured by 4-point probe and relevant calculated resistance (ohms/per square) for group 2.

Sample Number#	Sputtering time	V1	V2	V3	V4	V5	V (average)	$R_{\square} (\Omega/\square)$	$R_{Au\square} (\Omega/\square)$
051110-1	ITO 6' (V)	0.328	0.327	0.325	0.321	0.328	0.326 ± 0.008	147.6 ± 4.2	
	Au 3" (mV)	316.4	315.4	315.8	314.9	315.7	315.6 ± 4.0	143.0 ± 2.7	4585.1 ± 3923.3
051110-2	ITO 6' (V)	0.330	0.330	0.329	0.329	0.330	0.330 ± 0.006	149.3 ± 3.4	
	Au 5" (mV)	307.3	307.5	307.4	307.4	307.8	307.4 ± 3.5	139.3 ± 2.5	2075.1 ± 756.4
051110-3	ITO 6' (V)	0.322	0.322	0.325	0.324	0.325	0.324 ± 0.007	146.6 ± 3.8	
	Au 7" (mV)	304.5	305.2	306.0	305.7	307.3	305.7 ± 4.3	138.5 ± 2.7	2509.4 ± 1171.2
051110-4	ITO 6' (V)	0.321	0.318	0.322	0.323	0.323	0.321 ± 0.007	145.6 ± 3.8	
	Au 9" (mV)	300.1	298.1	299.8	300.4	300.2	299.7 ± 4.1	135.8 ± 2.7	2012.8 ± 772.6
051110-5	ITO 6' (V)	0.310	0.310	0.310	0.309	0.309	0.310 ± 0.006	140.3 ± 2.0	
	Au 11" (mV)	268.2	268.7	268.5	267.5	267.5	268.0 ± 3.5	121.4 ± 2.3	905.5 ± 162.3
051110-6	ITO 6' (V)	0.325	0.325	0.325	0.326	0.33	0.326 ± 0.007	147.8 ± 3.8	
	Au 14" (mV)	229.0	225.8	225.3	226.7	226.6	226.6 ± 3.9	102.7 ± 2.3	336.6 ± 26.3
051110-7	ITO 6' (V)	0.352	0.352	0.349	0.349	0.349	0.350 ± 0.008	158.6 ± 4.2	
	Au 17" (mV)	171.1	171.1	170.5	170.0	169.7	170.4 ± 2.3	77.2 ± 1.5	150.5 ± 6.2
051110-8	ITO 6' (V)	0.336	0.338	0.338	0.336	0.339	0.337 ± 0.006	152.8 ± 3.5	
	Au 25" (mV)	107.2	105.8	105.8	105.7	105.6	106.0 ± 2.0	48.0 ± 1.1	70.0 ± 2.2

*: Voltages of samples are measured by a 4-point probe measurement system at the current of 10.00mA. Every sample was measured twice when ITO on a glass slide and au ultra-thin gold layer on ITO/Glass and displayed in two rows respectively. $R_{Au\square}$ is equivalent sheet resistance of the ultra-thin gold layer.

almost does not contribute to the conductance of the composite AR coatings if the sputtering time of the ultra-thin gold layer is less than 10 seconds.

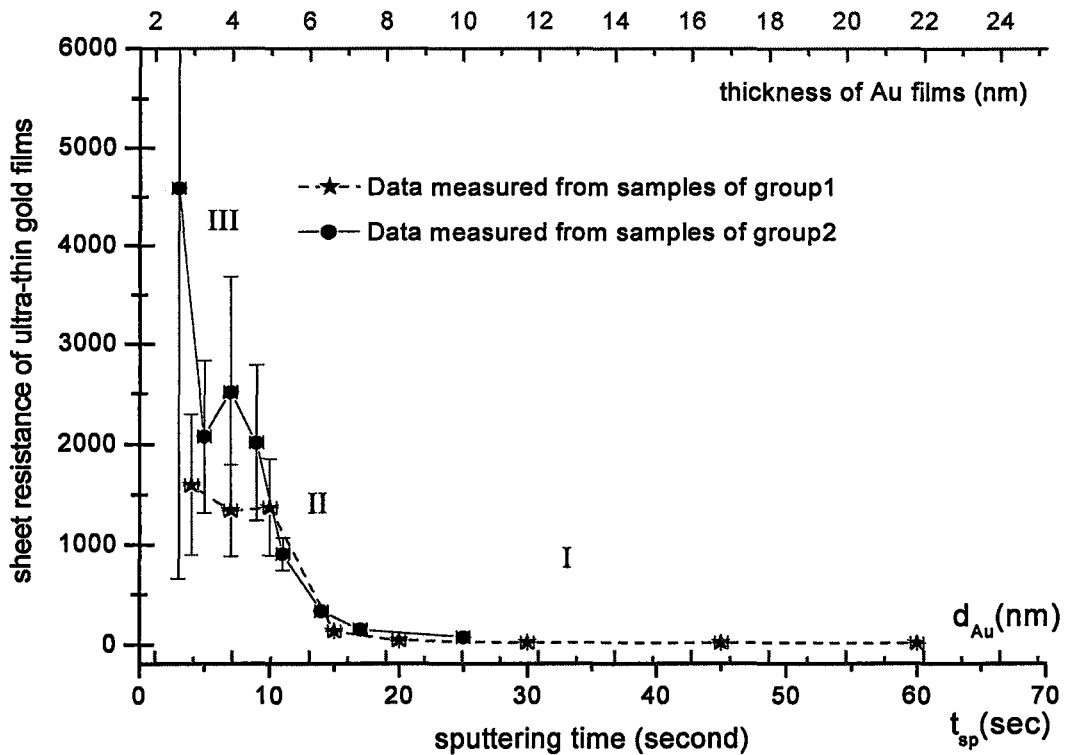


Figure 4.15 Sheet resistance of ultra-thin films with sputtering time ranging from 3 second to 60 second. Below tick labels of bottom axis are the sputtering time of ultra-thin gold films, and upper tick labels of bottom axis are the thickness of ultra-thin gold films related to the sputtering time. The scale is shown in the top axis.

For the sputtering time of more than 20 seconds, as well as the stage I region, sheet resistance of ultra-thin gold films are $34.2 \pm 1.2 \Omega/\square$ for 20 seconds, $14.3 \pm 0.4 \Omega/\square$ for 30 seconds and $7.2 \pm 0.2 \Omega/\square$ for 60 seconds. The sheet resistance of the ultra-thin gold film is inversely related to the sputtering time, as well as thickness, for the thickness of ultra-thin gold films is linear with the sputtering time as shown in figure 4.13. The sheet resistance of the ultra-thin gold film abides by the ohmic law and the formula of $R_{\square} = \rho/d_{Au}$

provided that the thickness of ultra-thin gold layer is more than $6.55\pm 0.33\text{nm}$ or sputtering time of 18 seconds. When the thickness of ultra-thin gold films is larger than $6.55\pm 0.33\text{nm}$, ultra-thin gold films are composed of long island chains as shown in figure 4.12(c), (d) and (e), which results in ultra-thin gold films having the electric properties of continuous films.

However, when the thickness of the ultra-thin gold film is less than $6.55\pm 0.33\text{nm}$, and sputtering time from 7 seconds to 15 seconds, the electrical conduction mechanism is the non-ohmic conduction shown in stage II due to the discontinuity of ultra-thin gold films. Ultra-thin gold films are composed of tiny isolated islands as shown in the AFM images of figure 4.12(a) and (b). Based on the model of the conductance by tunneling effects, and the calculation by superposition of electron wave functions between islands [4.5, 4.13, 4.14, 4.15], the conductance is a function of the temperature and distance between islands. Isolated islands diminish as the sputtering time decreases and as the thickness of ultra-thin gold films decreases; as the isolated islands diminish, the conductance exponentially decays from a carrier transfer mechanism of tunneling or thermionic emission related to the diminishing of isolated islands. Studies of ultra-thin gold films focused on non-ohmic conduction are reported only on gold films thicker than 5nm.

In stage III, a point of inflection was observed for the first time in measurement results of two group samples. It is interesting that the conduction behavior becomes better as the thickness of ultra-thin gold films decreases from stage II. However it is supposed to be worse as expected from the mode of tunneling effects and thermionic emission. It is

also difficult to explain this result based on the interface effects between the surface of ITO films and tiny gold islands (gold QDs). It might be assumed that electron wave functions are limited too weakly by isolated gold QDs as the size of gold QDs diminishes, and expand outside the space of isolated gold QDs much more. However, the space interval between isolated gold QDs does not enlarge as shown in figure 4.12(a) due to high density of isolated gold QDs distributed on the surface of ITO films. Therefore, the superposition of electron wave functions between isolated gold QDs in this case enhances and results in tunneling effects enhancement. The conductance of the ultra-thin gold layer becomes better and results in the anomalous effect of its sheet resistance when the thickness of it is around 3nm. As the thickness of the ultra-thin gold film decreases, the separation between gold QDs increases as the size of isolated gold QDs diminishes; then the superposition of electron wave functions between isolated gold QDs might be weakened. Its conductance becomes bad and its sheet resistance increases quickly again, as shown in figure 4.15.

4.2.3 Optical Features of Ultra-Thin Gold Films

The reflection spectra of ultra-thin gold films on Si substrates and glass slide substrates were measured by SUB 2000 Fiber Spectrum of Ocean Optics Inc. The measurement results are shown in figure 4.16 and figure 4.17. It can be seen from figure 4.16 and figure 4.17 that the reflection from the surfaces of the ultra-thin gold films increases with the increase of sputtering time of ultra-thin gold films, as well as the increase of the thickness of ultra-thin gold films. As the sputtering time increases, and as

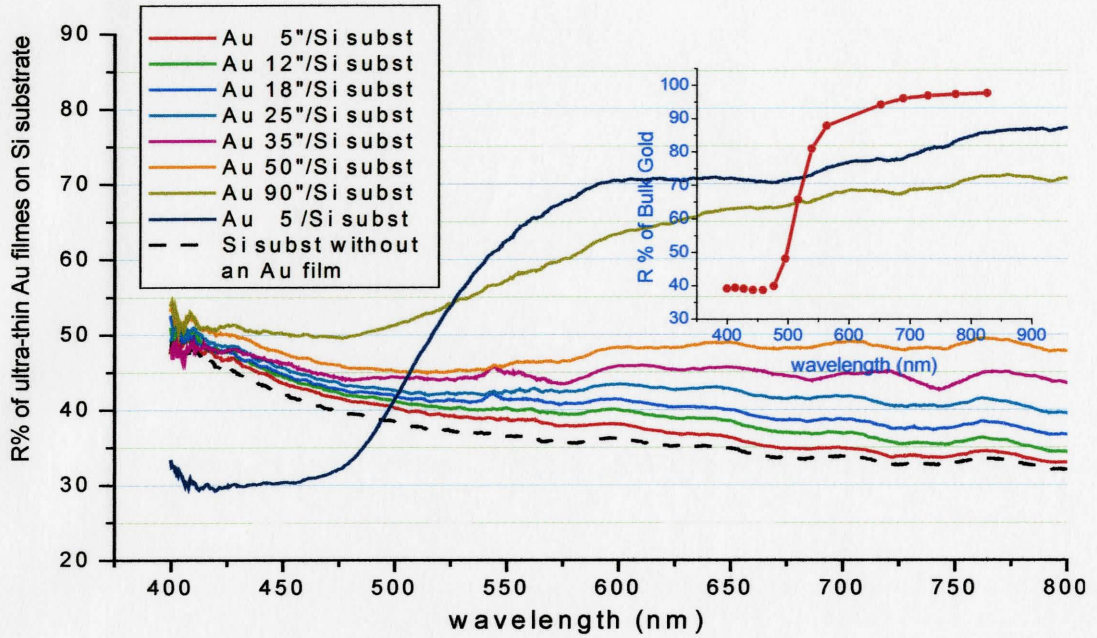


Figure 4.16 Reflection spectra of ultra-thin gold films on Si substrates with sputtered time ranging from 5 second (5") to 5 minutes (5'). In-site is reflection spectrum of bulk gold with polished surfaces.

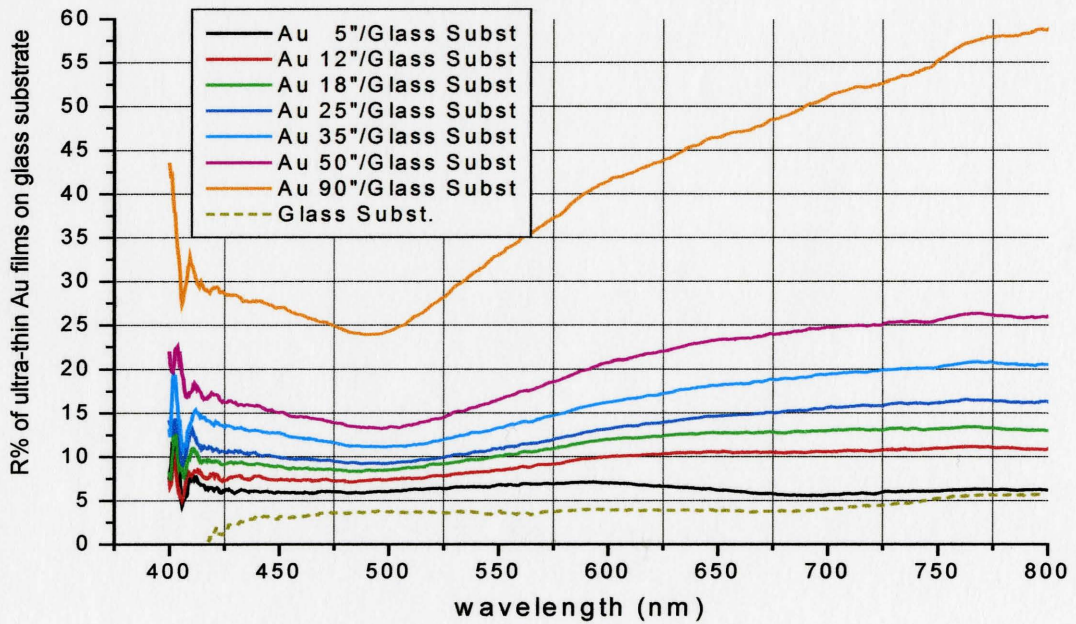


Figure 4.17 Reflection spectra of ultra-thin gold films on glass slide substrates with sputtered time ranging from 5 seconds to 5 minutes

the thickness of the ultra-thin gold films increases, the reflection at long wavelength range increases faster than that at short wavelength range. If the gold film is sputtered for 5 minutes as shown in figure 4.16, its reflection spectrum is similar to the reflection spectrum of bulk gold with a polished surface.

However, with a sputtering time of 5 seconds, the reflection spectrum of the ultra-thin gold film is similar to the reflection spectrum of the substrate whether the substrate is the Si substrate or the glass substrate, following the reflection spectrum of the substrate but increasing by several percent. Therefore, by changing the thickness of ultra-thin gold film, as well as its sputtering time, we can adjust the reflectance from its substrate. It provides a new way of looking for high refractive index materials in the design and fabrication of multi-layer AR coatings.

The transmittance spectra of ultra-thin gold films on the glass slide substrates are shown in figure 4.18, which were measured with a Cary 50 probe UV-visible spectrophotometer. To compare transmittance spectra of ultra-thin gold films on glass substrates in figure 4.16 with relevant reflection spectra in figure 4.17, it can be easily seen that the reflection is lower where the transmittance is higher, and higher where the transmittance is lower for ultra-thin gold films with sputtering time longer than 12 second. For a concave valley in the reflection spectrum, there is a convex peak in the transmittance spectrum located at the same wavelength region around 500nm.

It is noticed in the reflection spectrum of the ultra-thin gold film with sputtering time 5 seconds in figure 4.17 that its reflectance spectrum is convex at the wavelength region around 575nm, and its transmittance shows a dent at this region of around 575nm

in figure 4.18. This phenomenon happens for the ultra-thin gold film of (2.98 ± 0.15) nm with the sputtering time of 5 seconds. It is totally different from the reflection and transmittance spectral curves of ultra-thin gold films with the thickness thicker than (2.98 ± 0.15) nm. The sheet resistance of the ultra-thin gold film with the thickness around (2.98 ± 0.15) nm shows an electric resistance related to this thickness of the ultra-thin gold film in figure 4.15. The image in figure 4.12 (a) shows that the ultra-thin gold film with the thickness of approximately 3nm is composed of tiny gold particles with high density

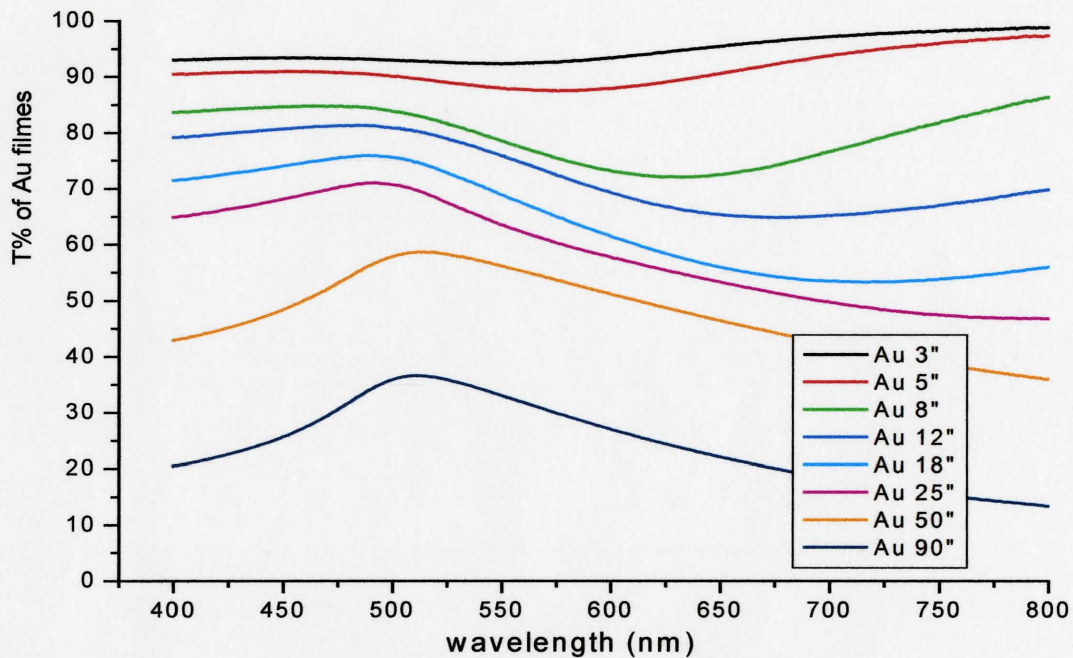


Figure 4.18 Transmittance spectra of ultra-thin gold films on glass slide substrates with sputtering time ranging from 5 seconds to 5 minutes

Finally, it can be seen that the transmittance of ultra-thin gold films in the visible region is higher than 70% while the sputtering time is less than 8 seconds.

Chapter 5 Experimental (II) and Discussion

(AR coating and contrast of SSTFEL devices)

This chapter presents the measurement results of specular and diffuse reflections of the AR coatings on the polypropylene sheets and SSTFEL devices. Also, the contrast ratio of SSTFEL devices with AR coatings is discussed.

5.1 AR Coatings on Polypropylene Sheets

Polypropylene sheets with thickness of 0.9mil used in the study were purchased from Copol International Ltd. A 30nm thick gold layer was deposited on one side of the polypropylene sheet by magnetron sputtering for 2 minutes. After the two annealing processes as well as two embedding processes described in Chapter 3, the ITO film of 100nm was deposited on the top of samples to simulate the part A area of the surface of SSTFEL devices shown in figure 2.7 (a). Figure 5.1 shows the specular reflectance spectra of two samples. They were measured by USB2000 Fiber Optic Spectrometer.

Reflectance, shown as a red curve, is over 18% in the whole visible wavelength, and over 25% in green and red region, which results from high reflectance of the 30nm gold layer on the polypropylene sheets. The black curve is the specular reflection spectrum of a sample without an ITO layer. It is like the reflection spectrum of bulk gold with a polished surface shown in the in-site of figure 5.1.

After two layers of AR coatings were sputtered on the top of polypropylene sheets with the 30nm thick gold layer, the reflectance of samples drops down quickly. These

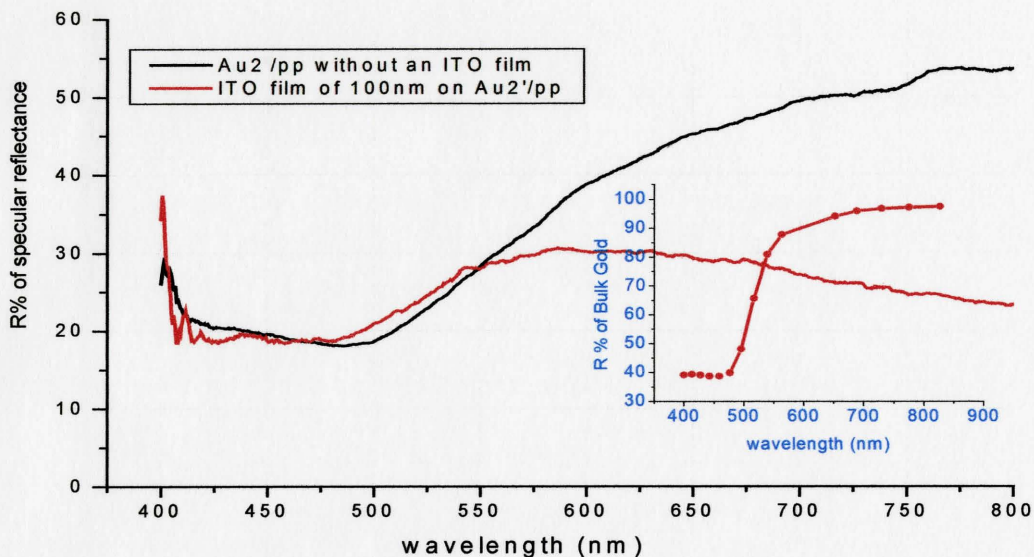


Figure 5.1 Specular reflectance spectra of samples with a ITO film of 100nm on Au₂'/pp and without a ITO film on Au₂'/pp. The in-site is the reflectance of bulk gold with a polished surface [5.1]

measured specular reflectance spectra of samples are shown in Figure 5.2 from page 70 to 73, which are organized in groups based on the sputtering time of ITO layers. Comparing the red spectral curve in figure 5.1 with other spectral curves in figure 5.3(d), it can be seen that the specular reflection of samples with AR coatings obviously drops down in the whole visible wavelength range when the proper thickness of AR coating layers was selected. Compared with those in figure 5.2 respectively, it can be found easily that minimum reflectance moves from shorter wavelength to longer wavelength as the sputtering time of ITO films increases, as well as thickness of ITO films increases. Because the increase of ITO thickness results in optical path light passing in the ITO layer elongating, destructive interference happens in the longer wavelength for thicker ITO films.

At the long wavelength region in figure 5.2(a) and (g), it also can be found that

the ultra-thin gold layer in AR coatings is an adjusting layer of lightwave amplitudes to match amplitude of both reflection beam $R1$ and $R2$ shown in figure 2.7(a), to allow maximum destructive interference between $R1$ and $R2$. $R1$ and $R2$ are, respectively, the light beams reflected from the surface of the ultra-thin gold layer and the interface between the ITO layer and the bottom thicker gold layer on polypropylene sheets.

At the long wavelength region, when the ultra-thin gold layer is thinner as sputtering time is as short as 4 seconds, $R1$ is weaker and most of the incident light passes through it with high transmittance. Although incident light was absorbed by the ITO layer and the ultra-thin gold layer, loss is less in the case of the ultra-thin gold layer. $R2$ is strong due to the high reflection from the bottom thick gold layer as a black curve shows in figure 5.1. Therefore, two beams cannot cancel even if they are completely out of phase, which results from the difference between $R1$ and $R2$. Thus the reflection is still strong in this longer wavelength region, and it can be seen in every group of figure 5.2.

As the thickness of the ultra-thin gold layer increases, $R2$ decreases and $R1$ increases. The difference between them surges between large and small from figure 5.2(f). The reflectance spectrum of samples is high at sputtering of 4 seconds; drops at 7 seconds, and reaches the minimum at 9 and 11 seconds. Then reflectance rises further while sputtering time increases from 27 to 46 seconds.

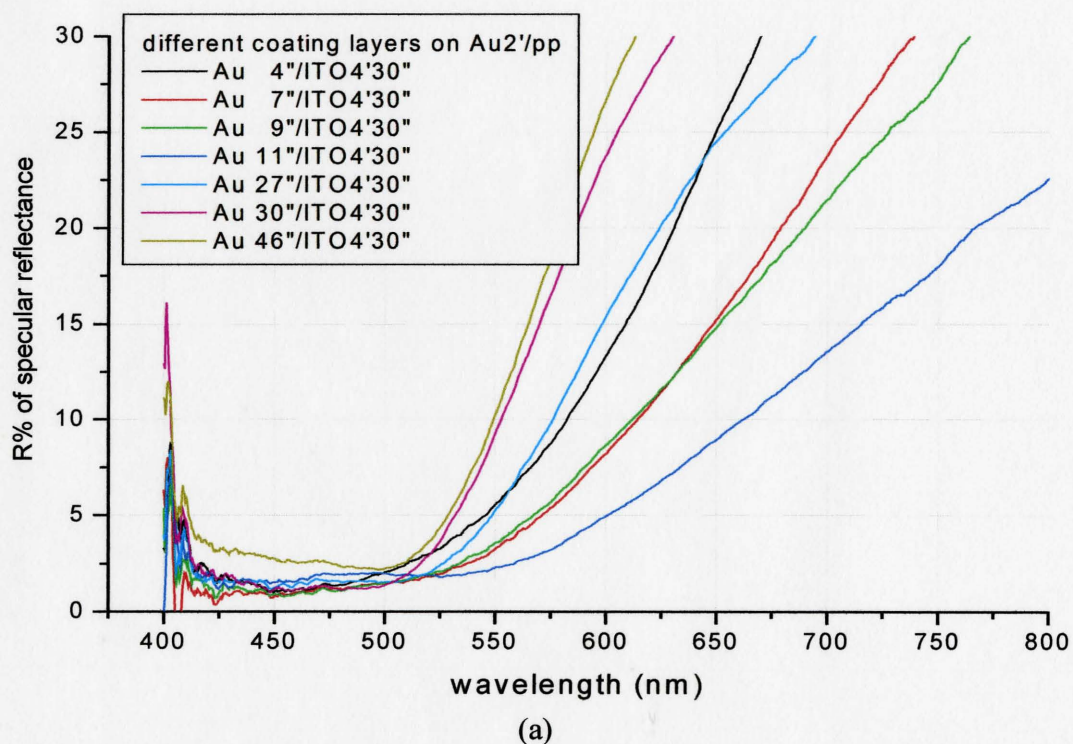
In the short wavelength region, this phenomenon also can be observed in figure 5.2(b). The reflectance spectra of samples are high for sputtering times of 4 and 7 seconds; drop at 9 seconds, and reach to minimum at 11 and 27 seconds. Then reflectance rises while sputtering time increases from 30 to 46 seconds.

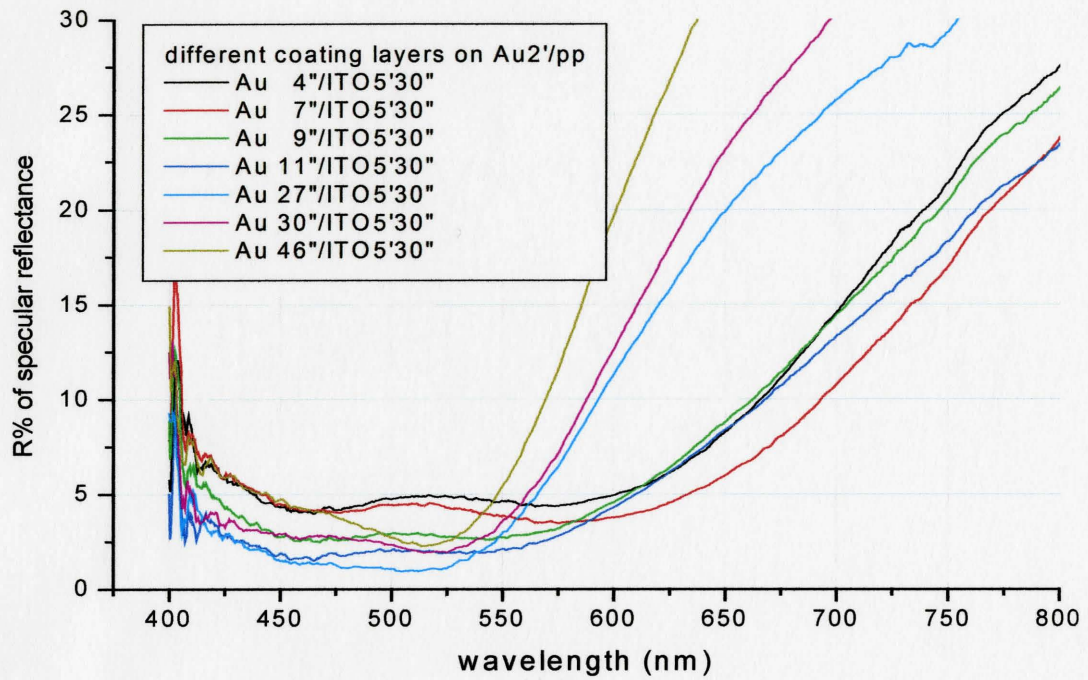
Compared with all reflection spectra in figure 5.2, it can be found that AR coatings have better performance when they are composed of ultra-thin gold layers with sputtering time ranging from 7 to 11 seconds and ITO layers ranging from 5'30" to 6'30". Related thickness of ultra-thin gold layer ranges from (3.44 ± 0.27) nm to (4.59 ± 0.29) nm, and thickness of ITO layer ranges from (395 ± 28) Å to (455 ± 30) Å. These reflectance spectra are present in figure 5.3 from page 74 to 75 based on the sputtering time of ultra-thin gold layers. Finally, the spectrum curves with low reflectance in figure 5.3 were selected and shown in figure 5.4 in page 76. Areas included by these selected spectra in the visible wavelength from 410nm to 700nm were calculated by the integrate function in the Calculus item of Origin Software and results are present in the Table 5.1. The wavelength region from 400nm to 410nm was discarded in the calculation due to the measurement noise.

Table 5.1 Integration areas of specular reflection spectra ranging from 410 to 700nm for lower spectra of samples in figure 5.4

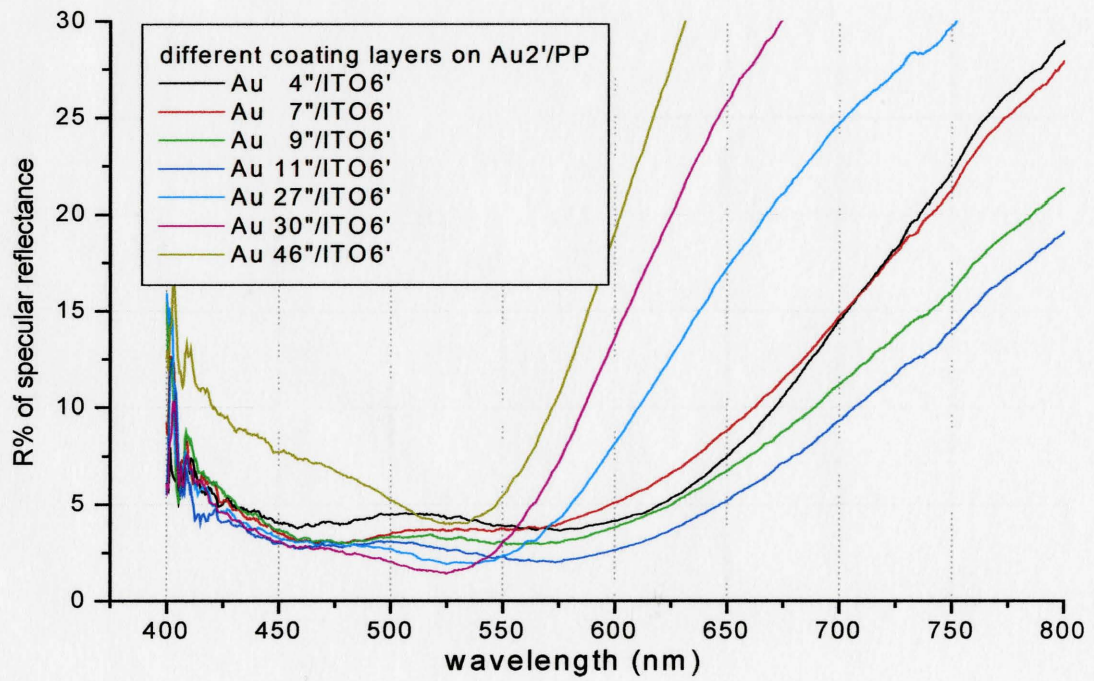
Sample number	sputtering time of related AR coating layers	Integration areas(nm)
2-7	Au 7"/ ITO 5'30"	1466.87
7-7	Au 7"/ ITO 6'	1647.81
3-7	Au 7"/ ITO 6'30"	1431.54
7-2	Au 9"/ ITO 6'	1375.19
3-2	Au 9"/ ITO 6'30"	1568.10
4-2	Au 9"/ ITO 7'30"	1535.91
3-1	Au 11"/ ITO 6'30"	1308.69

While the AR coating with constituent layers of Au 11"/ ITO 6'30" has lowest integration areas, the AR coating has best performance in reducing the specular reflectance and with high transmittance while its constituent layers are Au 7"/ ITO 6'30" and Au 9"/ ITO 6', as well as the thickness of Au (3.44 ± 0.27) nm/ITO (455 ± 29) Å and (4.01 ± 0.29) nm/ITO (425 ± 29) Å. Their specular reflectances in visible wavelength range are 4.9% and 4.7% respectively

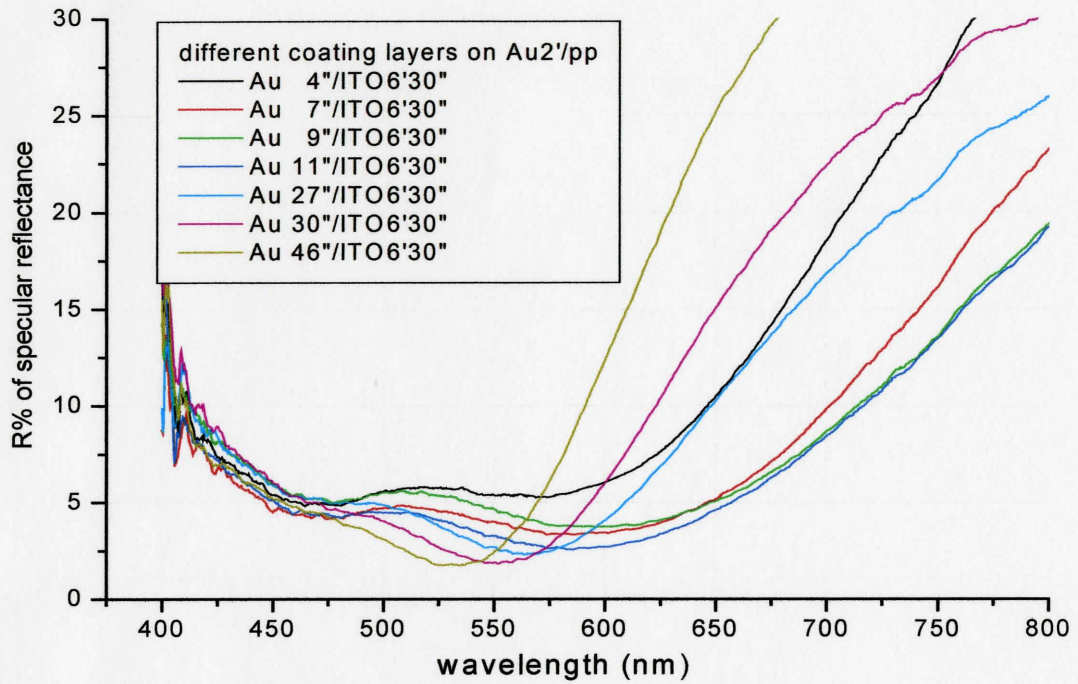




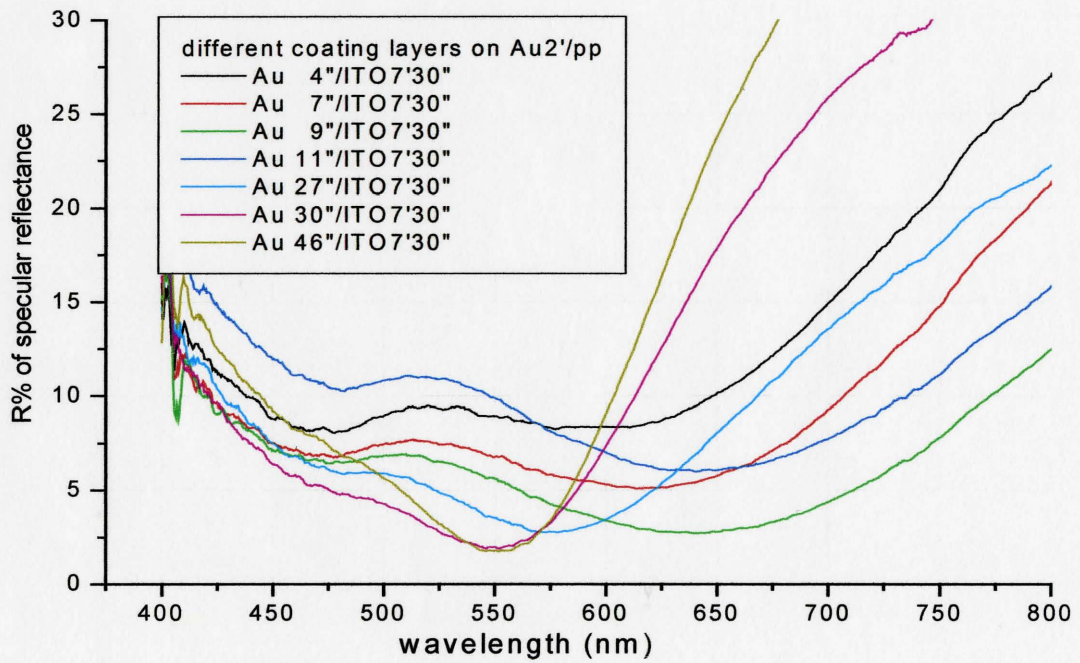
(b)



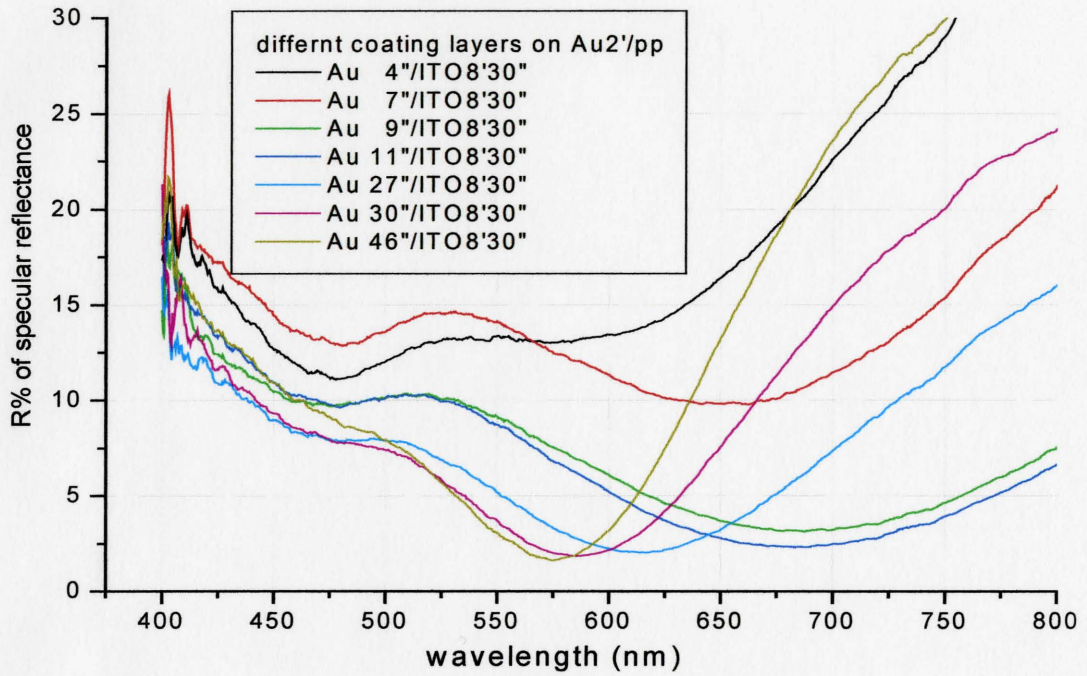
(c)



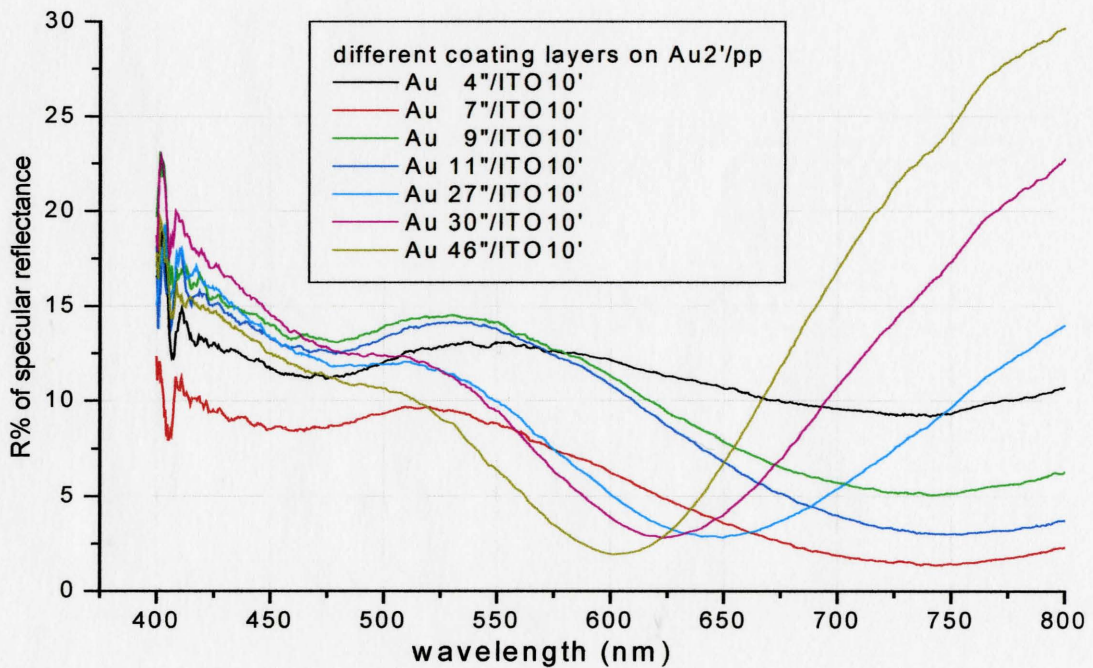
(d)



(e)

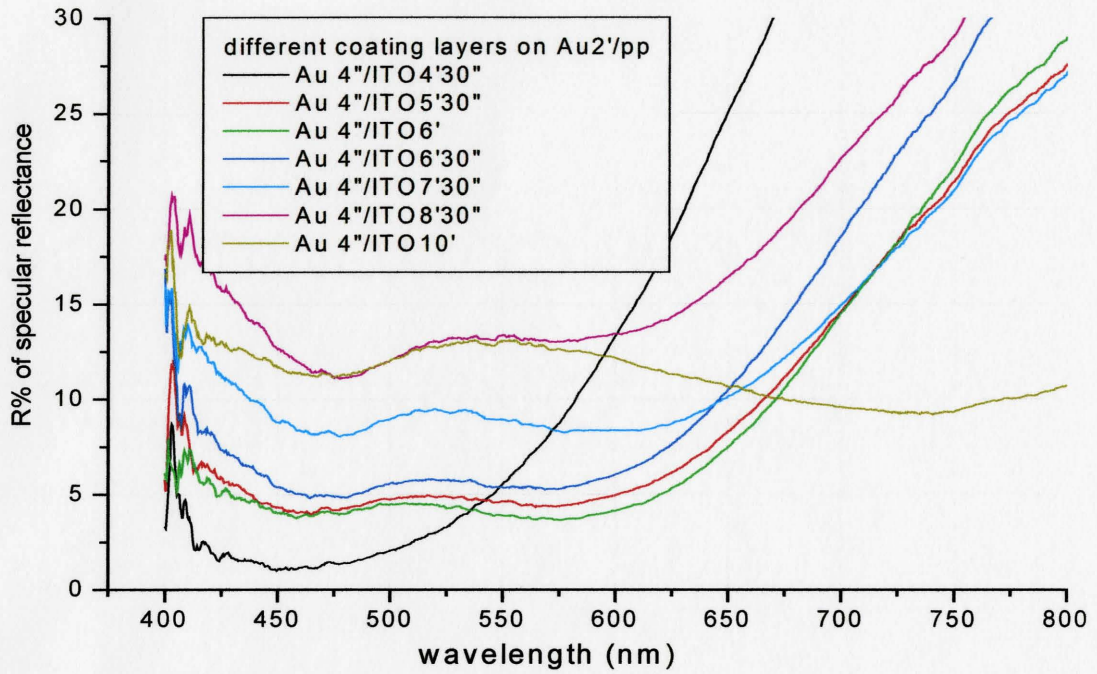


(f)

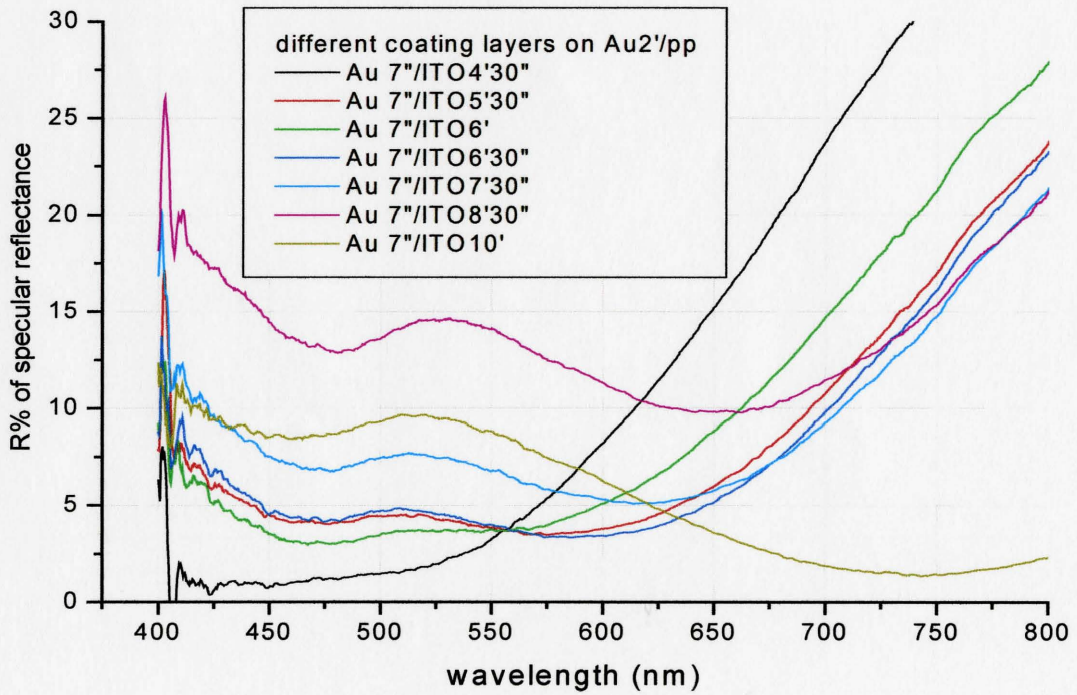


(g)

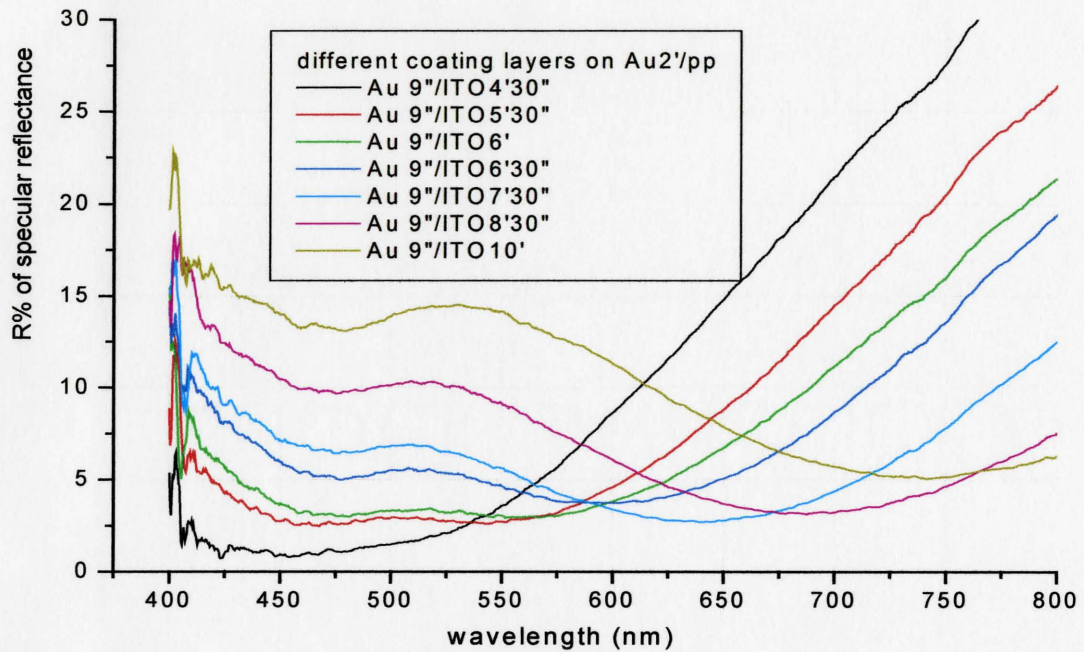
Figure 5.2 Specular reflectance spectra of samples with different thickness of AR coating layers on Au2'/pp, organized based on the sputtering time of ITO layers



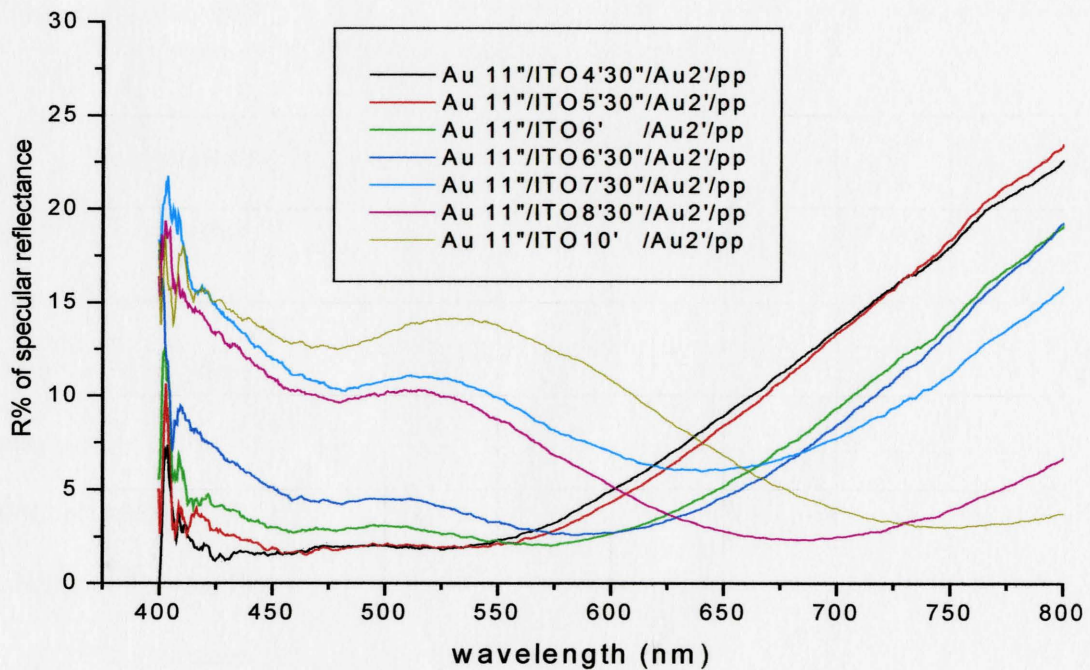
(a)



(b)



(c)



(d)

Figure 5.3 Specular reflectance spectra of samples with different thickness of AR coating layers on Au2'/pp, organized based on the sputtering time of ultra-thin gold layers

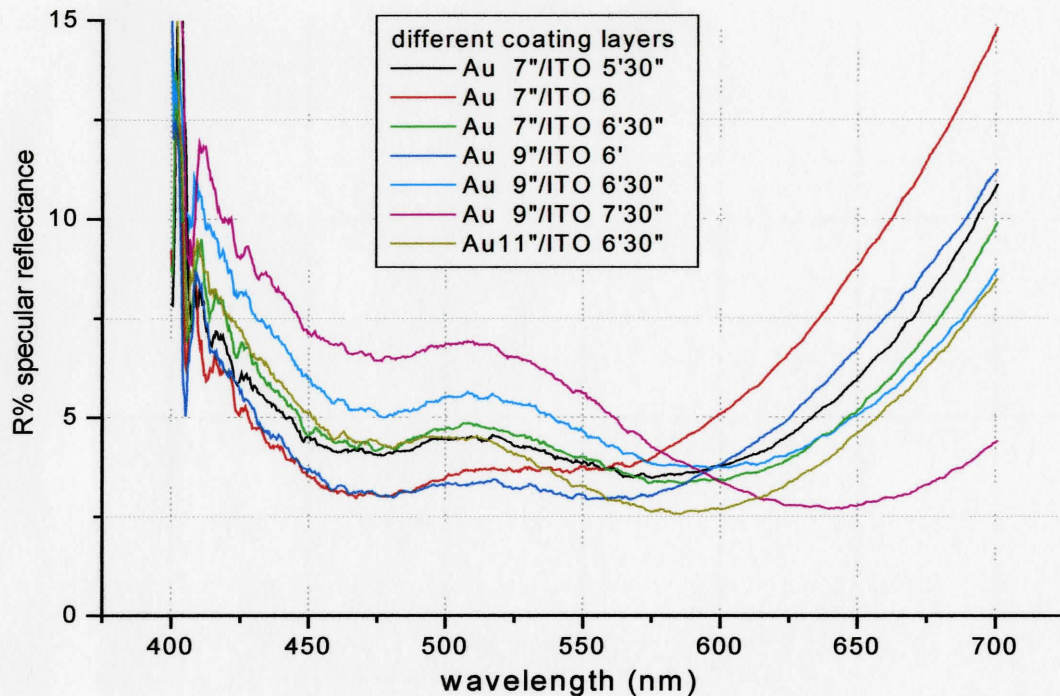


Figure 5.4 Lower reflectance spectra of samples in figure 5.3 with different thickness of AR coating layers on Au₂'/pp.

After annealing at 200°C for several seconds, the smooth surface of the polypropylene sheet became wavelike. Its surface morphology was shown in figure 4.14(f). Therefore, there is a small part of diffuse reflection from the surface of samples under ambient incident light. Diffuse reflection spectra of these samples were also measured in an office by USB 2000 Fiber Spectrometer under ambient light of about 300Lux. Ambient illumination of the office was measured by Luminance Meter LS-100 of Minolta Camera Co. Ltd.

The measurement results are shown in figures 5.5 from page 79 to 82, which are organized in a group based on the sputtering time of ITO layers, too. To compare among these spectra as it was done in the case of specular reflection spectra, some spectra of

samples with better performance are organized in figure 5.6 from page 82 to 84 based on the sputtering time of ultra-thin gold layers. When the sputtering time of the ultra-thin gold layer is from 7 to 11 seconds and the sputtering time of the ITO layer is from 5'30" to 6'30", the AR coatings exhibit better performance of decreasing the diffuse reflection than other AR coatings with different sputtering times of constituent layer. Spectra with lower reflectance in figure 5.6 are selected and displayed in figure 5.7 at page 84.

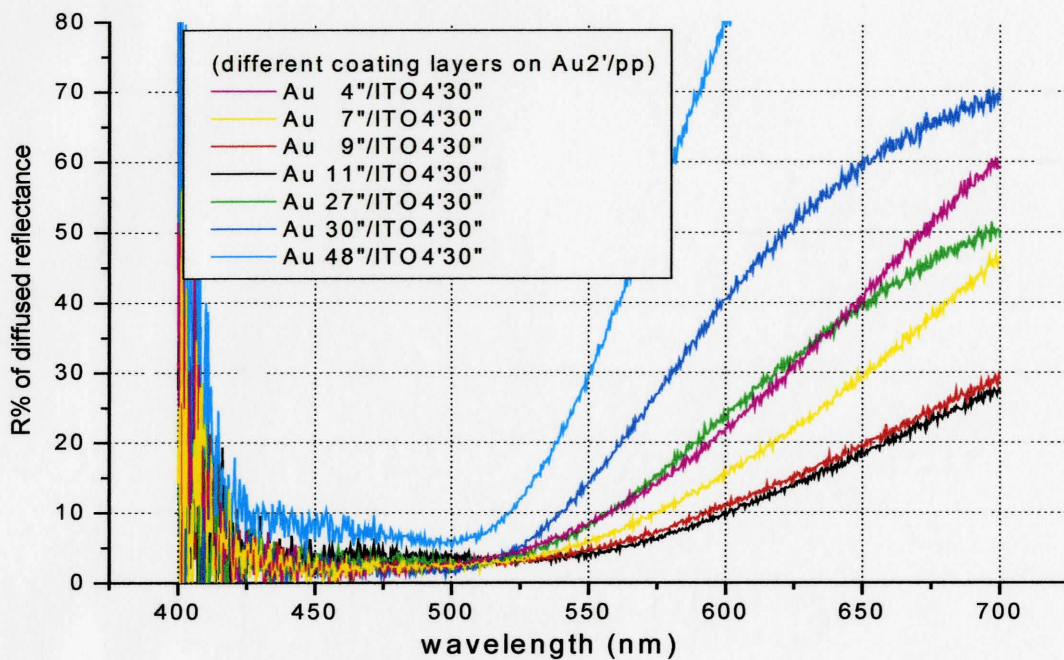
Finally the lower spectra in figure 5.7 were smoothed by the adjacent averaging, a function in the Origin software. Then areas included by these selected spectra in the visible wavelength range from 425nm to 700nm were calculated and results shown in Table 5.2. The wavelength region from 400nm to 425nm was neglected in the calculation due to the measurement noise.

Table 5.2 shows that AR coatings with the ultra-thin layer formed by 11 seconds of sputtering time not only have lower integration areas than others when the sputtering time of the ultra-thin layer is 7 and 9 seconds, but also have the lowest integration area among them, which is 1821.73 (nm) with constituent layers of Au 11"/ ITO 6'. However, considering the high transmittance of AR coatings needed, Au 7"/ ITO 6', Au 7"/ ITO 6'30", Au 9"/ ITO 5'30" and Au 9"/ ITO 6', as well as Au (3.44nm)/ITO (425Å), Au (3.44nm)/ITO (455Å), Au (4.01nm)/ITO (395Å), Au (4.01nm)/ITO (425Å) are also good constituent layers for AR coatings to have good performance. The average reflectance of these samples in the visible wavelength range is around 8 to 12%.

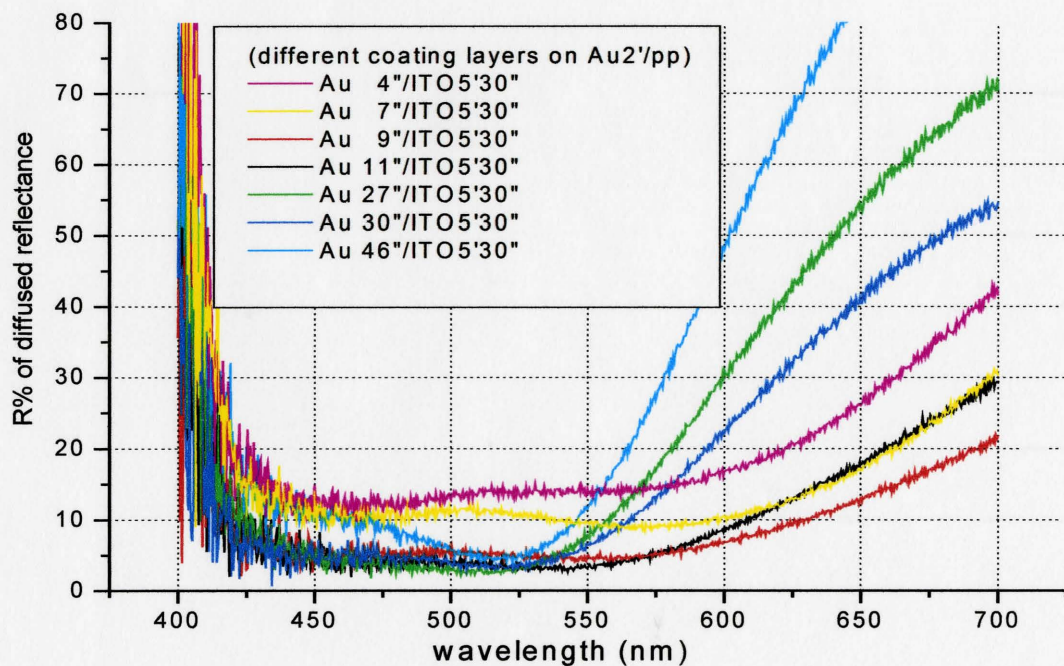
Table 5.2 Integration areas of diffuse reflection spectra ranging from 425 to 700nm for lower spectra of samples in figure 5.7.

Sample number	Sputtering time of related AR coating layers	Integration areas(nm)
2-7	Au 7"/ ITO 5'30"	3672.57
7-7	Au 7"/ ITO 6'	2930.66
3-7	Au 7"/ ITO 6'30"	3196.23
2-2	Au 9"/ ITO 5'30"	2241.42
7-2	Au 9"/ ITO 6'	3292.15
3-2	Au 9"/ ITO 6'30"	3326.92
2-1	Au 11"/ ITO 5'30"	2647.70
7-1	Au 11"/ ITO 6'	1821.73
3-1	Au 11"/ ITO 6'30"	2231.59

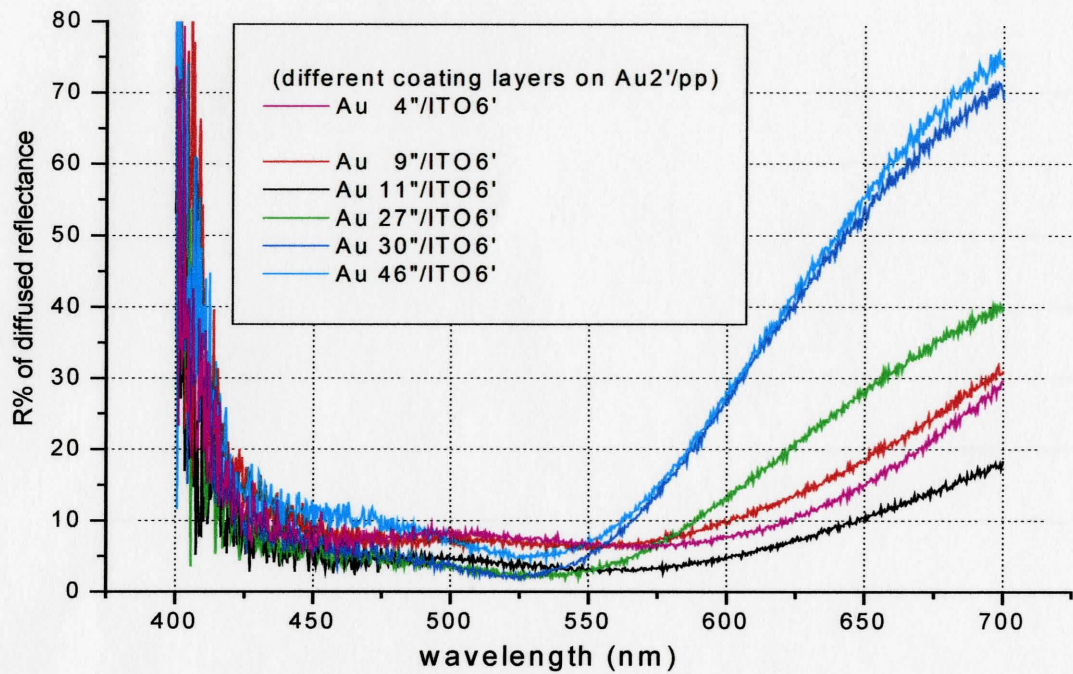
In summary, considering high transmittance of AR coatings to be necessary and low specular reflections and low diffuse reflections as needed, AR coatings have better performance on polypropylene sheets when the sputtering time of ultra-thin gold layers ranges from 7 to 9 seconds and sputtering time of ITO layers ranges from 6' to 6'30", as well as the thickness of ultra-thin gold layers ranges from (3.44 ± 0.28) nm to (4.01 ± 0.29) nm and thickness of ITO layers range from (425 ± 29) Å to (455 ± 30) Å. The average reflectance of specular and diffuse reflection in the visible wavelength range are about 5% and 12% respectively for AR coatings on the polypropylene sheets.



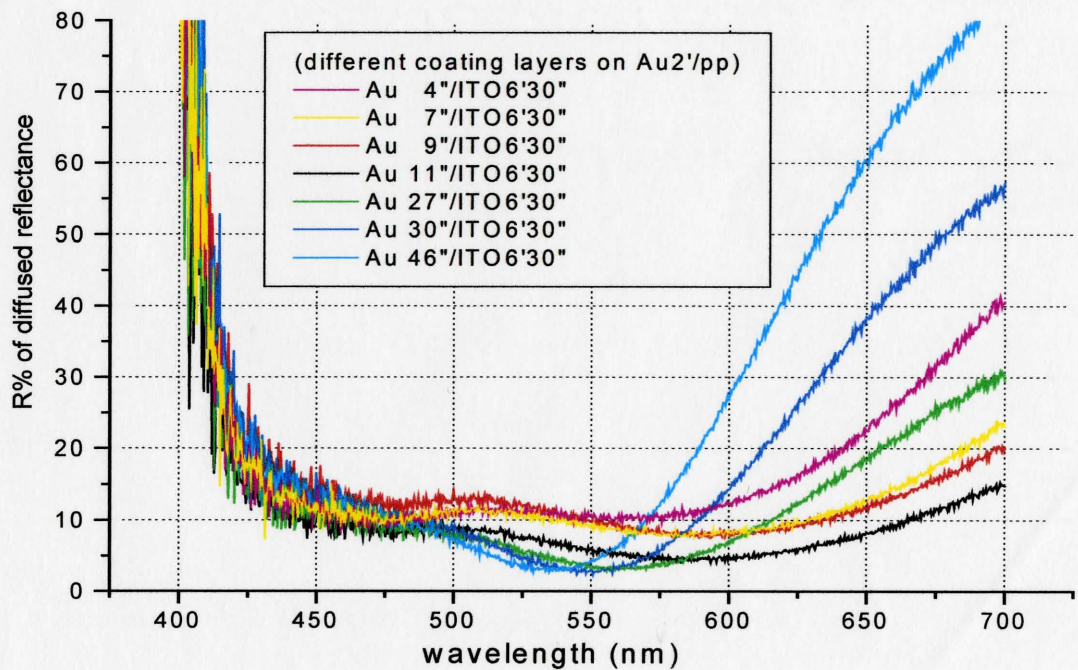
(a)



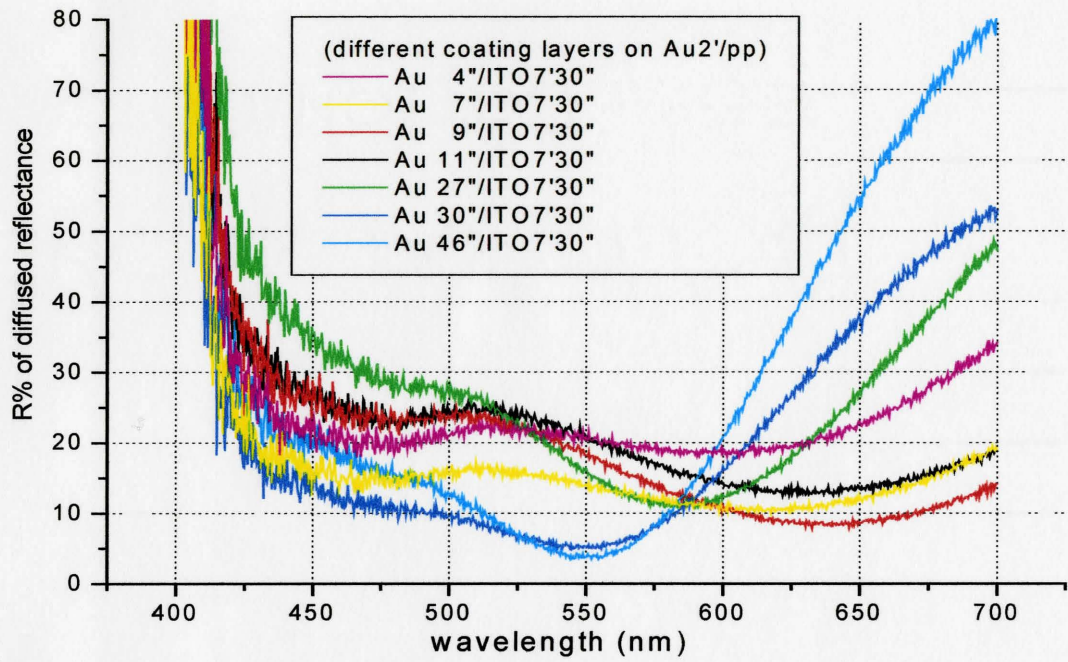
(b)



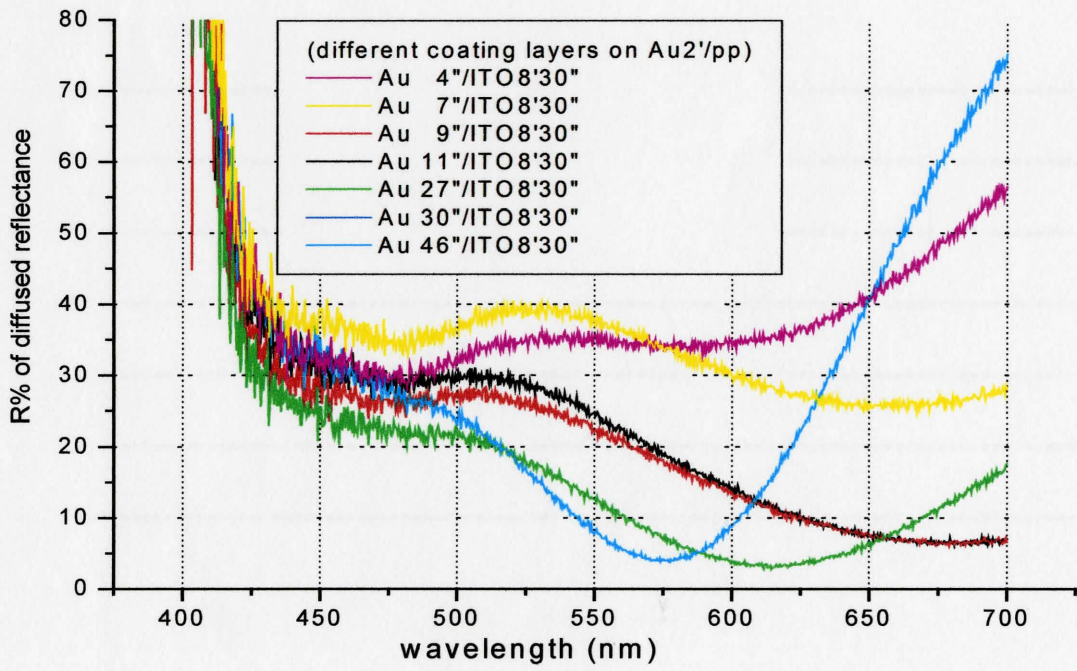
(c)



(d)



(e)



(f)

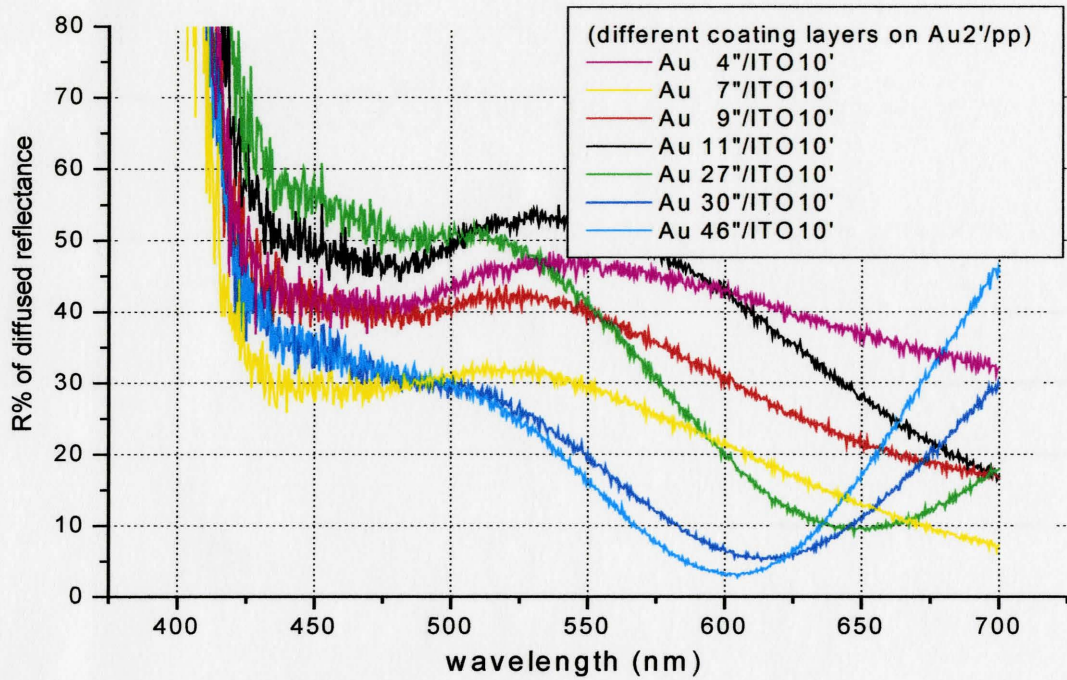
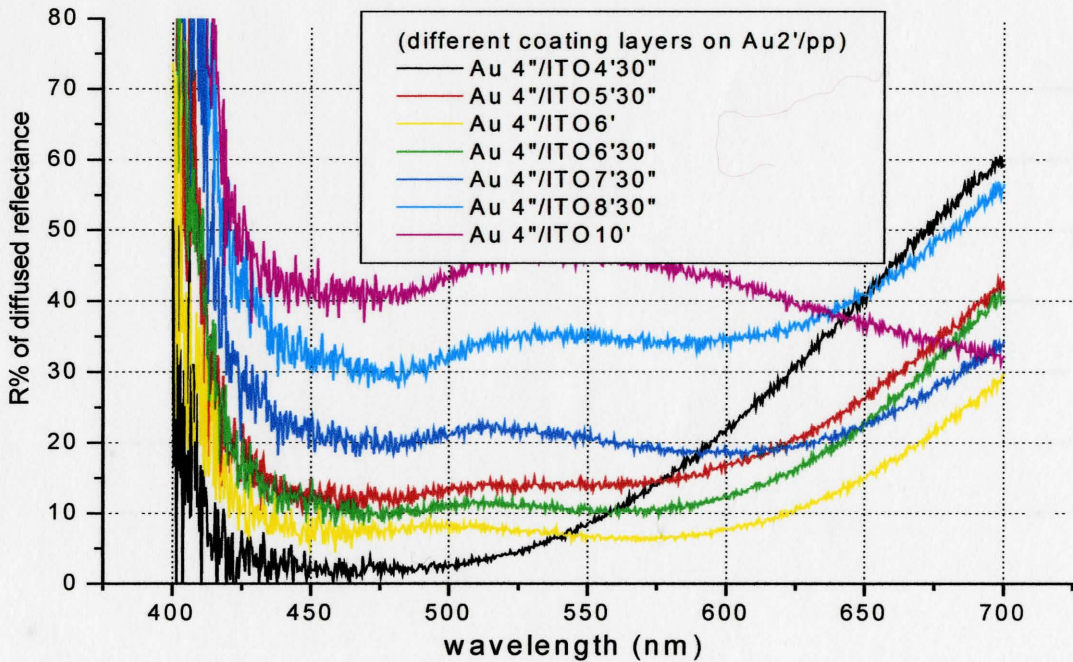
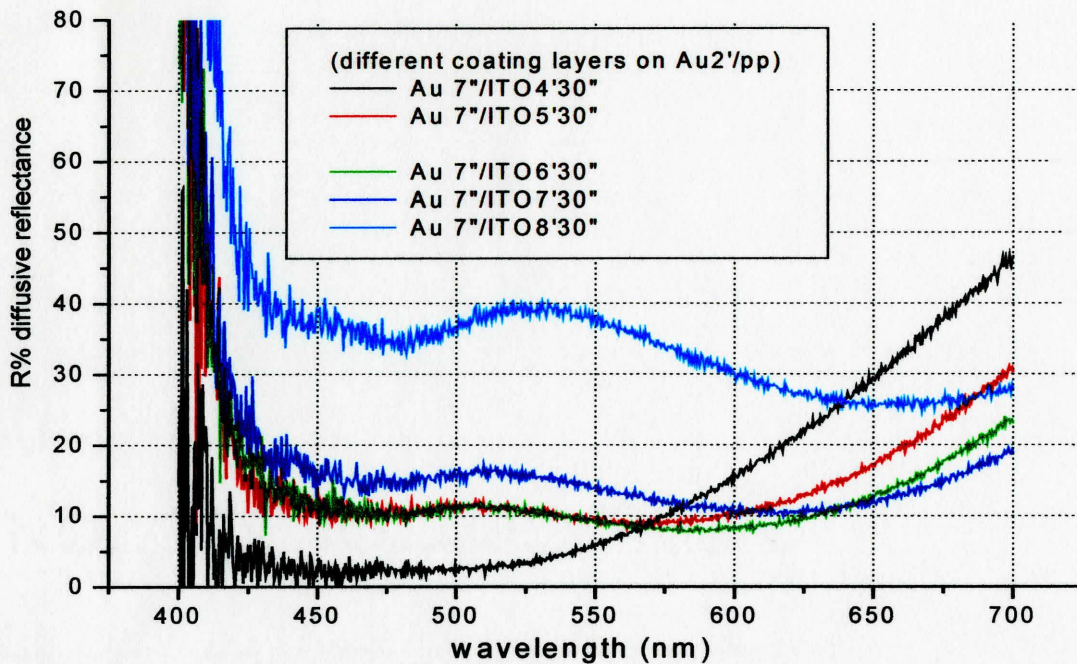
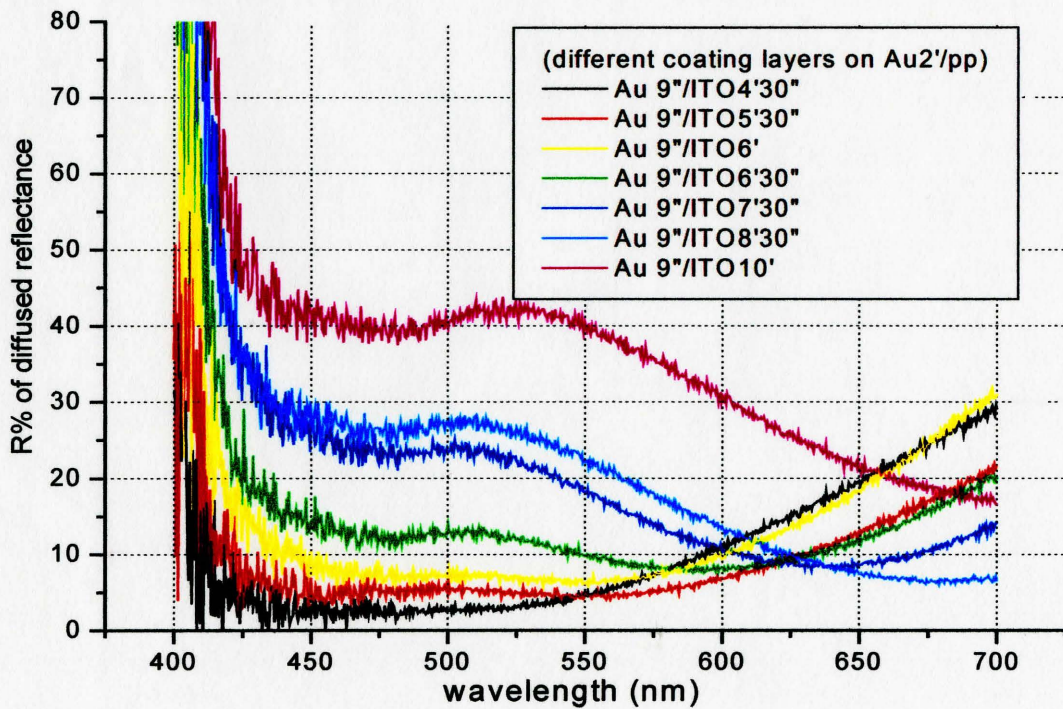


Figure 5.5 Diffuse reflectance spectra of samples with different thickness of AR coating layers on Au2'/pp, organized based on the sputtering time of ITO layers.





(b)



(c)

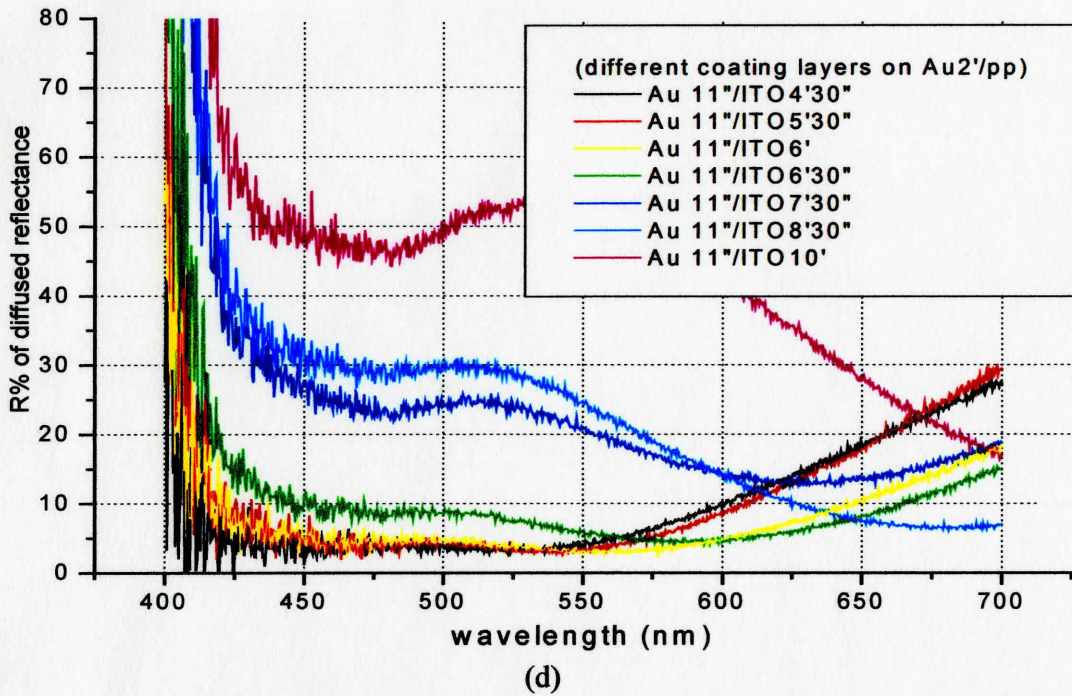


Figure 5.6 Diffuse reflectance spectra of samples with different thickness of AR coating layers on Au2'/pp, organized based on the sputtering time of ultra-thin gold layers.

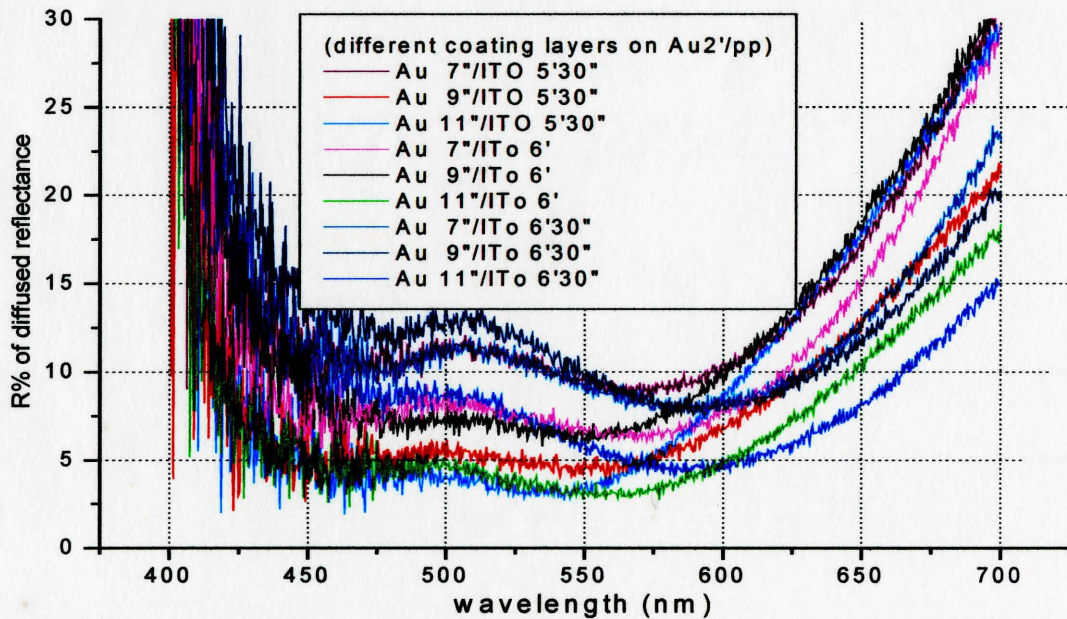


Figure 5.7 Lower reflectance spectra of samples in figure 5.6 with different thickness of AR coating layers on Au2'/pp.

5.2 AR Coatings on SSTFEL Devices

After the AR coatings were applied on the surface of SSTFEL devices, the specular and diffuse reflectance of the devices are 3 or 5 times lower than that of devices without AR coatings. Figures 5.8 and 5.9 show these measurement results. The diffuse reflection is always larger than the specular reflection because the surface of devices is highly packed with spheres with diameter of 50 μ m. Integration areas of specular reflection spectra ranging from 410 to 700nm in figure 5.8 for SSTFEL devices with or without AR coating are displayed in Table 5.3, which were calculated in the same way used in Chapter 5.1. Integration areas of diffuse reflection spectra ranging from 425 to 700nm in figure 5.9 for the same SSTFEL devices with or without AR coating are shown in Table 5.4.

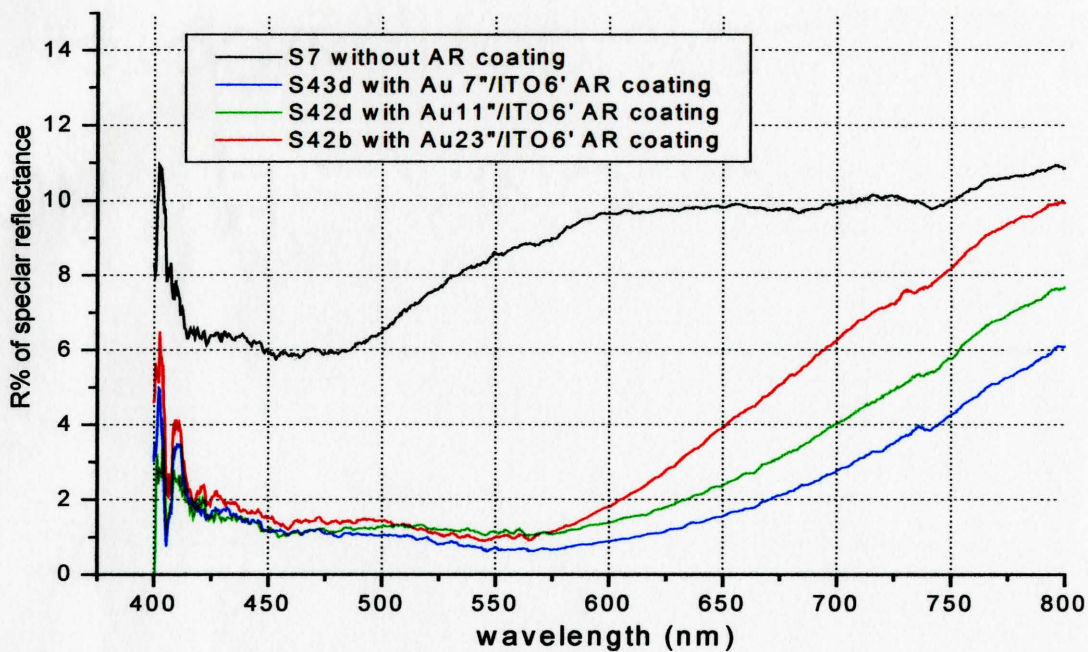
Table 5.3 Integration areas of specular reflection spectra ranging from 410 to 700nm in figure 5.8 for SSTFEL devices with different AR coating layers

Sample number	Sputtering time of related AR coating layers	Integrated areas(nm)
S42c	Au 7"/ ITO 5'40"	572.23
S43d	Au 7"/ ITO 6'	371.11
S43c	Au 11"/ ITO 5'40"	551.15
S42d	Au 11"/ ITO 6'	493.73
S42d	Au 23"/ ITO 5'40"	664.36
S42b	Au 23"/ ITO 6'	668.98
S2	Without AR coating	2374.29

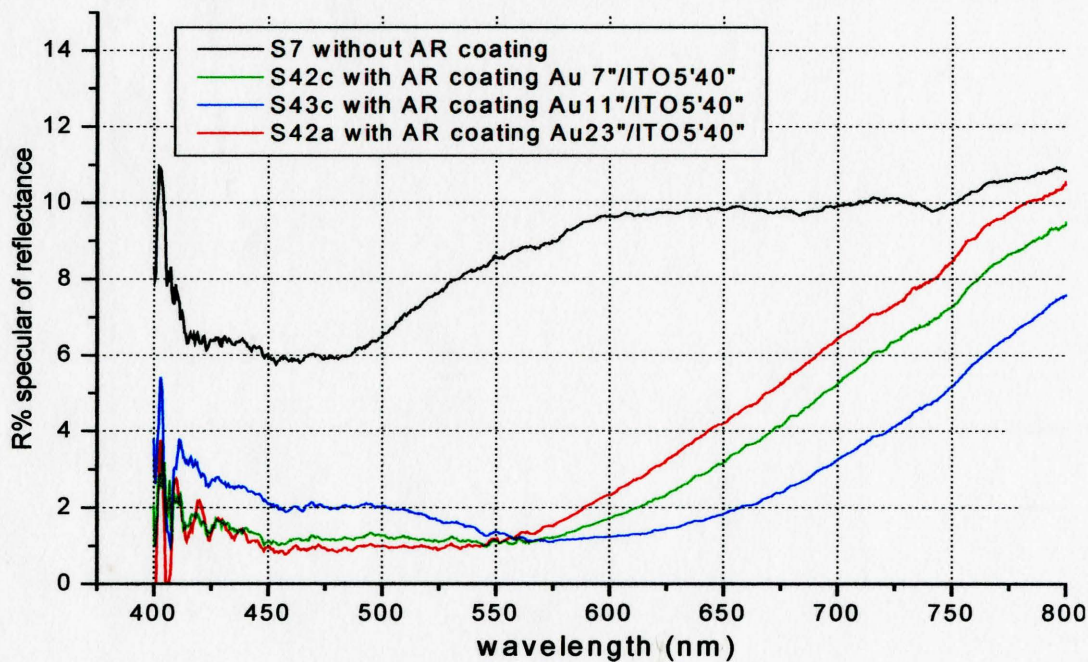
Table 5.4 Integration areas of diffuse reflection spectra ranging from 425 to 700nm in figure 5.9 for SSTFEL devices with different AR coating layers

Sample number	sputtering time of related AR coating layers	Integrated areas(nm)
S42c	Au 7"/ ITO 5'40"	7020.42
S43d	Au 7"/ ITO 6'	3750.31
S43c	Au 11"/ ITO 5'40"	4343.69
S42d	Au 11"/ ITO 6'	2884.59
S42d	Au 23"/ ITO 5'40"	5406.81
S42b	Au 23"/ ITO 6'	5342.39
S11	Without AR coating	23363.14

Comparing the data in Tables 5.3 and 5.4 and considering the high transmittance of AR coatings to be necessary, AR coatings have better performance to reduce specular and diffuse reflection of SSTFEL devices while the sputtering time of the ultra-thin gold layer is 7 seconds, and 6minutes for the ITO layer, as well as the thickness of (3.44 ± 0.28) nm and $(425 \pm 30) \text{Å}$ respectively. The average reflectance of specular and diffuse reflections in visible wavelengths is 1.3% and 13.6% respectively.

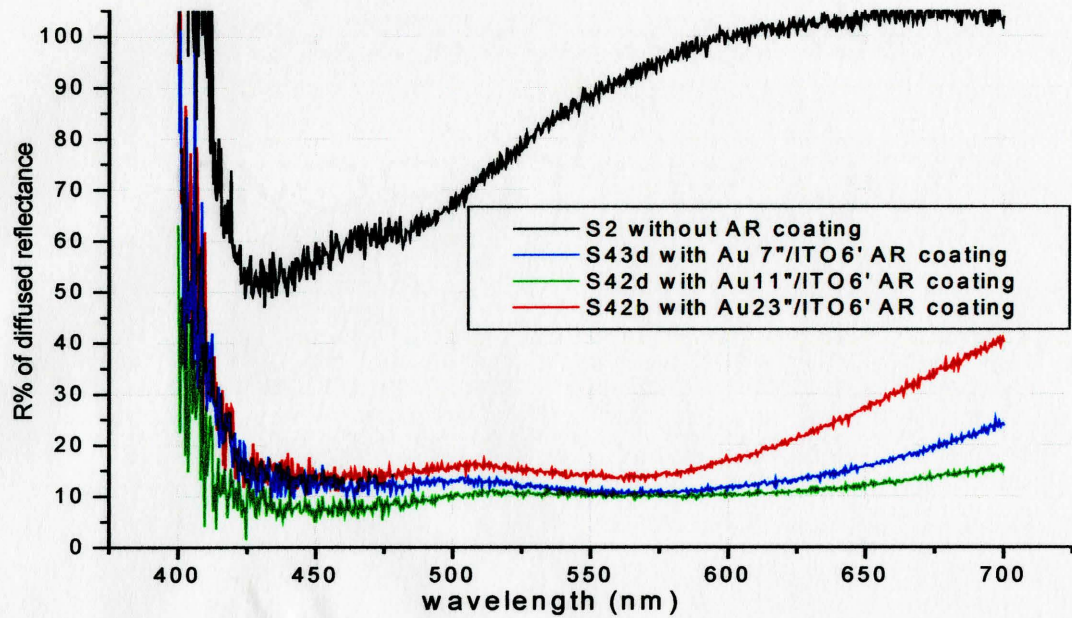


(a)

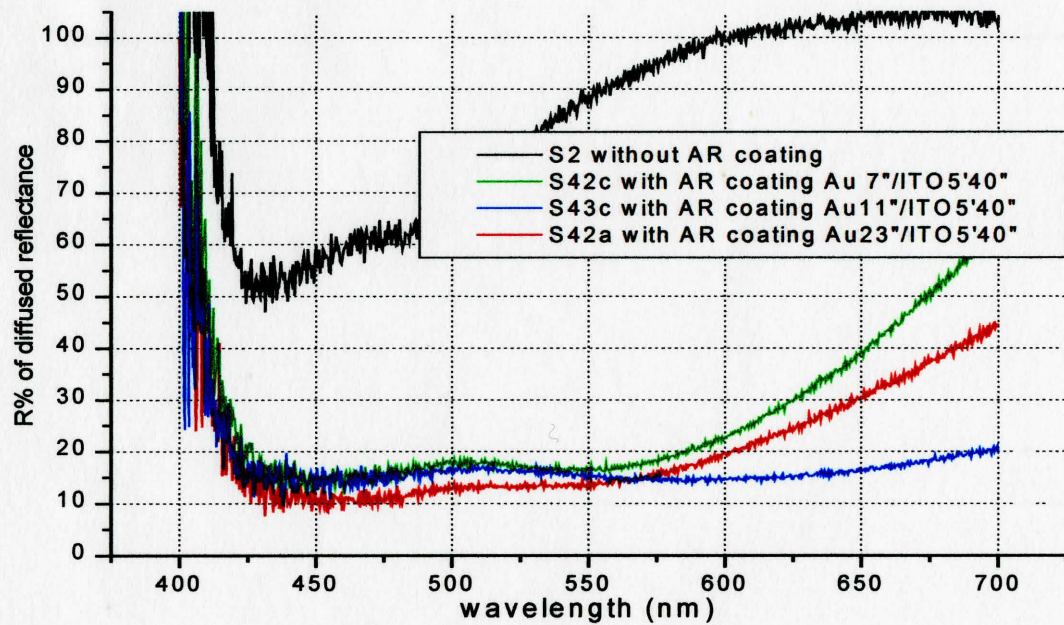


(b)

Figure 5.8 Specular reflectance spectra of SSTFEL devices with or without AR coatings.



(a)



(b)

Figure 5.9 Diffuse reflectance spectra of SSTFEL devices with or without AR coatings.

5.3 Contrast of SSTFEL Devices with AR Coatings

The contrast ratio of SSTFEL devices with or without the AR coatings was measured and compared in the different illumination conditions by a method of Full On/Off, a widely used measurement method in the video display industry. According to the Full On/Off method, the ratio of the light output white image (full on) and light output of an all black (full off) is expressed as the same expression (2.30) as

$$\text{contrast ratio} = \frac{L_{\text{pixel-on}}}{L_{\text{pixel-off}}} = \frac{L_{\text{El-on}} + L_{\text{reflect}}}{L_{\text{EL-off}} + L_{\text{reflect}}} \quad (5.1)$$

While the SSTFEL device was applied from a pulse voltage with the zero-to-peak of 250(V) and frequency of 745Hz, $L_{\text{pixel-on}}$ and $L_{\text{pixel-off}}$ were measured as “Pixel ON/OFF” by Luminance Meter LS-100 of Minolta Camera Co. Ltd. under different illumination conditions. Measurement results are presented in the Table 5.5.

The measurement results of SSTFEL devices with or without AR coatings under different ambient illumination conditions are presented in Table 5.5. The contrast ratio of SSTFEL devices with AR coatings is $(15.4 \pm 0.9):1$ at the ambient illumination level of (200.0 ± 7.2) lux, and increases up to $(47.9 \pm 2.0):1$ as the ambient illumination level decreases to (52.6 ± 1.6) lux.. Whether the ambient illumination level is high or low, the contrast ration of SSTFEL devices with AR coatings is always higher than the contrast ration of SSTFEL devices without AR coatings. At the ambient illumination level of 200 Lux, the contrast ratio of SSTFEL devices with AR coatings is 5 times higher than that of SSTFEL devices without AR coatings. However the contrast ratio of SSTFEL devices with AR coatings is only 3 times higher than that of SSTFEL devices without AR

coatings at the ambient illumination level of 52.6 Lux, not 5 times as was expected.. The measurement error results from the measured reflection of ambient light being lower while sample S7 without AR coatings is off. During the sputtering process of ITO layers on the SSTFEL devices, the polypropylene sheets of devices were heated and became non-planar. The measurement results would be affected, although it was made as planar as possible during measurement. Therefore the contrast ratio of sample S7 was higher than its real value, had a perfectly planar sample been available.

Table 5.5 Contrast of SSTFEL devices with or without AR coating system under different luminance conditions

	Sample Number	Pixel state	L(average) (cd/m ²)	SSTFEL Device Contrast
Ambient illumination	200.0±7.1 Lux			
SSTFEL devices (with AR coating)	S41	Pixel on	79.3 ± 1.3	(15.4± 0.4):1
		Pixel off	5.13 ± 0.11	
SSTFEL devices (without AR coating)	S7	Pixel on	123.5 ± 1.5	(3.0± 0.1):1
		Pixel off	41.4 ± 1.5	
Ambient illumination	52.6±1.6 Lux			
SSTFEL devices (with AR coating)	S41	Pixel on	70.3 ± 0.8	(47.9± 1.0):1
		Pixel off	1.47 ± 0.03	
SSTFEL devices (without AR coating)	S7	Pixel on	87.0 ± 1.1	(15.8± 0.3):1
		Pixel off	5.51 ± 0.08	

Chapter 6 Setup of Model for AR coatings on Polypropylene Sheets, Simulation Results and Discussion

6.1 Model for the Reflectance Simulation of AR Coatings on Polypropylene Sheets

The structure of AR coatings on polypropylene sheets is shown in figure 6.1. The thickness of an ultra-thin gold layer on the top of ITO layer is around from 3 to 5 nm, and the thickness of an ITO layer is around 45nm. A thick gold layer with the thickness of around 36nm is sputtered by S150B Sputter Coater for 120 second on the polypropylene sheets.

When the sputtering time is limited to several seconds, the ultra-thin gold layers will be less than 5nm thick, too thin to be regarded as a solid optical film. According to the reflectance spectra of ultra-thin gold layers on Si substrates and glass substrates shown in the figures 4.16 and 4.17, it can be assumed that the surface of AR coatings

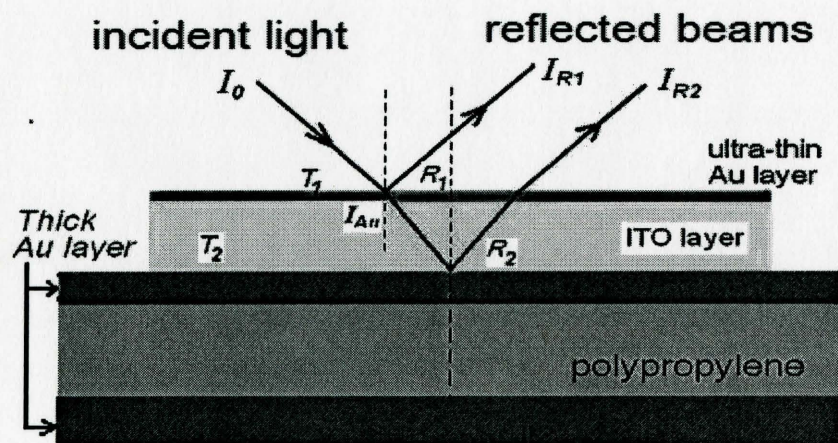


Figure 6.1 A schematic diagram of the model for AR coatings on polypropylene sheets

with the ultra-thin gold layer is regarded as a complex surface with the following properties:

1. Reflectance is equal to the sum of the reflectance of material below the ultra-thin gold layer and reflectance increment after the ultra-thin gold layer is sputtered on it. Thus its reflectance can be expressed in this work as

$$R_1 = R_{ITO} + \Delta R_{Au-on-ITO} \quad (6.1)$$

2. There is no phase change of the light wave in the internal reflection from this complex surface due to the ultra-thin gold layer composed of dense tiny islands with high resistance. Internal reflectance coefficient r_1 can be expressed as

$$r_1 = \sqrt{R_1} \quad (6.2)$$

where R_1 is the reflectance of this complex surface. For the external reflection, the reflectance coefficient is

$$r_1' = -r_1. \quad (6.3)$$

If the incident light is expressed as $E_0 e^{i\omega t}$, the intensity of incident light and a reflected beam are expressed as

$$I_0 = (E_0 e^{i\omega t}) \times (E_0 e^{i\omega t})^* = E_0^2 \quad (6.4)$$

$$\begin{aligned} I_{R1} &= (r_1 E_0 e^{i\omega t}) \times (r_1 E_0 e^{i\omega t})^* \\ &= r_1 r_1^* E_0^2 = R_1 I_0 \end{aligned} \quad (6.5)$$

where $(E_0 e^{i\omega t})^*$ and $(r_1 E_0 e^{i\omega t})^*$ are the conjugates of $(E_0 e^{i\omega t})$, $(r_1 E_0 e^{i\omega t})$ respectively.

3. The phase change of the light wave can be neglected due to the low thickness of the ultra-thin gold layer. The intensity of incident light passing the ultra-thin gold layer is

$$\begin{aligned} I_{Au} &= (t_1 E_0 e^{i\omega t}) \times (t_1 E_0 e^{i\omega t})^* \\ &= t_1 t_1^* E_0^2 = T_1 I_0 \end{aligned} \quad (6.6)$$

where t_1 is the transmittance coefficient of the ultra-thin gold layer, and $t_1 = t_1^*$. Thus t_1 can be expressed as

$$t_1 = \sqrt{T_1} \quad (6.7)$$

where T_1 is transmittance of the ultra-thin gold layer shown in the figure 6.1.

Reflectance coefficient of the ITO/Au interface is assumed and expressed as

$$r_2 = \sqrt{R_2} e^{-i\Delta} \quad (6.8)$$

where R_2 is reflectance of the ITO/Au interface shown in figure 6.1, and Δ is the phase change of the ITO/Au interface shown in figure 6.1. It cannot be assumed that Δ is still π even if the thick gold layer is a continuous film physically with thickness of 36nm. However optical properties of this thick gold layer are different from that of bulk gold for two reasons: Firstly, its reflectance spectrum is different from that of bulk gold as shown in figure 5.1, and it is not opaque in the visible wavelength range as is bulk gold. Secondly, the surface of this thick gold layer on polypropylene sheets does not look like a

smooth mirror due to the annealing processes. Therefore Δ will be treated as a parameter in the simulation.

When the light passes the ITO layer, its intensity decreases further and can be expressed as

$$\begin{aligned} I_{ITO} &= (t_2(t_1 E_0 e^{i(\omega t)})e^{-i\delta}) \times (t_2(t_1 E_0 e^{i(\omega t)})e^{-i\delta})^* \\ &= t_2 t_2^* t_1 t_1^* E_0^2 \\ I_{ITO} &= T_2 T_1 E_0^2 \end{aligned} \quad (6.9)$$

where δ is the phase change of the light wave resulting from passing through the ITO layer, and t_2 is the transmittance coefficient of the ITO layer and $t_2 = t_2^*$. Thus, t_2 can be expressed as

$$t_2 = \sqrt{T_2} \quad (6.10)$$

where T_2 is the transmittance of the ITO layer shown in the figure 6.1.

The transmittance spectra of gold layers in figure 4.18 shows that the transmittance of a thick gold layer is lower than 30 percent in most of the range of visible wavelengths when its sputtering time is 90 seconds. For a gold layer with a sputtering time of 120 seconds, its transmittance will be less than 30 percent in the visible wavelength range. Therefore, we can neglect approximately the effect of the reflected light from the interface behind this thick gold layer in simulation.

6.2 The Reflectance of the AR Coating on Polypropylene Sheets

Because it is difficult to measure indexes of two gold layers, the multiple-beam interference method is selected to calculate the reflectance of AR coatings on a thick gold

layer by considering the superposition of the reflected beams shown in the figure 6.2. The phase difference between successive beams due to passing an ITO layer at close to normal incident angle is given as

$$\delta = 2 * \frac{2\pi}{\lambda_0} * n_{ITO} d_{ITO} \tag{6.11}$$

here n_{ITO} and d_{ITO} are the refractive index and thickness of an ITO layer respectively. If the incident light is expressed as $E_0 e^{i\omega t}$, the successive reflected beams can be expressed by appropriately modifying both the amplitude and phase of the initial wave.

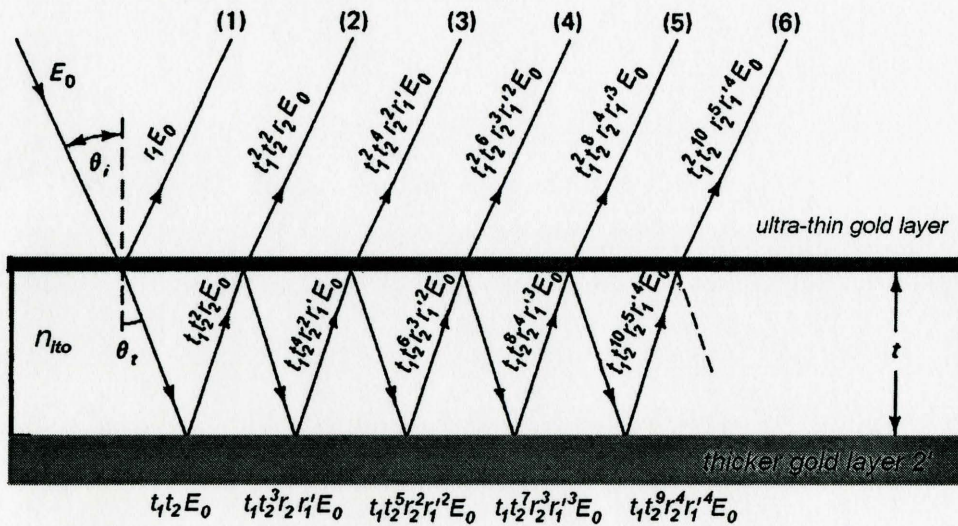


Figure 6.2 Schematic diagram of AR coating on thick gold layer with the thickness of 360nm.

Referring to figure 6.2, there are

$$E_1 = (r_1 E_0) e^{i\omega t}$$

$$E_2 = (t_1^2 t_2^2 r_2 E_0) e^{i(\omega t - \delta)}$$

$$E_3 = (t_1^2 t_2^4 r_2^2 r_1 E_0) e^{i(\omega t - 2\delta)}$$

$$E_4 = (t_1^2 t_2^6 r_2^3 r_1'^2 E_0) e^{i(\omega t - 3\delta)}$$

$$E_5 = (t_1^2 t_2^8 r_2^4 r_1'^3 E_0) e^{i(\omega t - 4\delta)}$$

$$E_6 = (t_1^2 t_2^{10} r_2^5 r_1'^4 E_0) e^{i(\omega t - 5\delta)}$$

and so on, where r_2 is the reflectance coefficient of the interface between the ITO layer and the thick gold layer. Nth such reflected wave can be written as

$$E_N = (t_1^2 t_2^{2(N-1)} r_2^{N-1} r_1'^{N-2} E_0) e^{i(\omega t - (N-1)\delta)} \quad (6.12)$$

a form that holds for all but E_1 . Therefore, the resulting E_R may be written as

$$E_R = \sum_{N=1}^{\infty} E_N \quad (6.13)$$

$$E_R = r_1 E_0 e^{i\omega t} + \sum_{N=2}^{\infty} (t_1^2 t_2^{2(N-1)} r_2^{N-1} r_1'^{N-2} E_0) e^{i(\omega t - (N-1)\delta)} \quad (6.14)$$

$$E_R = E_0 e^{i\omega t} \left[r_1 + t_1^2 t_2^2 r_2 e^{-i\delta} \times \sum_{N=2}^{\infty} (t_2^{2(N-2)} r_2^{N-2} r_1'^{N-2}) e^{-i(N-2)\delta} \right]$$

The summation is now in the form of a geometric series,

$$\sum_{N=2}^{\infty} x^{N-2} = 1 + x + x^2 + x^3 + \dots \quad ; \quad (6.15)$$

where

$$x = t_2^2 r_2 r_1' e^{-i\delta} \quad (6.16)$$

Since $|x| < 1$, the series converges to the sum $S = 1/(1-x)$. Thus

$$E_R = E_0 e^{i\omega t} \left[r_1 + \frac{t_1^2 t_2^2 r_2 e^{-i\delta}}{1 - t_2^2 r_2 r_1' e^{-i\delta}} \right] \quad (6.17)$$

The reflectance of AR coatings is

$$R = \frac{E_R E_R^*}{E_0^2} = \left| r_1 + \frac{t_1^2 t_2^2 r_2 e^{-i\delta}}{1 - t_2^2 r_2 r_1' e^{-i\delta}} \right|^2 \quad (6.18)$$

After replacing r_1 , r_1' and r_2 by formulas (6.2), (6.3) and (6.10), and replacing t_1 and t_2 by (6.7) and (6.9) respectively, (6.18) is simplified to,

$$R = R_1 + \frac{T_1^2 T_2 R_2 + 2T_1 T_2^2 R_1 R_2 + 2T_1 T_2 \sqrt{R_1 R_2} \cos(\delta + \Delta)}{1 + T_2^2 R_1 R_2 + 2T_2 \sqrt{R_1 R_2} \cos(\delta + \Delta)} \quad (6.19)$$

where T_1 and T_2 are the transmittance of the ultra-thin gold layer and the ITO layer respectively. R_1 is the reflectance defined in expression (6.1). R_2 is the reflectance of the thick gold layer on the polypropylene sheet.

6.3 Extracting Transmittance Spectra of The Ultra-Thin Gold Layer and The ITO Layer from Experimental Results

Transmittance spectra of ITO films and ultra-thin gold films were measured by Cary 50 Probe UV Visible Spectrophotometer after they were deposited on glass substrate, which are shown in figures 4.10 and 4.18. During measurement, the same glass substrate was measured as a reference sample. The measurement transmittance of the ITO film on the glass is given by

$$T_{ITO_measured} = \frac{I_s}{I_{ref}} \quad (6.20)$$

where I_{ref} and I_s are the intensity of incident light after passing a reference sample and samples with an ITO film respectively. Both of them are shown in figure 6.3(a) and (b).

In the figure 6.3, I_0 is the intensity of incident light. The reflection of light from the two sides of the glass can be assumed to be the same and labeled R_g in figure 6.3(a).

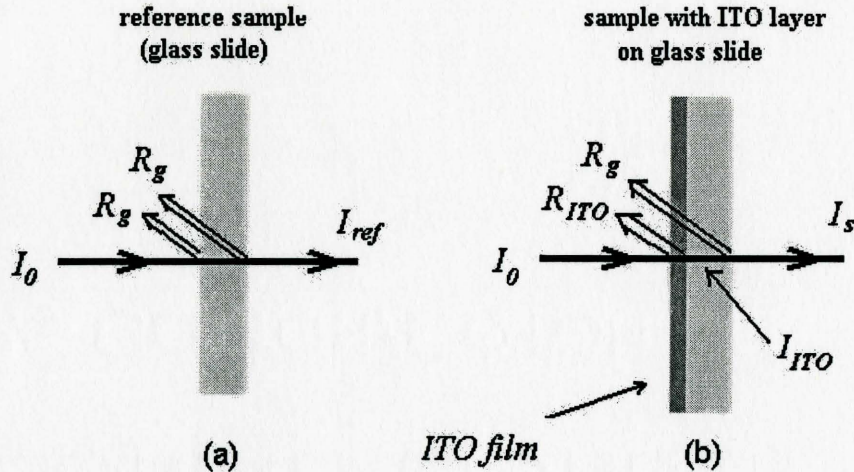


Figure 6.3 The schematic diagrams of the transmittance measurement of ITO films deposited on glass slides by Cary 50 Probe UV Visible Spectrophotometer

Considering reflections of surfaces and interfaces in measurement, expression (6.20) can be expressed approximately as

$$T_{ITO_measured} \approx \frac{I_0(1 - R_{ITO} - R_g)}{I_0(1 - 2R_g)} \quad (6.21)$$

where R_{ITO} simply expresses the reflectance of the ITO layer on the glass. It includes two parts; one is the reflection from the ITO surface, the other is the reflection from the interface between the ITO layer and the glass.

Because $R_g=0.04$, $1/(1 - R_g) \approx 1 + R_g$. Expression (6.21) can be approximately simplified as

$$\begin{aligned} T_{ITO_measured} &\approx (1 - R_{ITO} - R_g) \times (1 + 2R_g) \\ &\approx 1 - R_{ITO} + R_g \end{aligned} \quad (6.22)$$

On the other hand, the transmittance of the ITO film can be expressed as

$$T_2 \approx \frac{I_0(1 - R_{ITO})}{I_0} = 1 - R_{ITO} \quad (6.23)$$

Thus
$$T_2 = T_{ITO_measured} - R_g \quad (6.24)$$

Therefore the transmittance of the ITO film is equal to the difference between direct measured transmittance of the ITO layer on the glass and the reflectance of the glass surface.

Similarly the transmittance of ITO films, the transmittance of the ultra-thin gold film shown in figure 6.4 can be expressed as

$$T_1 = T_{Au_measured} - R_g \quad (6.25)$$

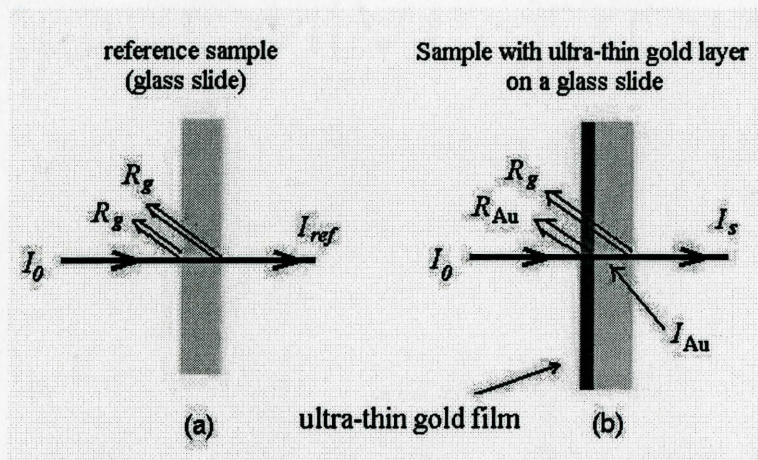


Figure 6.4 The schematic diagrams of the transmittance measurement of ultra-thin gold films on glass slides by Cary 50 Probe UV Visible Spectrophotometer

6.4 Extracting Reflectance Spectra of The Complex Surface and Interface Between ITO Layer and Thick Gold Layer from Experimental Results

Due to ITO films with the thickness like that of glass slides unavailable, it is difficult to directly measure the reflectance of ultra-thin gold layers on the ITO film

without the interference effect. And it is impossible to directly measure the reflectance of the interface between ITO layer and thick gold layer shown in figure 6.5(b).

Based on the experimental results shown in figures 4.16 and 4.17, the reflectance spectrum of the ultra-thin gold film whether on the Si substrate or on the glass substrate is similar to the reflectance spectrum of the substrate, and following the reflectance spectrum of the substrate but increasing by several percent. It is reasonable to assume approximately that the reflectance spectrum of the ultra-thin gold film on the ITO film, the complex surface in the model, is also equal to the sum of the ITO reflectance spectrum and several percent increment. It is expressed as

$$R_1 = R_{ITO} + \Delta R_{Au-on-ITO} \quad (6.26)$$

where R_{ITO} is the reflectance of the ITO film and $\Delta R_{Au-on-ITO}$ is the reflectance increment after the ultra-thin gold layer is sputtered on the ITO film. For simplifying the reflectance simulation of AR coatings, $\Delta R_{Au-on-ITO}$ is replaced by $\Delta R_{Au-on-Glass}$ approximately for the index of glass slide substrate being closer to the index of ITO layer. Thus R_1 in expression (6.26) is expressed as

$$R_1 \approx R_{ITO} + \Delta R_{Au-on-glass} \quad (6.27)$$

For simplification in the reflectance simulation of AR coatings, it is assumed approximately that the index of the ITO film deposited under sputtering conditions in this work is constant in the visible wavelength range. R_{ITO} in the normal incident situation is

$$R_{ITO} = \left(\frac{n_{air} - n_{ITO}}{n_{air} + n_{ITO}} \right)^2 \quad (6.28)$$

where n_{air} is the index of air and n_{ITO} is the index of the ITO layer with 1.97 in this work.

So R_I can be expressed as

$$R_1 = \Delta R_{Au-on-glass} + \left(\frac{n_{air} - n_{ITO}}{n_{air} + n_{ITO}} \right)^2 \quad (6.29)$$

$\Delta R_{Au-on-Glass}$ can be obtained from experimental data shown in figure 4.17

The reflectance of ITO/Au interface, $R_{ITO/Au}$, is replaced by the reflectance of the Air/Au interface, $R_{air/Au}$, shown in figures 6.5(a) and (b). Thus the reflectance coefficient of the ITO/Au interface in expression (6.8) can be expressed as

$$r_2 = \sqrt{R_2} e^{-i\Delta} = \sqrt{R_{air/Au}} e^{-i\Delta} \quad (6.30)$$

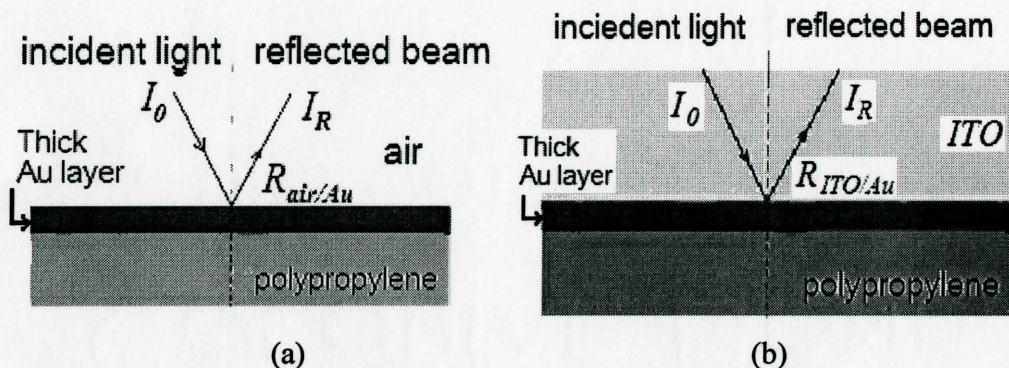


Figure 6.5 The schematic diagrams of interface reflections between the air and a thick gold layer (a); and between the ITO layer and the thick gold layer (b).

where Δ is the phase change of ITO/Au interface shown in figure 6.5(b). $R_{air/Au}$ is the reflectance of air/Au interface shown in figure 6.5(a) and its measurement result is shown in figure 5.1.

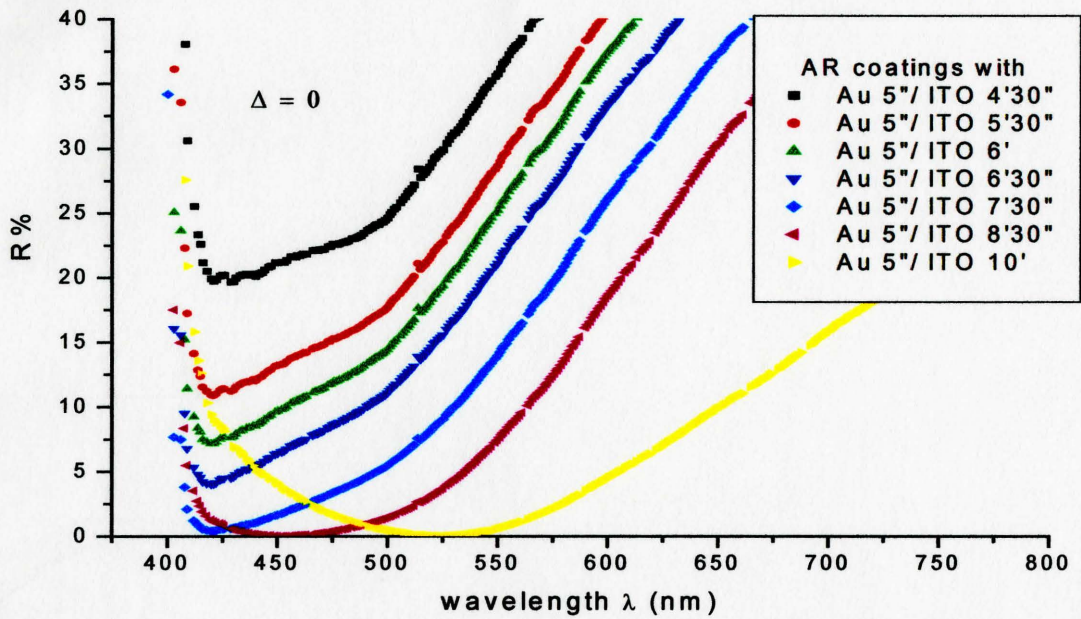
6.5 Calculating reflectance of AR coatings on Polypropylene Sheets

Based on assuming the phase change of the reflected light on the surface of AR coatings be zero in the model, the smaller the thickness of the ultra-thin gold layer, the

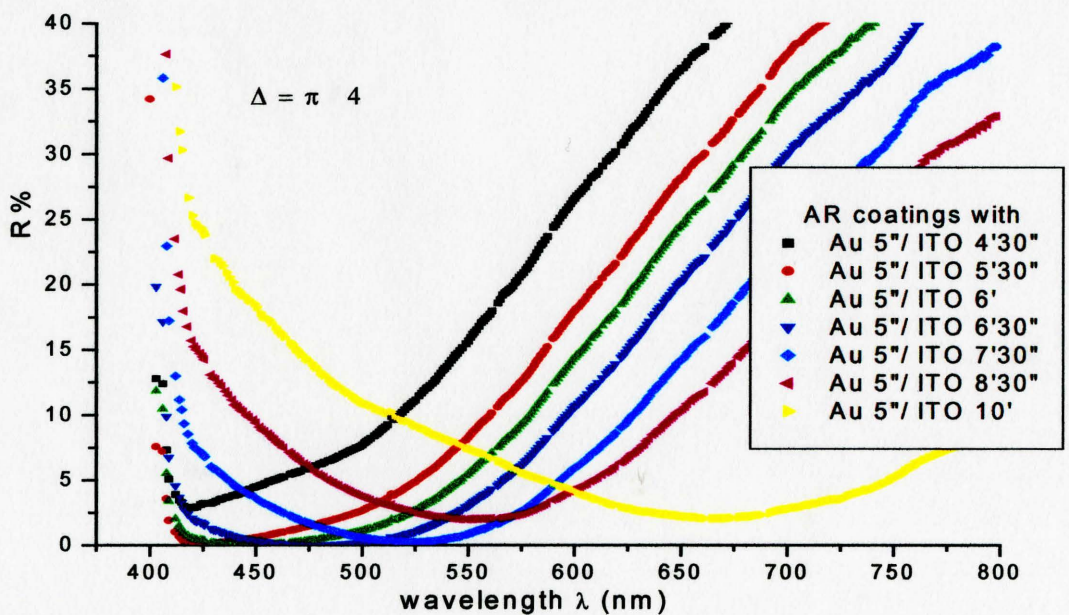
better the approximation of this model to calculate the reflectance of AR coatings. The reflectance simulation was applied on the AR coatings composed of different ITO layers and ultra-thin gold layers with sputtering times of 5 seconds and 12 seconds. Simulation results of AR coating reflectance are shown in figures 6.6 and 6.7 from page 103 to 110. Because the transmittance of ITO layers with sputtering times of 5', 6' and 6'30" have only been measured, the transmittance of ITO layers with sputtering times of 4'30" and 5'30" were approximately replaced by the experimental data of the ITO layer with sputtering time of 5'. The transmittance of ITO layers with sputtering times of 7'30", 8'30" and 10' were approximately replaced by the experimental data of the ITO layer with sputtering time of 6'30" in the calculation.

To compare each group of reflectance spectra in figure 6.6 with one group in figure 6.6(h), which is the experimental results of AR coatings composed of ultra-thin gold layers with sputtering times of 4 seconds and the same thickness of different ITO layers, it can be seen clearly that spectral curves in figure 6.6(e) have similar relative position and variation in visible wavelengths to those of spectral curves in figure 6.6(h). Similarly in figure 6.7, the spectral curves in figure 6.7(d) have similar relative position and variation in visible wavelengths to those of spectral curves in figure 6.7(h). The simulation results show that the phase change of Δ is around $\pi/2.5$. Although, the simulation reflectance of AR coatings does not match exactly with the measurement value of the reflectance of AR coatings due to the approximate calculation in the simulation and the effect of diffused reflection from the thick gold layer, the match of the spectral variation trends at two end ranges of visible wavelengths and their similarity in

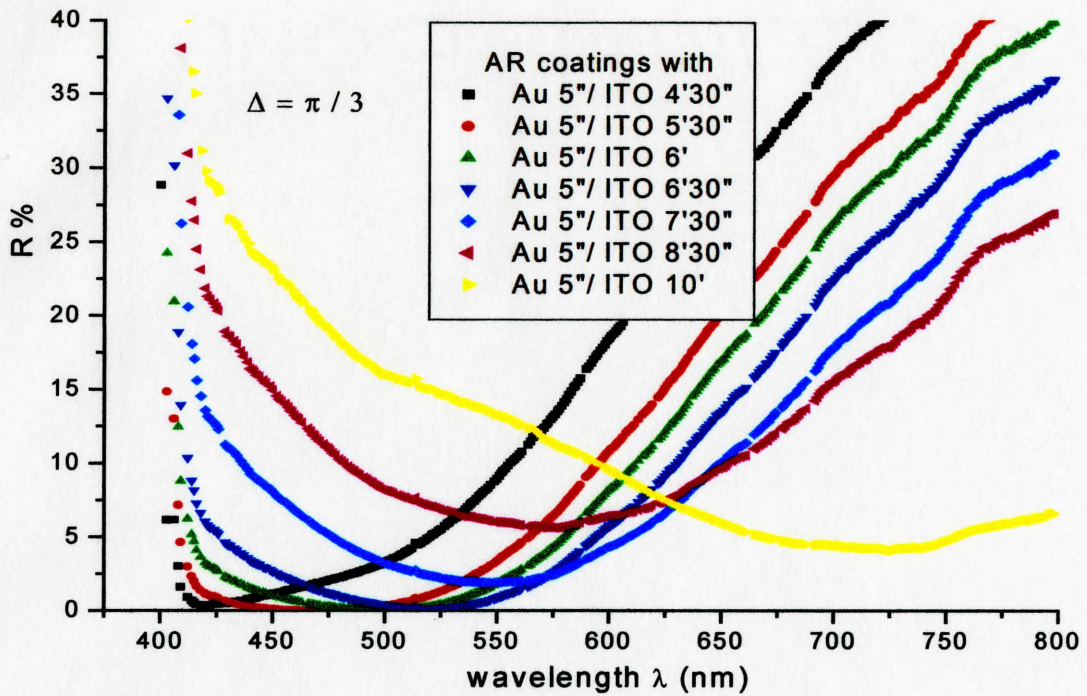
detail at the mid range of visible wavelengths show that the model and assumptions for simulating reflectance of AR coatings on polypropylene sheets can predict the basic features of experimental curves.



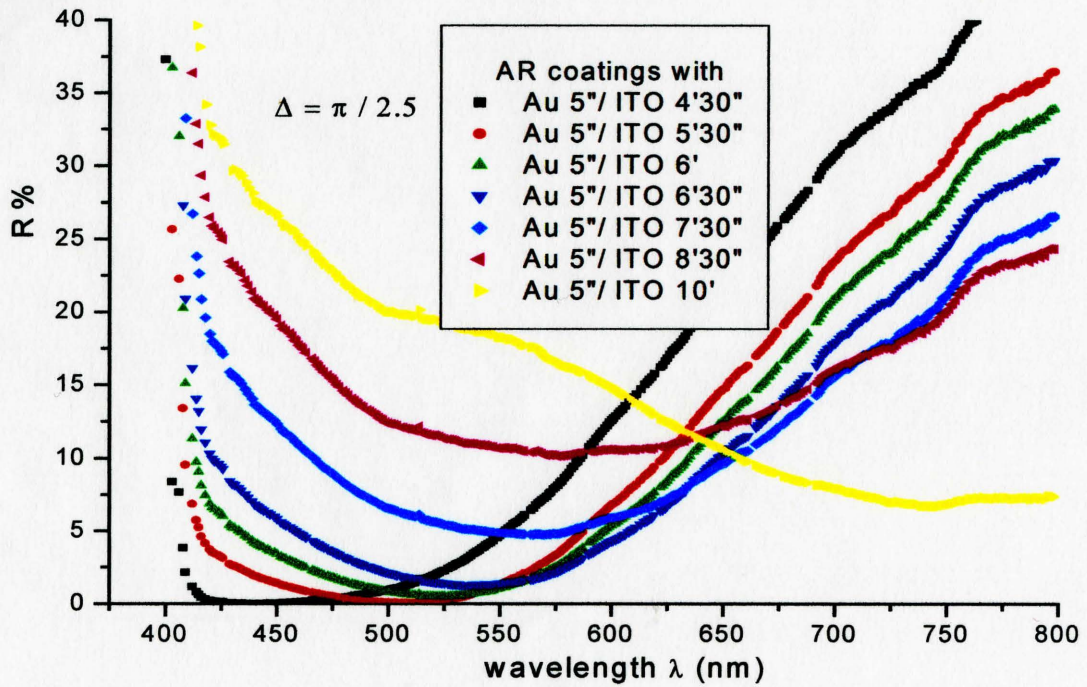
(a)



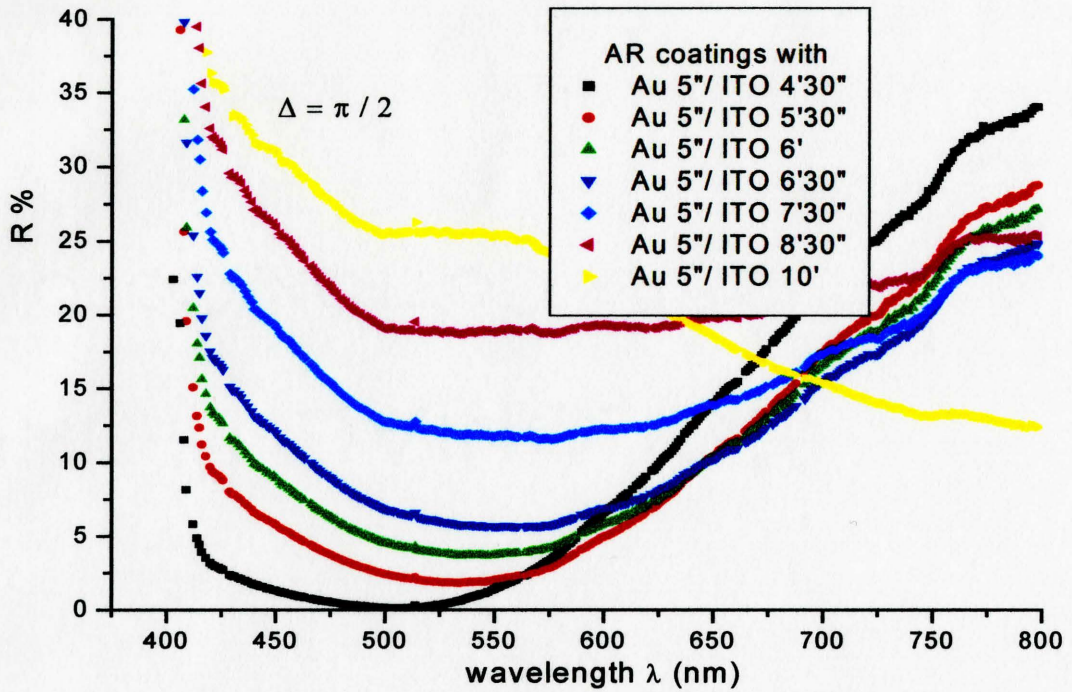
(b)



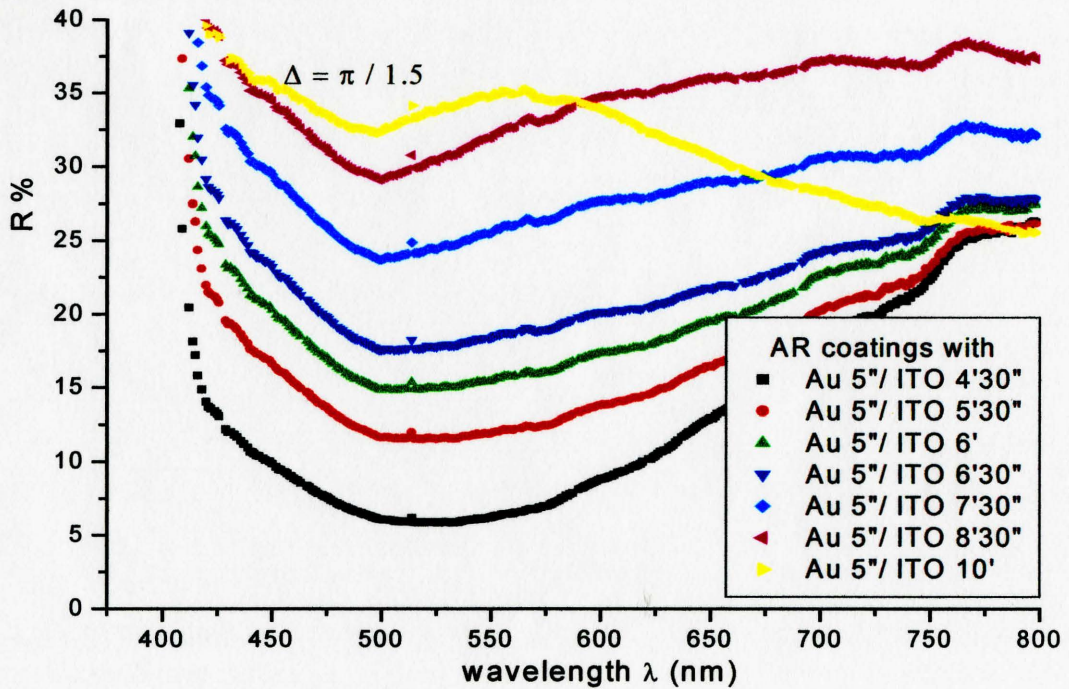
(c)



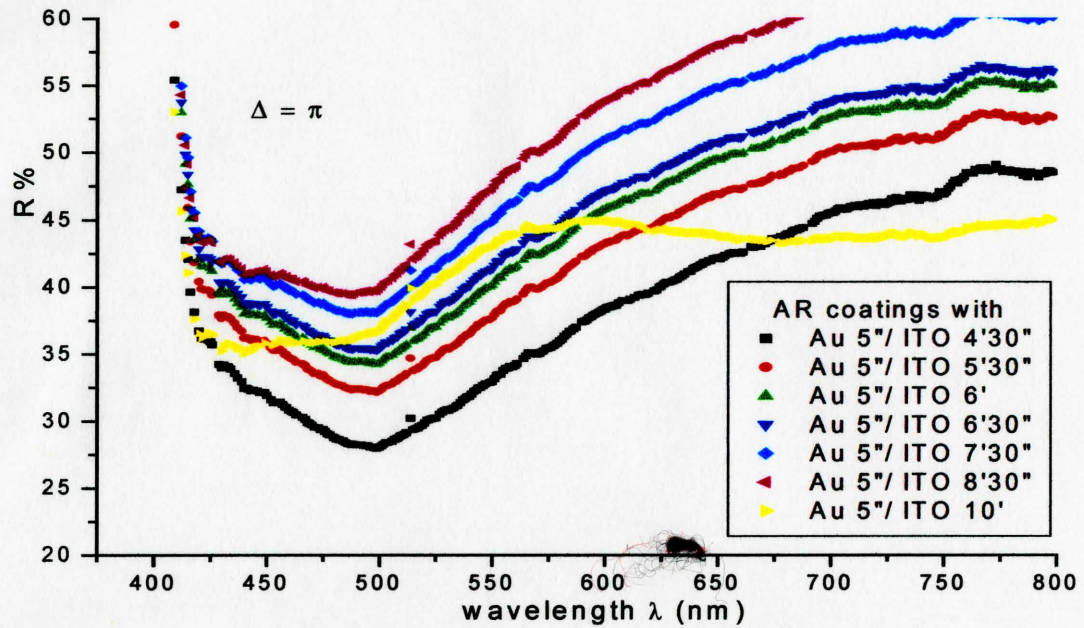
(d)



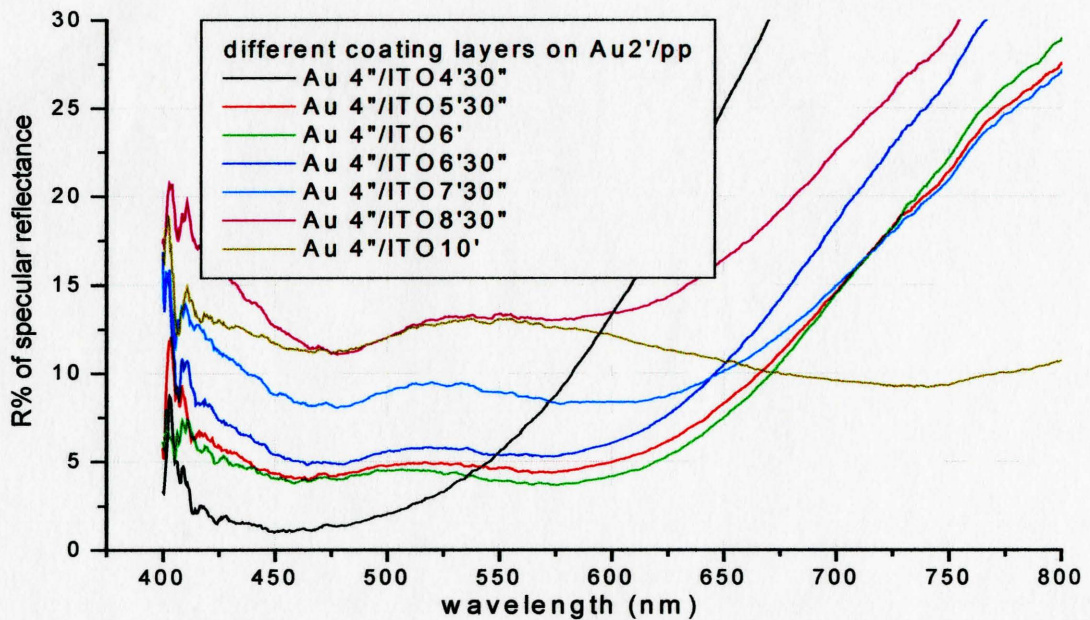
(e)



(f)

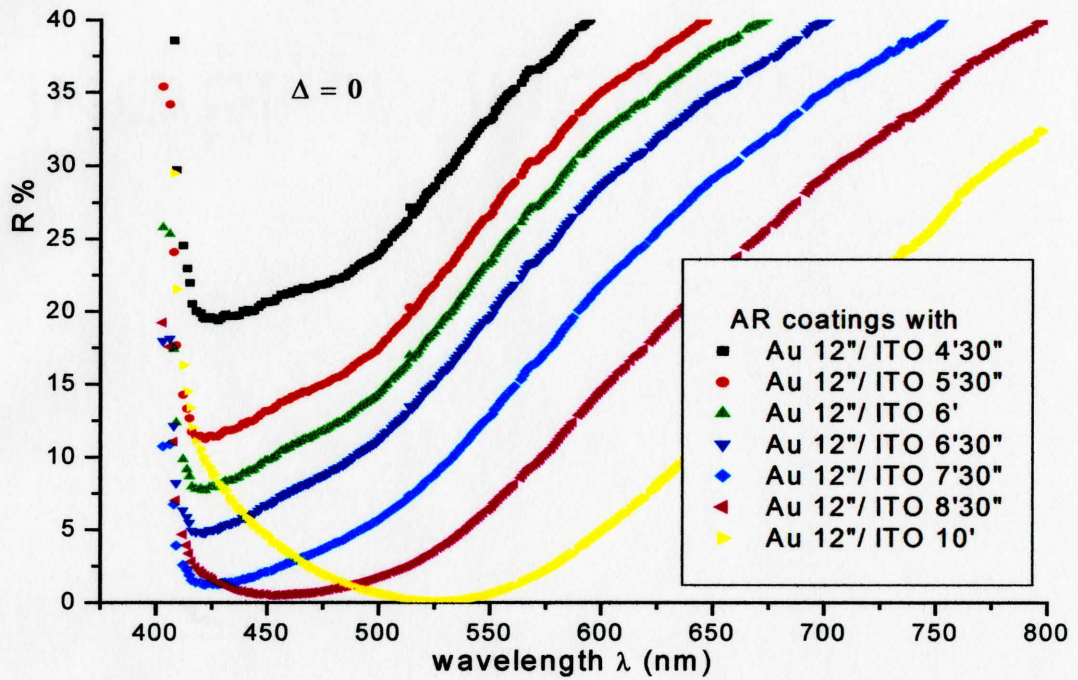


(g)

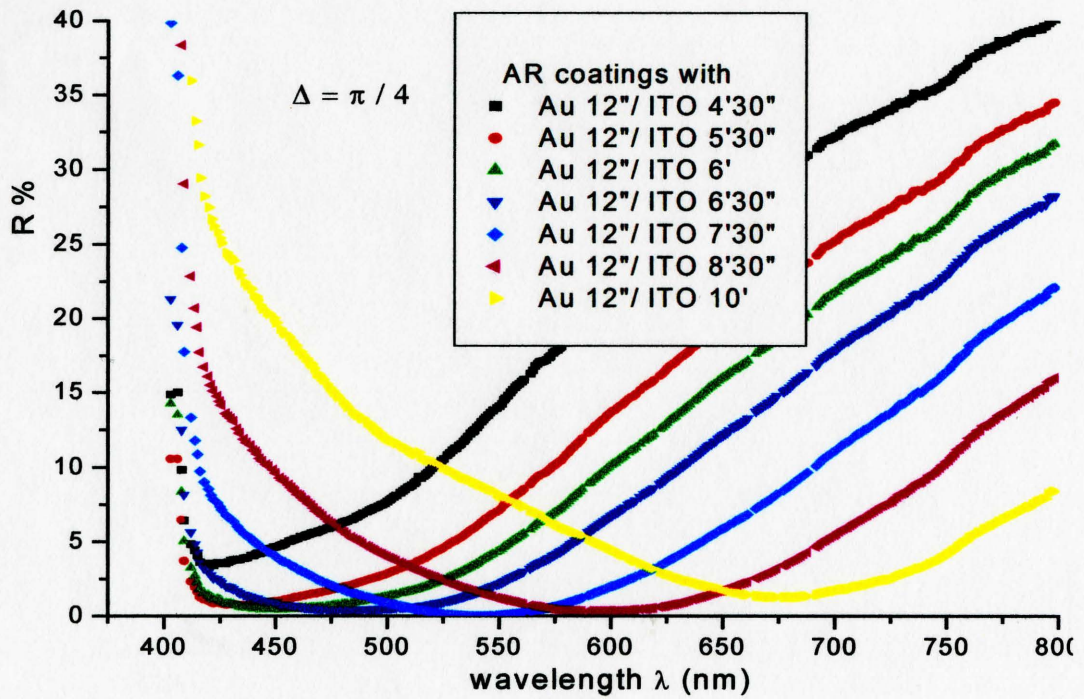


(h)

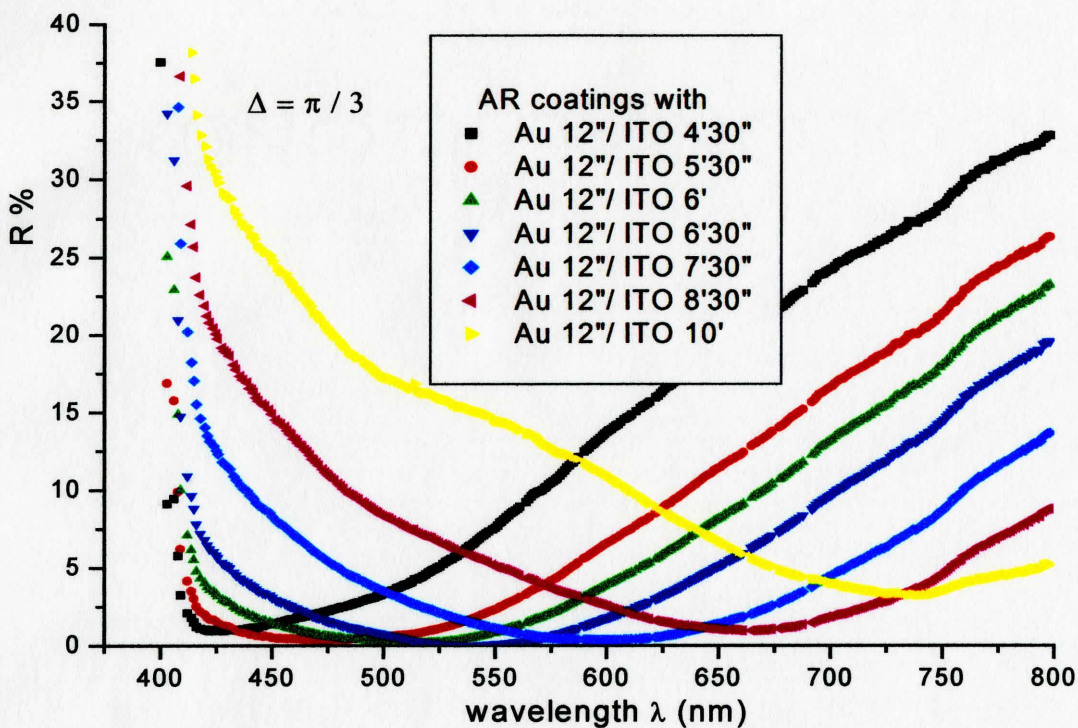
Figure 6.6 The simulation results of specular reflectance of AR coatings composed of ultra-thin gold layer with sputtering time of 5 seconds and different ITO layers are shown from (a) to (g) as the parameter of Δ is changed from 0 to π . (h) is the measurement results of AR coatings composed of ultra-thin gold layer with sputtering time of 4 seconds and different ITO layers



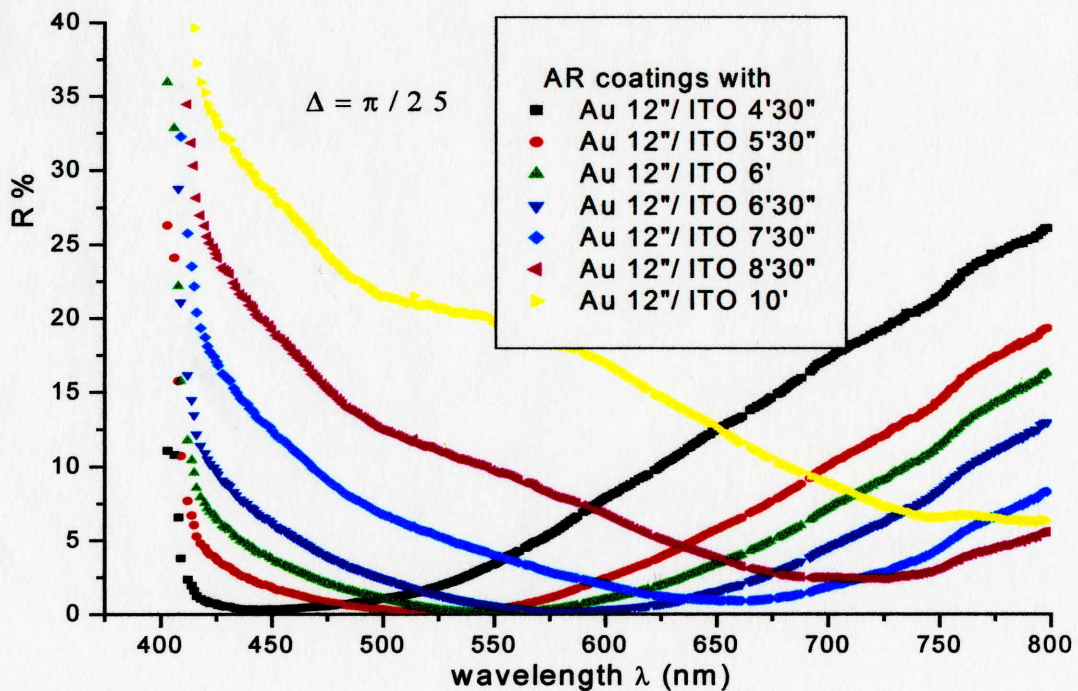
(a)



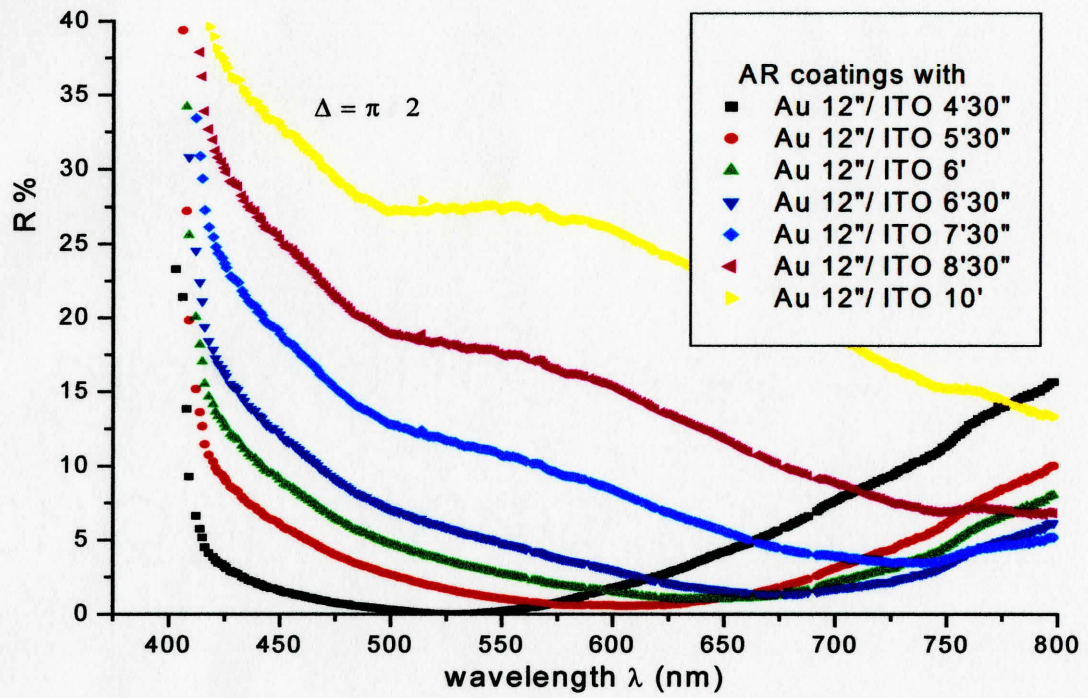
(b)



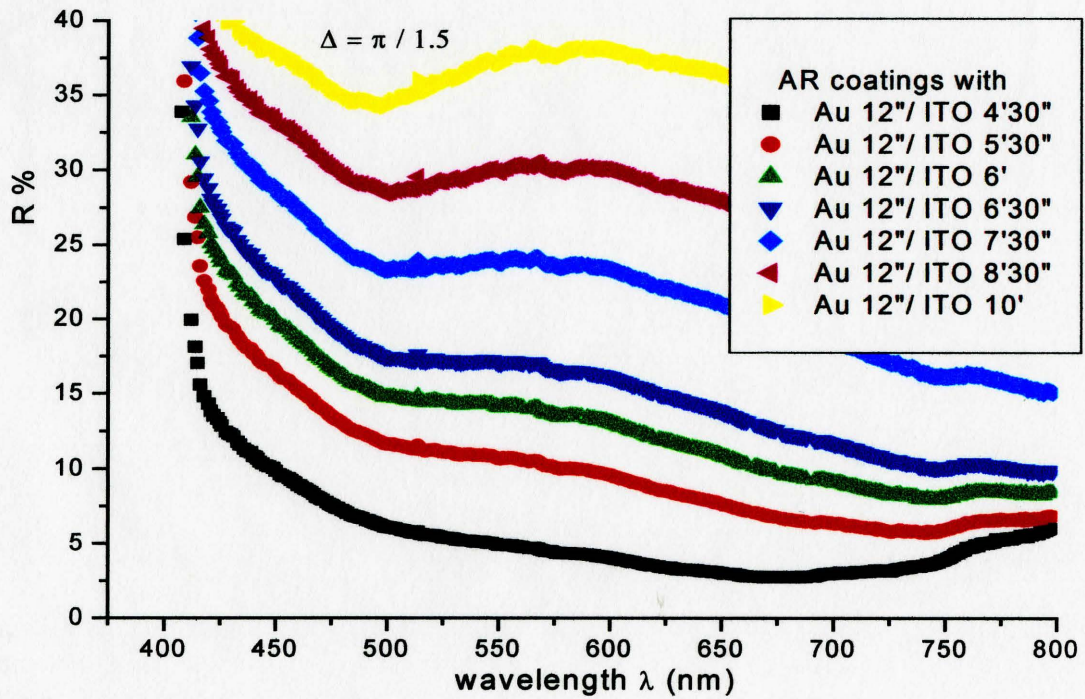
(c)



(d)



(e)



(f)

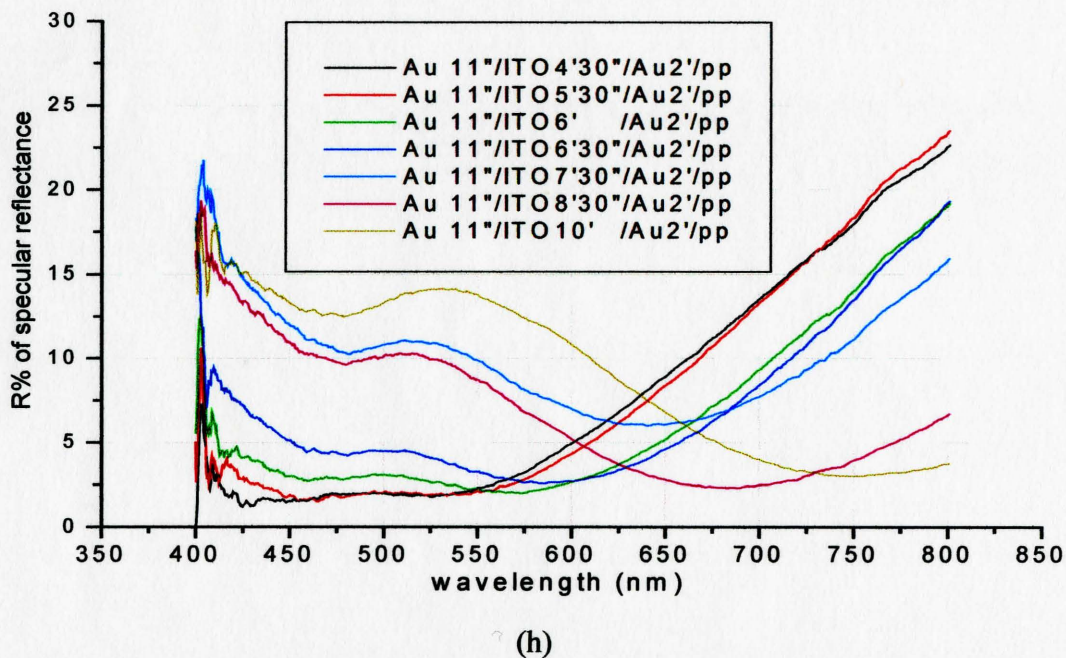
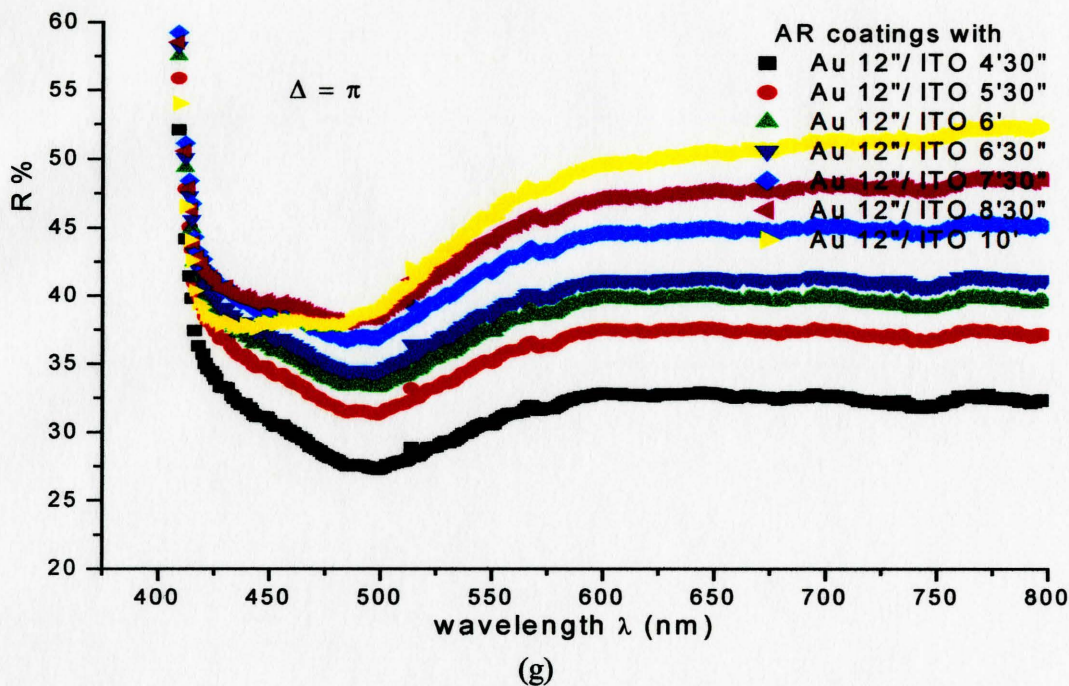


Figure 6.7 The simulation results of specular reflectance of AR coatings composed of ultra-thin gold layer with sputtering time of 12 seconds and different ITO layers are shown from (a) to (g) as the parameter of Δ is changed from 0 to π . (h) is the measurement results of AR coatings composed of ultra-thin gold layer with sputtering time of 11 seconds and different ITO layers

Chapter 7 Conclusion and Future Work

7.1 Conclusion

This thesis has not only developed an antireflection coating for the SSTFEL device, but also optimized its to increase contrast ratio of the device high up to 49:1 at ambient illumination level of 52.6 Lux, which is at least 3 times higher than that of SSTFEL devices without AR coatings.

The AR coating is composed of an ultra-thin gold layer and an ITO layer. During research, the index, transmittance spectrum and sheet resistance of ITO films related to sputtering conditions have been studied. At the deposition conditions of RF power of 30W, chamber pressure of 0.5mTorr and Ar flow ratio of 7.0sccm, ITO films have high transmittance over 75% in visible wavelength and good conductivity with sheet resistance of 131.2 ± 6.1 (ohms per square). The refractive index is 1.97. It was found that the polypropylene sheets were crinkled and wrinkled during the deposition process of ITO layers at the RF power of 45W.

The ultra-thin gold layer plays is an adjusting layer of reflecting intensity in AR coatings. Its transmittance and reflectance spectra are important in the AR coatings and have been measured. Results from the measurement of its reflectance spectra show that its reflectance spectrum is totally different from bulk gold when its thickness is less than 10 nm. It then appears the reflectance spectrum of substrates moving up several percent. However, as its thickness increases over to 30nm, its reflectance spectrum is some similar to that of bulk gold.

AFM technology was also utilized to image the surface morphology of ultra-thin gold layers and measure the thickness of ultra-thin gold layers. AFM images suggest that the surface morphology of ultra-thin gold films are similar whether on Si substrates, on polypropylene sheets or on the surface of ITO films. Therefore the measured sputtering speed of the ultra-thin gold film on the Si substrate by AFM technology can be used to evaluate the thickness of the ultra-thin gold layer sputtered on polypropylene sheets under the same sputtering conditions.

In order to maximize the destructive interference of ambient light in visible wavelengths, a number of samples were made by depositing AR coatings on polypropylene sheets and SSTFEL devices, which were composed of different thicknesses of ITO layers and ultra-thin gold layers. Specular and diffuse reflection spectra of samples have been measured and compared. Areas under spectral curves of reflection with good performance AR coatings were integrated over visible wavelengths from 410 or 425 to 700nm. Considering the high transmittance of AR coatings needed, results show that AR coatings have best performance in reducing the surface reflection of samples as the thickness of ultra-thin gold layers ranges from 3.4 to 4.0nm and thickness of ITO layers ranges from 424 to 450Å.

Sheet resistance of two groups of ultra-thin gold layers sputtered on the top of ITO layers show that the conductivity of the ultra-thin gold layer become better as thickness of the ultra-thin gold film decreases to a certain value. However it is supposed to be worse according the theory of tunneling effects that has been reported. This

phenomenon is difficult explain by the interface effects between tiny gold islands and the ITO layer, or by systematic errors of measurement. It is worth exploring further.

7.2 Recommendations for Future Work

At first, although results of two groups of samples of ultra-thin gold films show the anomalous behavior in the relationship between sheet resistance and thickness, extensive research on it in detail is attractive to gain a physical understanding of the nano-structure material.

Based on the optical and electric properties of ultra-thin gold films and a growth model at room temperature, it is very interesting to extend the research for its applications in optical filters, AR coatings in visible wavelength range and infrared wavelength range.

As shown in the AFM images of ultra-thin gold films with thickness of around 3nm, it can be assumed that this gold nano-film is composed of gold quantum dots (QDs) with high density on the surface of Si substrates, polypropylene sheets and ITO films for its sputtered process kept at room temperature. This growth model might hint that it is worth trying to grow the III-V semiconductor QDs at lower temperature than usual growth temperature for high density QDs.

Because of bad adhesive ability of polymer with metals, it was found that the backside electrode of SSTFEL devices, which was a gold layer deposited on a polypropylene sheet, did not adhere on the backside of the polypropylene sheet well. A new structure has been proposed to improve the adhesive property between the electrode

and the polypropylene sheet. It is a sandwich structure of ITO layers and gold layers. Based on the initial experimental result, an improvement of the adhesive between the electrode and the polypropylene sheet was observed. It would be interesting to extend research and development on this structure.

Appendix A:

Experimental Setup of Reflectivity Measurement System and Reflection Spectra Measurement

Reflection spectrum measurement is one of the most common optical measurement techniques. In general, there are two kinds of reflection from the surface: one is specular reflection; the other is diffuse reflection.

The measurement of specular reflectance spectra of samples were all performed in a dark room, but diffuse reflectance spectra were measured under ambient illumination of light bumps with thermal radiations. Both of them were measured by USB 2000 Fiber Optic Spectrometer of Ocean Optics Inc.

A.1. Experimental Setup and Measurement for the Specular Reflection

Figure A.1 shows a schematic diagram of the experimental setup of specular reflectivity measurement system. Light off the source of a tungsten halogen lamp was directed onto the surface of samples at incident angle less than 7° by an optical fiber with $200\mu\text{m}$ core diameter. The light source was cooled by a fan in order to maintain the output power and spectrum stable during measurement. Samples were mounted on an optical stage that could be adjusted in three directions. An optical fiber with $400\mu\text{m}$ core diameter, which is a component of USB 2000 Fiber Optic Spectrometer, was mounted with angle of near 7° over the surface of samples as a guidance fiber for reflected light. The reflected light was directed by this guidance fiber into USB 2000 Fiber Optic

Spectrometer and recorded in intensity spectrum by OOIBase 32 Spectrometer Operating Software installed in a computer

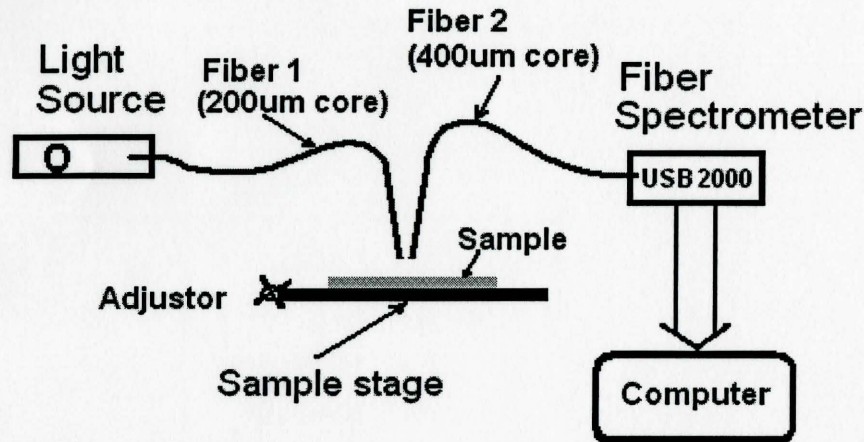


Figure A.1 A schematic diagram of the measurement set up of the specular reflection.

Before measuring samples, reference samples, a 500nm Al film deposited on a Si and a glass substrate, were put on the stage and the intensity spectra of reflection light were measured. Fibers and the sample on the stage were adjusted to make the detected signal maximum. The sample was put on the same position of the stage and measured at the same experimental conditions.

The specular reflection spectrum of the sample is

$$R_{sample}(\lambda) = \frac{I_{sample}(\lambda) - I_{Dark}(\lambda)}{I_{Al}(\lambda) - I_{Dark}(\lambda)} * R_{Al}(\lambda)$$

where $I_{sample}(\lambda)$ and $I_{Al}(\lambda)$ are the intensity spectra of specular reflection from the surface of samples and the Al reference sample respectively. $I_{Dark}(\lambda)$ is noise spectrum of USB 2000 Fiber Optic Spectrometer measurement system. R_{Al} is the reflectance spectrum of the Al film [A.1].

A.2 Experimental Setup and Measurement for the Diffuse Reflection

The diffuse reflection from the surface of samples was measured also by USB 2000 Fiber Optic Spectrometer. The measurement environment is totally different from that for the measurement of specular reflection. Instead of fluorescent lamps in the lab, six tungsten filament incandescent lamps with powers of 60 to 100W were used to make average and isotropic illumination on the surface of samples due to their continuous spectrum. The guidance fiber was mounted over the surface of samples with a 90° angle as shown in figure A2. The diffuse reflection light out off the surface of samples was directed into the USB 2000 Fiber Optic Spectrometer and their spectral data were recorded by OOIBase 32 Spectrometer Operating Software in the computer.

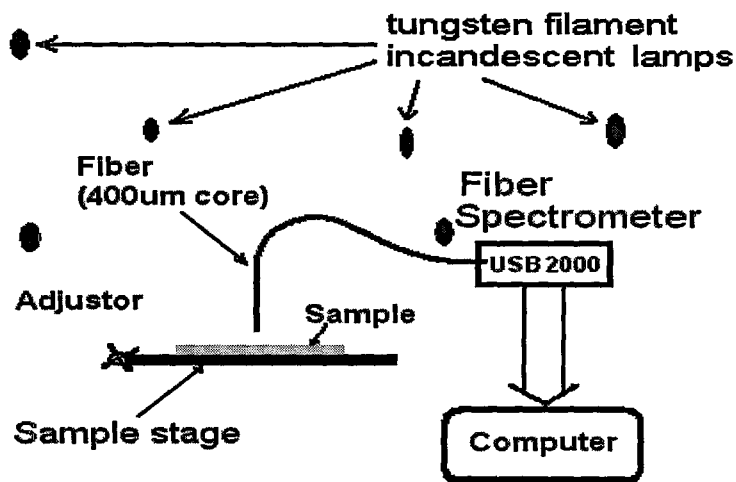


Figure A.2 A schematic diagram of the measurement set up of the diffuse reflection

Under the illumination of 311 Lux measured with Luminance Meter LS-100 of Minolta Camera Co, Ltd., a reference sample with diffuse reflectance of near 90% in the visible wavelength range was measured at first. Reference samples are the KODAK Gray

Cards with calibrated neutral diffuse reflectance spectra. Then, the sample was measured as was done in the measurement of specular reflection.

The diffuse reflection spectrum of the sample is

$$R_{sample}(\lambda) = \frac{I_{sample}(\lambda) - I_{Dark}(\lambda)}{I_{reference}(\lambda) - I_{Dark}(\lambda)} * R_{reference}(\lambda)$$

where $I_{sample}(\lambda)$ and $I_{reference}(\lambda)$ are the intensity spectra of diffuse reflection light from the surface of samples and the reference sample respectively. $I_{Dark}(\lambda)$ is noise spectrum of USB 2000 Fiber Optic Spectrometer measurement system. $R_{reference}$ is the diffuse reflectance spectrum of the reference sample shown in figure A3, which is a copy from a part of the product manual of KODAK Gray Card.

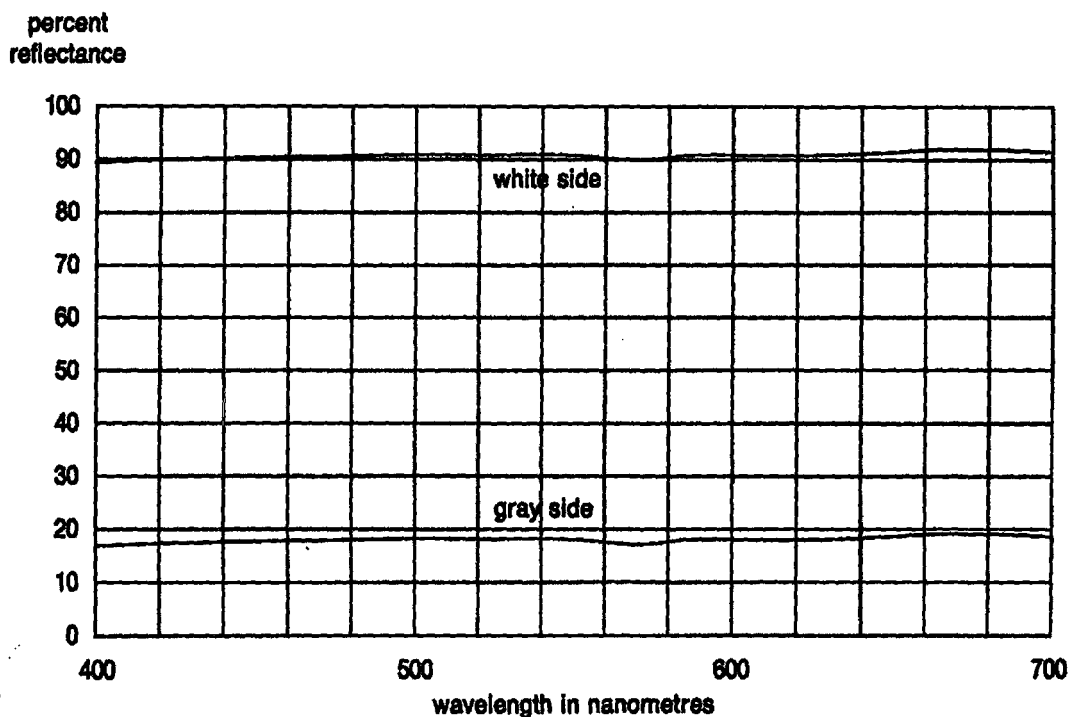


Figure A.3 This graph shows the percent reflectance of the KODAK Grad Card in relation to light wavelength in manometers. A white side curve is the reflectance spectrum of the reference sample.

Appendix B.

Ellipsometry Measurement System

Ellipsometry is an old but highly sensitive optical method, which enables us to measure the refractive index and thickness of semi-transparent thin films by relying on the fact that the polarization of incident light changes upon an interface or sequence of interfaces between media of different refractive index. Incident linearly polarized light with both s and p components will be elliptically polarized after reflection. Null ellipsometry is a classical ellipsometric technique based on the measurement of azimuth angle of a polarizer, a compensator, and an analyzer for which the detected intensity of light is extinguished. A typical null ellipsometer is shown in figure B.1.

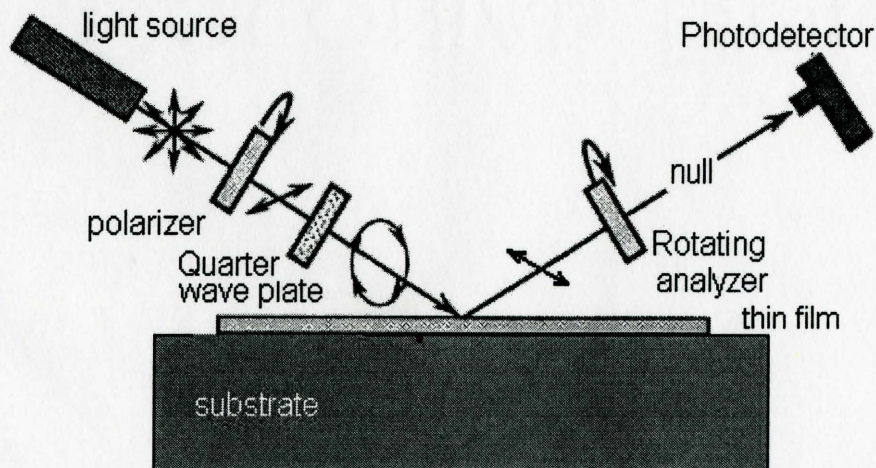


Figure.B.1 Schematic diagram of a null ellipsometry measurement system.

The incident light passes first through a rotating polarizer, and then through a quarter-waver plate with its axes fixed at 45 degrees to the incident plane. The incident

light becomes elliptically polarized. By rotating the polarizer to the special orientation to make the incident light to be an appropriate elliptical polarization, the ellipticity of the light is removed by the reflection. The reflected light becomes linearly polarized. The null condition at the photodetector is satisfied when the analyzer is crossed with it.

The fundamental equation of ellipsometry is

$$\frac{r_{PP}}{r_{SS}} = \tan \psi e^{i\Delta} \quad (3.1)$$

The quantities ψ and Δ are called the ellipsometric parameters, which are measured by the ellipsometer. ψ is the angle whose tangent is the ratio of the magnitudes of total reflection coefficient, while Δ denotes the relative phase difference between the p-wave and s-wave before the reflection as δ_1 and the phase difference after the reflection as δ_2 . If performed carefully and with four-zone averaging, the null ellipsometer can give very accurate experimental data with few or no systematic errors.

In the ellipsometric equation, r_{SS} and r_{PP} are *s* and *p* total reflection coefficients of the thin film on the substrate.

$$r_{PP} = \frac{r_{01,TE} + r_{12,TE} e^{-i\delta}}{1 + r_{01,TE} r_{12,TE} e^{-i\delta}} \quad (3.2)$$

$$r_{SS} = \frac{r_{01,TM} + r_{12,TM} e^{-i\delta}}{1 + r_{01,TM} r_{12,TM} e^{-i\delta}} \quad (3.3)$$

Where $\delta = \frac{4\pi n_1 d_1 \cos \phi_1}{\lambda}$, and $r_{ij,TE(TM)}$ ($i=0,1; j=1,2$) are Fresnel reflection coefficients of

TE and *TM* mode on the interfaces between material *i* and material *j* as shown from expression (4.23) to (4.26).

Therefore, from measurement results of ellipsometric parameters Ψ and Δ , the index and thickness of a film can be obtained by solving the ellipsometric equation.

In this work, index and thickness of ITO layers deposited on the Si substrate were measured by a Philips PZ2000 Laser Ellipsometer working at the wavelength of 632.8nm.

Reference:

Chapter 1

- [1.1] Funada, F, M Hijikigawa “Recent Trend of Display Devices”, <http://sharp-world.com/corporate/rd/tj1/pdf/2.pdf>
- [1.2] Suh, Dong-Hae, Young-IL, Gon Son, and et. al, SID Digest, **34** (2003) 601
- [1.3] Oka, Yoshihiro, Atsushi Ban, Masaya Okamoto, SID Digest, **33** (2002) 1204
- [1.4] Kim, W. H. and Kafafi Z. H., SID Digest, **33** (2002) 1090
- [1.5] Ayako, Yoshida, Sou Fujimura and *et. al.*, SID Digest, **34** (2003) 856
- [1.6] Yingwei, Xiang, A. H. Kitai and *et. al.* SID Digest, **35** (2004) 82
- [1.7] A. H. Kitai, Yingwei Xiang and Brian Cox, Journal of the SID **13/6** (2005) 493
- [1.8] Li Li, “Optical Coatings for Displays” in Optical interference coatings, Springer series in optical sciences; V. 88, edit by Norbert Kaiser, Hans K. Pulker, Berlin; New York: Springer, (2003) 433
- [1.9] http://www.luxellresearch.com/black_layer_video.htm
- [1.10] <http://www.xerotechnology.com/ip1.nsf>

Chapter 2

- [2.1] Guden, H., R. W. Pohl, Z. F. Physick **2** (1929) 192
- [2.2] Tang, C. W. and S. A. VanSlyke, Appl. Pyhs Lett., **51** (1987) 913
- [2.3] Russ, M. J. and D. I. Kennedy, J. Electrochem. Soc., **114** (1967) 1066
- [2.4] Ono, A. Yoshimasa., “Electroluminescent Displays”, edited by Hiap L. Ong, World Scientific Publishing Company, New Jersey, (1995) 9
- [2.5] Rack, D. Philip, and Paul H. Holloway, Materials Science and Engineering, **R21**, (1998) 177

- [2.6] Flynn, John Michael, “Investigation of the Influence of Cadmium Processing on $Zn_{1-x}Ga_xO_4$:Mn Thin Films for Photoluminescent and Thin Film Electroluminescent Applications”, Ph.D thesis, McMaster University, (2003) 53
- [2.7] Frank, L. Pedrotti, S.J, Leno S. Pedrotti, “Introduction to Optics”, 2th, Prentice-Hall, Inc., New Jersey, 1993
- [2.8] Macleod, H. A., “Thin-Film Optical filters”, edit by W. T. Welford, Adam Hilger Ltd., Bristol, England, 1986
- [2.9] Fowles, Grant R, “Introduction to modern optics”, edit by Grant R Fowles, Holt, Rinehart and Winston, New York, 1975
- [2.10] Zheng, Yanfei, Kazuo Kikuchi, Masafumi Yamasaki, Kenichirou Sonoi, and Kazuhiro Uehara, Applied Optics, 36 (1997) 6335
- [2.11] X. W. Wu, N. Dalacu, and A. H. Kitai, J. Electrochem. Soc., 137 (1990) 2987

Chapter 3

- [3.1] Moulson, A. J., and J. M. Herbert, “Electroceramics: Materials; Properties, Application, Thomson Press Ltd. Great Britain, (1990) 3
- [3.2] T. Minami, T. Miyata, S. Takata, I. Fukada, Jap. J. Appl. Phys., 36 (1990) L117
- [3.3] A. H. Kitai, Z. Jing, J. Deng, and K. Cook, SID Digest, 30 (1999) 596.
- [3.4] Y-H, Lee, K-S. Shin, Y-S. Kim and et. al., SID Digest, 30 (1999) 600
- [3.5] Cairns, R. Darran, Richard P. Witte II, and et. al., Appl. Phys. Lett., 76 (2000) 1425
- [3.6] Crawford, P. Gregory, SID Digest, 36 (2005) 10
- [3.7] M. H. Frey, and D. A. Payne, Phys Rev. B, 54 (1996) 3158
- [3.8] Wada, Satoshi, Takeyuki Suzuki and Tatsuo Noma, Jpn. J. Appl. Phys., 34 (1995) 5368
- [3.9] Wada, Satoshi, Hiroaki Yasuno, Takuya Hoshina and et. al., Jpn. J. Appl. Phys., 42 (2003) 6188
- [3.10] Xiang, Yingwei, “Sphere-Supported Thin Film Electroluminescence Technology”, Ph. D Thesis, (2006)

Chapter 4

- [4.1] V. A. Tolmachev, Onokhov, A. P, J. of Optical Technology, **65** (1998) 117
- [4.2] R. A. Synomicki, Thin Solid Films, **313-314** (1998) 394
- [4.3] Chiou, Bi-shiou, and Jen-Huan Tsai, J. of Materials Science: Materials in Electronic **10** (1999) 491
- [4.4] Bright, C., Proceedings, Annual Technical Conference - Society of Vacuum Coaters, (1993) 63
- [4.5] Song, Seok-Kyun, Seok-Keun Koh, Deuk Yeon Lee and Hong –Koo Baik, Jap J. of Applied Physics **43** (2004) L15
- [4.6] Jiang, Yong, Guan Bo, and Xu Xiao Liang, Chin. Phys. Lett., **22** (2005) 730
- [4.7] Galdikas, A., S Kačiulis, A. Mironas, and A Šetkus, Sensors and Actuators **B43** (1997) 186
- [4.8] Smith, G. B., G. A. Niklasson, J. S. E. M. Svensson, and C.G. Granqvist, J. Appl. Phys., **59** (1986) 571
- [4.9] Sennett, R. S., and G. D. Scott, J. of the Optical Society of America, **40** (1950) 203
- [4.10] Silva A. Da., C. Andraud, J. Lafait and A. Dakka, J. Phys.: Condens. Matter, **12** (2000) 4125
- [4.11] Kaiser, Norbert, Applied Optics, **41** (2002) 3053
- [4.12] Liang, Pan, “GS-MBE Growth of In(Ga)As Self-Organized Quantum Dots”, McMaster University, (2002) 38
- [4.13] Grimvall, G., and T. G. Andersson, J. Phys. D: Appl. Phys., **16** (1983) 1985
- [4.14] Neugerauer C. A., and M. B. Webb, J. of Applied Physics, **33** (1962) 74
- [4.15] Inoue, Yoku, Makoto Inata, Minoru Fujii, Shinji Hayashi, Keiichi Yamamoto, Thin Solid Film, **349** (1991) 289

[5.1] David W. Lynch, and W. R. Hunter, “Handbook of Optical Constants of Solids”, edited by Edward D. Palik, Academic Press, Inc. LTD, London, (1985) 294